

## Pulsar timing arrays: the emerging gravitational-wave landscape

C. M. F. MINGARELLI<sup>(1)</sup> <sup>(2)</sup>(<sup>\*</sup>), J. A. CASEY-CLYDE<sup>(3)</sup><sup>(1)</sup>, Y. T. CHANG<sup>(4)</sup>, E. EISENBERG<sup>(4)</sup>,  
 F. HUTCHISON<sup>(1)</sup> N. KHUSID<sup>(5)</sup>, B. LARSEN<sup>(1)</sup>, A. MORAN<sup>(6)</sup>, F. SEMENZATO<sup>(7)</sup>,  
 L. WILLSON<sup>(3)</sup> and Q. ZHENG<sup>(1)</sup>

<sup>(1)</sup> *Department of Physics, Yale University - New Haven, CT, USA*

<sup>(2)</sup> *Center for Computational Astrophysics, Flatiron Institute, 162 5th Avenue, New York, NY, 10010, USA*

<sup>(3)</sup> *Department of Physics, University of Connecticut - Storrs, CT, USA*

<sup>(4)</sup> *Department of Astronomy, Yale University - New Haven, CT, USA*

<sup>(5)</sup> *Department of Physics and Astronomy, Stony Brook University - Stony Brook, NY, USA*

<sup>(6)</sup> *Department of Astronomy, Columbia University - New York, NY, USA*

<sup>(7)</sup> *Dipartimento di Fisica e Astronomia “G. Galilei”, Università degli Studi di Padova - Padova, Italy*

**Summary.** — Pulsar Timing Array (PTA) experiments have entered a new era with evidence for a nanoHertz gravitational wave background (GWB). This review describes the physics of detection, detailing the noise models and cross-correlation techniques required to isolate the Hellings-Downs curve. We discuss astrophysical implications, arguing that the perceived tension between current amplitudes and standard merger models is largely resolved by new insights into supermassive black hole binary populations. Beyond the stochastic background, we review the framework for multi-messenger continuous gravitational-wave searches, highlighting targeted search campaigns and rigorous detection protocols. We also examine the potential to probe New Physics, including cosmic strings and ultralight dark matter. Critical challenges are addressed, including small-scale leakage bias in anisotropy searches and the separation of deterministic signals from the GWB and pulsar noise. Finally, we outline the field’s future, from rapid data combination strategies to the sensitivity gains expected from the Square Kilometre Array Observatory (SKAO) and DSA-2000.

PACS 04.30.-w – Gravitational waves.

PACS 04.80.Nn – Gravitational wave detectors and experiments.

PACS 97.60.Gb – Pulsars.

---

5	1. Introduction
7	State of the Art

---

(<sup>\*</sup>) E-mail: chiara.mingarelli@yale.edu

9	2.	The Gravitational Wave Background
10	2'1.	Why the nanoHertz GWB is stochastic
12	2'2.	PTA Response to GWs
13	2'3.	The General Plane Wave Framework
15	2'4.	Derivation of the Hellings and Downs Curve
19	2'5.	The Characteristic Strain Spectrum
19	2'6.	A discrete population of SMBHBs
20	3.	GWB Predictions and Limits
20		The Foundational Era (1995–2013)
21		The “Stalling” Crisis (2014–2018)
21		The Noise Modeling Breakthrough (2020–2021)
22		The Modern Era (2021–Present)
23		The Astrophysical GWB Ceiling
24	4.	Modeling the GWB
27	4'1.	Major Merger Models
28	4'2.	Quasar-based SMBHB Models
30	4'3.	Astrophysics-agnostic Models
31	5.	Gravitational Wave Background Anisotropy
31	5'1.	Search Methods for Anisotropy
32	5'1.1.	Spherical Harmonics
32	5'1.2.	Square-Root Spherical Harmonics
33	5'1.3.	Pixel-based Methods
33	5'1.4.	The Radiometer
34	5'1.5.	Fisher Matrix Formalism
34	5'1.6.	Timing-Residual Maps and BiPOSH
35	5'2.	Scaling Laws and the Shot Noise Regime
36	5'2.1.	Anisotropy from a Single Bright Source
37	5'3.	GWB Polarization from Anisotropies
37	5'4.	Cross-Correlation Analysis
38	5'5.	Challenges in Detecting Anisotropy
41	5'6.	Recent Results and Future Prospects
42	6.	Continuous Gravitational Waves
43	6'1.	Electromagnetic Counterparts
43	6'2.	Signal Model
43	6'2.1.	The Polarization Angle as a Basis Rotation
44	6'3.	All-Sky Searches
45	6'4.	Targeted Searches
46	6'5.	The first steps of a protocol for CW detection
47	6'6.	Comparison: Targeted vs. All-Sky
47	6'7.	Deterministic Fingerprints of CWs
50	6'8.	Strong Lensing
52	6'9.	Joint Likelihood Multi-Messenger Analysis
52	6'10.	Cosmology with Bright Sirens
53	6'11.	Binary Evolution: The PTA Time Machine
54	6'12.	Pulsar Distances
54	7.	The Angular Resolution of PTAs
54	7'1.	The Incoherent Regime
55	7'2.	The Coherent Regime
56	7'3.	Implications for Searches
56	8.	Search for New Physics
56		Cosmic Strings
57		Cosmological Phase Transitions
57		Primordial Gravitational Waves and Inflation
57		Ultralight Dark Matter
58		Tests of General Relativity and Alternative Polarizations

58	9. Pulsar Noise Models
64	10. The International Pulsar Timing Array
65	10.1. The Need for Data Combination: Scaling Laws
68	10.2. The LITE method: three steps to combination
69	10.3. FrankenStat: likelihood-level data combination without merging TOAs
69	10.4. Fourier-space combination and global Gibbs sampling
69	10.5. Outlook
69	11. Complementary Science
69	11.1. Picohertz GW Searches
71	11.2. Mapping Galactic Acceleration
74	12. Conclusion and Future Outlook
77	Acknowledgements
78	references

---

## Executive Summary

Six pulsar timing arrays (PTAs)—the North American Nanohertz Observatory for Gravitational Waves (NANOGrav), the European PTA, the Indian PTA, the Parkes PTA, the Chinese PTA, and the MeerKAT PTA—have reported evidence for a nanoHertz-frequency gravitational wave (GW) background (GWB), opening the lowest-frequency window of GW astronomy. This review surveys this emerging nanoHertz GW landscape.

**The GWB (§2–§4).** We derive the PTA response from first principles, including the Hellings–Downs correlation that distinguishes a GWB from correlated noise. The characteristic strain  $h_c(f)$  directly probes the supermassive black hole binary merger rate and chirp mass distribution, with chirp mass as the dominant factor governing the amplitude. At low frequencies the GWB is a superposition of  $\sim 10^6$  sources; at mid-frequencies this thins to  $\sim 10^3$ ; at the highest frequencies there may not be a single binary per frequency bin. The measured amplitude is in  $2\text{--}4\sigma$  tension with most predictions, though more massive black holes than previously assumed help ease this tension.

**GWB anisotropy (§5).** An astrophysical GWB is anisotropic. Hence, detecting anisotropy, or establishing its absence, directly tests the GWB’s origin. At low frequencies anisotropies trace the large-scale structure of the Universe and can be recovered through cross-correlations with galaxy catalogs. At high frequencies, a few loud binaries dominate each frequency bin. This is the regime where anisotropy is most detectable. We review search methods from spherical harmonics to pixel-based approaches.

**Individual binaries (§6).** We review three complementary approaches to searching for continuous GW from individual binary systems: all-sky searches, targeted searches using electromagnetic priors, and joint-likelihood multi-messenger analyses. The first systematic targeted search of 114 active galactic nucleus candidates has established a protocol requiring signal coherence, robustness against a correlated GWB model, dropout analyses, and more. Strong gravitational lensing and bright-siren cosmography are explored as future science goals. The angular resolution of PTAs (§7) sets the fundamental localization limits for these searches.

**New physics (§8).** The GWB spectrum may encode signals from cosmic strings, phase transitions, primordial GWs, and ultralight dark matter through spectral and polarization signatures distinct from the supermassive black hole binary signal. Searches for non-Einsteinian polarization modes—scalar or vector contributions producing monopolar or dipolar correlations—offer a direct test of general relativity in the nanoHertz band.

**Custom noise models (§9).** Accurate per-pulsar noise characterization underpins all PTA results. Custom noise models now treat achromatic red noise, chromatic interstellar medium variations, and instrumental systematics within hierarchical Bayesian frameworks. Getting the noise right determines the inferred GWB amplitude, the significance of continuous wave candidates, and the reliability of anisotropy searches.

**The International PTA (§10).** The IPTA combines data from all regional collaborations into a single global array. We review its data releases, mock data challenges, and complementary science, and discuss the long timescales inherent in full data combination. Rapid synthesis frameworks, such as the Lite method and FrankenStat, now enable global constraints on timescales of months rather than years.

The SKAO and the Deep Synoptic Array will push PTAs into the coherent regime with more pulsar discoveries, sub-arcminute source localization, while decades-long baselines will open the picohertz band. Evidence for the GWB is just the beginning—PTAs are poised to become a cornerstone of multi-messenger GW astronomy.

## 1. – Introduction

*Historical Context.* – Pulsar Timing Arrays (PTAs) have a rich history at the interface of physics and astronomy. The idea of using precise radio links to detect gravitational waves (GWs) dates to the mid-1970s, when Estabrook and Wahlquist [1] proposed that Doppler tracking of interplanetary spacecraft could reveal the signature of passing GWs. Motivated by high-precision tracking data from the Pioneer 10 mission, they calculated the effect of plane GWs on the two-way Doppler shift of a signal sent by a distant spacecraft, and suggested that cross-correlating the Doppler residuals from several spacecraft could isolate a GW signal from plasma and clock noise. In practice, however, the frequency stability of the best available clocks—hydrogen masers—was insufficient to detect the expected GW amplitudes. Moreover, the technique probed a frequency band of  $\sim 10^{-4}$ – $10^{-1}$  Hz where loud astrophysical sources were not anticipated at the time. Meanwhile, the discovery of the binary pulsar PSR B1913+16 by Hulse and Taylor [2], and the subsequent measurement of its orbital decay in precise agreement with General Relativity [3], provided the first indirect evidence for GW emission and galvanized the broader effort to detect GWs directly.

The breakthrough came with the realization that nature provides far better clocks than any spacecraft oscillator. Sazhin [4] and Detweiler [5] independently proposed that the regular radio pulses from pulsars could serve the same role, but with dramatically improved precision and at much lower frequencies ( $\sim$  nHz) set by the multi-year observing baselines. Building on this idea, Hellings and Downs [6]—working at NASA’s Jet Propulsion Laboratory (JPL), where spacecraft Doppler tracking was pioneered—submitted a landmark paper on October 1, 1982, using pulsar timing residuals from four ordinary (slow) pulsars to place an upper limit on the isotropic gravitational-wave background (GWB). More importantly, they showed that a true GWB would imprint a characteristic quadrupolar-like pattern of correlations between pulsar pairs as a function of their angular separation on the sky. This is now known as the Hellings-Downs curve, and its detection remains the “smoking gun” that distinguishes a GWB signal from correlated noise. The paper was accepted just nineteen days later, on October 20, 1982.

Unbeknownst to Hellings and Downs, a discovery was already underway that would transform the significance of their work. On September 25, 1982—six days before the Hellings-Downs paper was even submitted—Backer et al. [7] had detected a fleeting signal at the Arecibo Observatory: two harmonics of a 1.558 ms periodicity from the steep-spectrum radio source 4C21.53. The signal appeared for only three minutes and could not be reproduced the following day. It was not until November 7, weeks after the Hellings-Downs paper was already accepted, that the source was confirmed as PSR 1937+21, the first millisecond pulsar. Millisecond pulsars—recycled pulsars spun up to periods of  $\sim 1$ – $10$  ms through accretion from a binary companion, with timing stabilities rivaling atomic clocks—would prove to be the ideal clocks that the Hellings and Downs cross-correlations method needed. Together, these two developments gave rise to the concrete possibility of a PTA: a Galaxy-scale GW detector built from an array of precisely timed millisecond pulsars.

Fig. 1 summarizes the key milestones from these early theoretical foundations through to the current era. Foster & Backer [8] took the critical next step by constructing the first PTA: a dedicated program at the NRAO 43 m telescope timing PSRs 1620–26, 1821–24, and 1937+21 over a two-year baseline beginning in 1987. Their 1990 paper formalized the use of a spatial array of millisecond pulsars to simultaneously provide a long-timescale time standard, detect perturbations of the Earth’s orbit, and search for a GWB. The

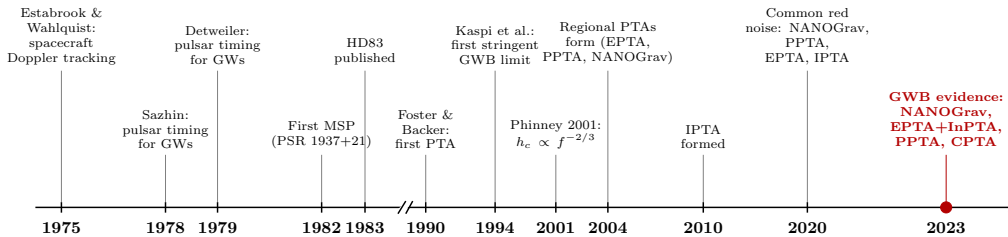


Fig. 1. – **Timeline of key milestones in PTAs.** From the first proposals for GW detection via spacecraft Doppler tracking (1975) and pulsar timing (1978–79), through the near-simultaneous development of the Hellings–Downs correlation framework (1983) and the discovery of the first millisecond pulsar (1982), to the construction of the first PTA by Foster & Backer (1990) [8], the first stringent GWB upper limit by Kaspi et al. (1994) [9], Phinney’s GWB strain spectrum (2001) [11], the formation of PTA collaborations, the independent detections of a common red-noise process (2020–2022) [17–20], and the landmark 2023 evidence for a GWB.

observing equipment of the era limited their timing residuals to  $\sim 1 \mu\text{s}$ , so while they demonstrated the method and placed an early GWB constraint, the first truly stringent limit came from Kaspi, Taylor & Ryba [9], who used over eight years of high-precision Arecibo data on PSRs B1855+09 and B1937+21 (with residuals of  $\sim 0.2\text{--}0.8 \mu\text{s}$ ) to set an upper limit of  $\Omega_g h^2 < 6 \times 10^{-8}$ . McHugh et al. [10] subsequently reanalyzed the same data within a Bayesian framework, demonstrating the practical power of millisecond pulsar timing for GW searches. A key theoretical advance came with Phinney [11], who derived a simple relation between the GWB spectrum, the time-integrated energy spectrum of individual sources, and the comoving number density of their remnants. This result established the canonical  $h_c \propto f^{-2/3}$  power-law prediction for a population of circular, GW-driven SMBHBs, providing the standard spectral benchmark against which all subsequent PTA measurements have been compared.

Through the late 1990s and 2000s, three regional PTA collaborations took shape. In Australia, a long-running pulsar timing program at the Parkes 64 m telescope was formalized as the Parkes PTA (PPTA) [12], which pioneered many of the noise modeling and data analysis techniques now standard across the field, including the TEMPO2 timing package [13]. In Europe, observations from five major radio telescopes were combined under the European PTA (EPTA) [14]. In North America, the North American Nanohertz Observatory for Gravitational Waves (NANOGrav) [15] unified US and Canadian efforts around the Arecibo Observatory and the Green Bank Telescope. These three programs motivated the formation of the International PTA (IPTA) in 2010 [16], which combines data across all regional arrays (see sect. 10 for a full discussion). The Indian PTA (InPTA) and the African Pulsar Timing array (APT<sup>(1)</sup>) subsequently joined as full members. More recently, the Chinese PTA (CPTA) and the MeerKAT PTA (MPTA) have begun contributing independent datasets, though they are not yet formal IPTA members.

The search for nanoHertz-frequency GWs has now reached a historic milestone. After decades of precision monitoring, PTAs worldwide have uncovered evidence for a stochastic GWB. The first indication came from the NANOGrav 12.5-yr dataset [17],

<sup>(1)</sup> <https://africanpulsartiming.github.io>

which identified a common-spectrum red-noise process across its pulsars but could not yet confirm Hellings–Downs correlations. Contemporaneous analyses by the PPTA [18], EPTA [19], and IPTA [20] independently confirmed the presence of a common red-noise signal, establishing that this was not an artifact of a single dataset. The breakthrough came in 2023, when four collaborations reported evidence for spatial correlations consistent with a GWB: NANOGrav [21], the EPTA and InPTA [22], the PPTA [23], and the CPTA [24]. The IPTA, which combines datasets from all regional collaborations, is expected to deliver the most significant joint measurement [20] in the near future. Crucially, these recent datasets have begun to reveal the distinctive Hellings–Downs spatial correlations required to confirm the low-frequency PTA signal’s GW origin.

This evidence of a GWB opens a new window onto the dynamical Universe. The leading interpretation is that this background arises from the cosmic population of supermassive black hole binaries (SMBHBs) with masses of  $\sim 10^8\text{--}10^{10} M_\odot$ . These binaries form as a natural consequence of hierarchical galaxy mergers: following a merger, dynamical friction drives the two central black holes toward the center of the newly formed galaxy on timescales of  $\sim 100$  Myr - Gyrs. At parsec-scale separations, the binary must shed energy and angular momentum—via three-body stellar scattering or interactions with a circumbinary gas disk—to reach the sub-parsec regime where GW emission becomes efficient. This transition was long considered a potential bottleneck—the “final parsec problem” [25]—but the emerging GWB evidence implies that SMBHBs do indeed reach the GW-dominated regime, effectively ruling out severe stalling scenarios. During their slow GW-inspiral phase, these systems emit GWs with periods of years to decades. At the lowest accessible frequencies ( $\sim 2$  nHz), the background is formed by the incoherent superposition of signals from  $\sim 10^6$  binaries; at higher frequencies ( $\sim 20$  nHz), the population thins to  $\sim 10^3$  systems as binary evolution accelerates ( $df/dt \propto f^{11/3}$ ), see fig. 2. While SMBHBs are the standard astrophysical interpretation, the signal could also herald “New Physics,” potentially originating from cosmic strings, phase transitions in the early Universe, or primordial fluctuations [26, 27].

PTAs can detect these faint spacetime ripples by using millisecond pulsars in our own Galaxy as a GW detector. A passing GW with strain  $h \sim 10^{-15}$  induces timing residuals of order 100 ns over a decade-long baseline. Millisecond pulsars can reach this precision thanks to their rapid, stable rotation and low intrinsic spin-down noise, making them ideal clocks for GW detection. The sensitivity of a PTA is bounded by its total observation time ( $f_{\min} \sim 1/T_{\text{obs}}$ ) and observing cadence ( $f_{\max} \sim 1/\Delta t$ ), uniquely positioning PTAs to probe physics on timescales not accessible by any other means.

*State of the Art.* – In anticipation of a detection, the IPTA Detection Committee established a detection checklist [29]. Shortly after, independent analyses by NANOGrav [21], EPTA+InPTA [22], PPTA [23], CPTA [24], all reported the presence of a common-spectrum process with the expected Hellings–Downs angular correlations. The recent results from the MPTA [30], which reported evidence for the GWB using only 4.5 years of data but an impressive sample of 83 pulsars, further strengthen this global effort. Should these emerging PTAs join the IPTA, the inclusion of their additional southern-hemisphere pulsars with small residuals would be particularly valuable for improving the sky coverage, detection prospects for continuous GWs, and angular resolution of a combined analysis. Joint data will also be critical for GWB anisotropy searches, which require uniform sky coverage to distinguish an astrophysical background tracing large-scale structure from a nearly isotropic primordial signal (sect. 5).

A key advance since the first GWB evidence claims has been the development of in-

creasingly sophisticated custom noise models [31–33]. These models treat each pulsar’s red noise spectrum, chromatic interstellar medium variations, and potential instrumental systematics self-consistently within hierarchical Bayesian frameworks. Accurate noise characterization has become essential, as the inferred amplitude of the GWB, with a strain amplitude of  $A_{\text{GWB}} \sim 2.4 \times 10^{-15}$  [21], is near or above the upper end of predictions from many astrophysical models [34]. This apparent tension has motivated new theoretical work on the demographics and merger rates of SMBHBs, including the effects of environmental coupling, eccentricity evolution, and black hole mass scaling relations, e.g. Liepold and Ma (2024) [35]. It has also reinvigorated the search for cosmological sources, as the high amplitude could alternatively be explained by stable cosmic strings or phase transitions in the early Universe [26].

Recent astronomical discoveries have added further importance to the GWB evidence. High-redshift quasars observed at  $z \gtrsim 6$  appear to host black holes with masses exceeding  $10^9 M_{\odot}$  [36, 37], far earlier and more massive than expected from standard models of hierarchical growth, with James Webb Space Telescope (JWST) observations pushing this to  $z \approx 10$  [38]. If such systems are common, they would substantially increase the GW power produced throughout cosmic history, naturally explaining the elevated GWB amplitude observed by PTAs. At the same time, this scenario challenges our current understanding of black hole formation and galaxy evolution [34, 35, 39, 40].

Together with stochastic background analyses, PTAs have entered a new phase of targeted searches for CWs from individual SMBHBs. These efforts represent a major conceptual leap from the early era, when PTAs could only place upper limits on a candidate binary in 3C 66B [41], to today coordinated campaigns testing specific binary

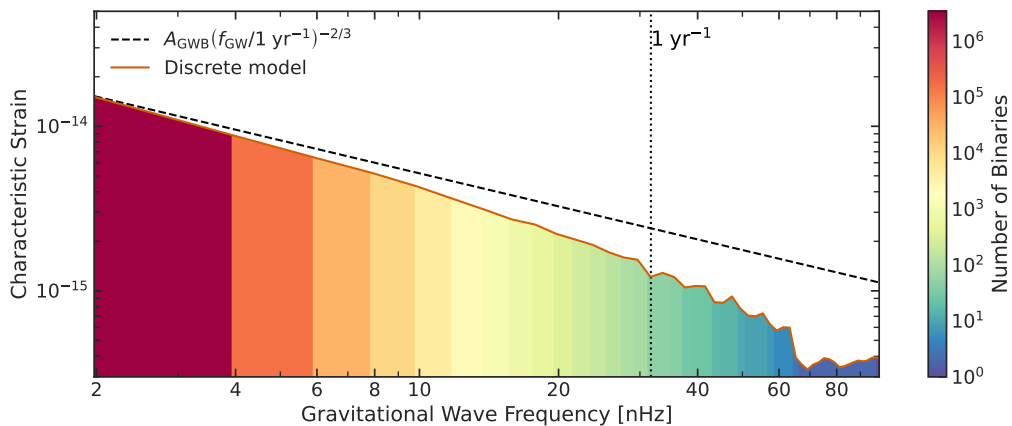


Fig. 2. – **The GWB in the PTA frequency band.** The characteristic strain spectrum of the GWB from a cosmic population of SMBHBs. At low frequencies the background is well approximated by a power law  $h_c \propto f^{-2/3}$ , representing the Phinney [11] ensemble average (i.e. the mean over many realizations). Since we observe a single realization of the Universe, the measured spectrum will be jagged, with excursions above and below this mean; the median spectrum (from discrete realizations of the GWB) may better represent what any one realization looks like, see e.g. [28]. The number of binaries per frequency bin,  $\Delta N(f)$ , drops steeply with frequency (eq. (7)): from  $\sim 10^6$  sources at 2 nHz to  $\sim 10^3$  at 20 nHz, because higher-frequency binaries are more massive and rarer, and they evolve through each bin more quickly ( $\dot{f} \propto f^{11/3}$ ). This steep decline marks the transition from a confusion-dominated stochastic regime to one where individual binaries become resolvable as CW sources (sect. 6) and the background develops measurable anisotropy (sect. 5).

hypotheses in well-identified active galactic nuclei (AGN). The recent NANOGrav targeted search [42] established the first systematic framework for evaluating individual candidates, using two candidates that stood out of the 114 as case studies for a detection protocol. To date, no CW detection has been made by any GW detector across the entire frequency spectrum. To accelerate these multi-messenger efforts, the community is developing rapid data combination frameworks which allow for PTA analyses on timescales of months rather than years.

*Scope of this review.* – Several complementary reviews of nanoHertz GW science have appeared recently. Sesana & Figuera [27] provide a thorough treatment of the GWB source physics, covering both the astrophysical signal from SMBHBs, including eccentricity, environmental coupling, and sparse sampling, as well as early-Universe backgrounds from inflation, phase transitions, and topological defects. Taylor [43] gives a broad overview of PTA data analysis and astrophysical interpretation in the post-evidence era. Shaifullah [44] focuses on the observational and instrumental landscape, summarizing the techniques behind sub-microsecond timing precision and the challenges posed by noise modeling, interstellar propagation, and Solar system ephemeris uncertainties. Liu & Chen [45] survey the past decade of PTA progress, covering advances in instrumentation, data-analysis techniques, and the path from progressively tighter upper limits to the 2023 Hellings–Downs detection. The present review is intended to complement these works. Our emphasis is on the mathematical formalism underlying PTA searches—the spatial correlation signatures of GWs, and their harmonic decomposition—and on the methodologies for detecting and characterizing both the stochastic background and individual sources. We give particular attention to GWB anisotropy, multi-messenger CW searches, and the role of the IPTA. We also discuss new physics, including alternative GW polarizations and ultralight dark matter, and the observational prospects opened by next-generation instruments.

As PTA baselines lengthen, noise modeling becomes increasingly precise, and targeted searches mature into a detection framework, the field is transitioning from evidence for a GWB to astrophysical inference and toward the first direct discovery of a SMBHB in its host galaxy. This review summarizes the status of the field in this new era. A list of common acronyms is given in tab. I. In sect. 2, we present an order-of-magnitude derivation of the GWB stochasticity before developing the formalism underlying GWB searches, including the derivation of the Hellings–Downs curve and the cross-correlation methods used to extract the signal. Sect. 3 reviews predictions and current observational constraints on the GWB amplitude and spectrum while sect. 4 covers astrophysical modeling of the SMBHB population. Sect. 5 addresses how we search for GWB anisotropy and how it scales. In sect. 6, we turn our attention to targeted CW searches for individual binaries, including multi-messenger detection frameworks, and in sect. 7 we discuss the angular resolution of PTAs. Sect. 8 examines prospects for probing new physics. Turning our focus to the detector aspects of PTAs, in sect. 9 we examine pulsar noise models, while sect. 10 describes the IPTA and new rapid data combination methods. Sect. 11 highlights some (certainly not all) complementary science, and we conclude with an outlook for the field in sect. 12.

## 2. – The Gravitational Wave Background

The search for a stochastic GWB relies on identifying a common signal correlated across the PTA. We begin in sect. 2.1 with an original order-of-magnitude derivation of the GWB stochasticity, showing from first principles why the nanoHertz background is

indeed a confusion-limited signal. Several scaling laws here may be useful for the reader in general. We then derive the response of a single pulsar to a GW, construct the cross-correlation statistic that isolates the GWB from intrinsic noise, and derive the expected spectral and spatial signatures of the signal.

**2.1. Why the nanoHertz GWB is stochastic.** – A useful way to distinguish a genuinely stochastic (confusion) background from a set of individually resolvable binaries is to compute the duty cycle (or occupancy) per frequency bin,  $\Delta N(f)$ . Here  $\Delta N(f)$  is the expected number of binaries whose gravitational radiation lies in a single Fourier bin centered at frequency  $f$ , at any given time. This basic resolvability criterion, and its relation to Gaussian versus non-Gaussian (“popcorn”) regimes, is widely discussed in the literature, see e.g. [46–49]. If  $\Delta N \sim 1$ , bins are typically empty or contain a single system. Individual sources are, in principle, resolvable. If  $\Delta N \gg 1$ , many systems contribute to each bin. Their phases are effectively uncorrelated, and the sum behaves as confusion noise with approximately Gaussian statistics (by the Central Limit Theorem; see e.g. Ref. [48–50]), i.e. a stochastic background.

At the level of an order-of-magnitude estimate,  $\Delta N(f)$  is the product of the rate at which relevant binaries enter the observable Universe and the time a typical binary

TABLE I. – *List of acronyms used in this review.*

Acronym	Definition	Acronym	Definition
AGN	Active Galactic Nucleus	MCMC	Markov Chain Monte Carlo
ARN	Achromatic Red Noise	MPTA	MeerKAT Pulsar Timing Array
BiPOSH	Bipolar Spherical Harmonic	MSP	Millisecond Pulsar
CMB	Cosmic Microwave Background	NANOGrav	N. Amer. Nanohertz Obs. for GWs
CPTA	Chinese Pulsar Timing Array	ORF	Overlap Reduction Function
CRN	Common Red Noise	PBH	Primordial Black Hole
CURN	Common Uncorrelated Red Noise	PGW	Primordial Gravitational Wave
CW	Continuous Wave	PPTA	Parkes Pulsar Timing Array
DM	Dispersion Measure	PSD	Power Spectral Density
DSA-2000	Deep Synoptic Array 2000	PTA	Pulsar Timing Array
QCD	Quantum Chromodynamics		
EPTA	European Pulsar Timing Array	QLF	Quasar Luminosity Function
FAP	False Alarm Probability	RFI	Radio Frequency Interference
FoM	Figure of Merit	SKAO	Square Kilometre Array Observatory
FOPT	First-Order Phase Transition	SMBH	Supermassive Black Hole
GR	General Relativity	SMBHB	Supermassive Black Hole Binary
GSMF	Galaxy Stellar Mass Function	S/N	Signal-to-Noise Ratio
GW	Gravitational Wave	SSB	Solar System Barycenter
GWB	Gravitational Wave Background	SW	Solar Wind
HD	Hellings and Downs	SWGPs	Solar Wind Gaussian Process
InPTA	Indian Pulsar Timing Array	TOA	Time of Arrival
IPTA	International Pulsar Timing Array	ULDM	Ultralight Dark Matter
IRN	Intrinsic Red Noise	VDF	Velocity Dispersion Function
ISCO	Innermost Stable Circular Orbit	VLBI	Very Long Baseline Interferometry
ISM	Interstellar Medium	LSS	Large-Scale Structure

spends in one frequency bin:

$$(1) \quad \Delta N(f) \approx \underbrace{\dot{N}}_{\text{Cosmic merger rate}} \times \underbrace{\tau_{\text{res}}(f)}_{\text{Residence time}} .$$

For PTAs, the dominant contribution to the background is expected from SMBHBs produced in galaxy mergers, with much of the signal power arising from redshifts  $z \sim 1-2$  (e.g. Ref. [40, 46, 47]). A simple estimate of the all-sky merger rate is obtained by multiplying a comoving merger-rate density by the relevant comoving volume:

1. **Volume ( $V_c$ ):** take the comoving volume out to  $z \approx 2$  as  $V_c \approx 500 \text{ Gpc}^3$  .
2. **Merger-rate density ( $\mathcal{R}$ ):** adopt a characteristic rate density for massive galaxies hosting  $\mathcal{M} > 10^8 M_\odot$  black holes,  $\mathcal{R} \sim 2 \times 10^{-2} \text{ Gpc}^{-3} \text{ yr}^{-1}$  [39] (Equivalently,  $\sim 2 \times 10^{-5}$  mergers per  $\text{Mpc}^3$  per Gyr.)
3. **Total rate:** the integrated rate over the volume is then  $\dot{N} \approx V_c \times \mathcal{R} \approx (500) \times (0.02) \approx 10$  mergers/year

The merger-rate density here should be viewed as a fiducial, order-of-magnitude normalization inferred from observationally anchored galaxy-merger models (galaxy stellar-mass function  $\times$  pair fraction  $\times$  merger timescale) and the assumption that SMBH coalescences broadly track massive galaxy mergers, up to uncertain delays or stalling [51]. The key point is that, while a merger is rare for any one galaxy, the cosmic rate integrated over the observable volume is non-negligible.

A binary appears effectively monochromatic if its frequency drift over the observing span is small compared to the Fourier resolution. For an observation time  $T_{\text{obs}}$  (typically  $\sim 10$  yr for PTA data sets), the bin width is

$$(2) \quad \Delta f = \frac{1}{T_{\text{obs}}} \approx 3 \times 10^{-9} \text{ Hz} .$$

Gravitational radiation causes the GW frequency to increase at a rate  $\dot{f}$ . The residence time in one bin is therefore

$$(3) \quad \tau_{\text{res}} \approx \frac{\Delta f}{\dot{f}} = \frac{1}{T_{\text{obs}} \dot{f}} .$$

In General Relativity (GR), the leading-order frequency evolution is

$$(4) \quad \dot{f} = \frac{96}{5} \pi^{8/3} \left( \frac{GM}{c^3} \right)^{5/3} f^{11/3} .$$

For a representative supermassive binary with  $\mathcal{M} \sim 10^9 M_\odot$  emitting near  $f \sim 10^{-8}$  Hz (10 nHz), this gives  $\dot{f} \approx 8.5 \times 10^{-5}$  nHz/yr. Substituting into the residence-time estimate,

$$(5) \quad \tau_{\text{res}} \approx \frac{3 \times 10^{-9} \text{ Hz}}{2.7 \times 10^{-21} \text{ Hz/s}} \approx 1.1 \times 10^{12} \text{ s} \approx 35,000 \text{ years} .$$

Although the data span is only  $\mathcal{O}(10)$  years, the inspiral is so slow at nanoHertz frequencies that a typical system can remain in a single Fourier bin for  $\sim 10^4$  years.

Combining the cosmic rate and the residence time,  $\Delta N = \dot{N} \times \tau_{\text{res}}$ . Using the numerical estimates above,

$$(6) \quad \Delta N \approx (10 \text{ yr}^{-1}) \times (35,000 \text{ yr}) = 3.5 \times 10^5.$$

Equivalently, one may highlight the parameter dependence by combining  $\Delta N \approx \dot{N}/(T_{\text{obs}}\dot{f})$  with the quadrupole scaling  $\dot{f} \propto \mathcal{M}^{5/3} f^{11/3}$ , which yields

$$(7) \quad \Delta N \sim 4 \times 10^5 \left( \frac{\mathcal{M}}{10^9 M_{\odot}} \right)^{-5/3} \left( \frac{f}{10^{-8} \text{ Hz}} \right)^{-11/3} \left( \frac{T_{\text{obs}}}{10 \text{ yr}} \right)^{-1}.$$

At nanoHertz frequencies ( $f \sim 10^{-8}$  Hz),  $\Delta N \approx 3.5 \times 10^5 \gg 1$ . Hundreds of thousands of binaries contribute to each frequency bin, so the signal cannot be decomposed into individual systems. Instead, the superposition of many weak, slowly evolving binaries produces a confusion background with effectively stochastic statistics, i.e. the GWB measured by PTAs.

At higher frequencies, the steep dependence  $\Delta N \propto f^{-11/3}$  drives the occupancy downward, eventually reaching  $\Delta N \lesssim 1$ . This marks the transition from a confusion-dominated regime to a regime where individual CW sources can become resolvable, see e.g. Ref. [46, 47]. The exact frequency at which this happens is the subject of current research.

**2.2. PTA Response to GWs.** – We define a computational frame where the Earth is at the origin and pulsars are located at distances  $L$  in directions  $\hat{p}$ . The response of a PTA to a passing GW is quantified by the fractional frequency shift,  $z(t, \hat{\Omega})$ , induced in the timing residuals. This shift arises from the metric perturbation  $h_{ij}$  at the Earth and the pulsar, resulting in a “two-term” response function [1, 5, 52]:

$$(8) \quad z(t, \hat{\Omega}) = \frac{1}{2} \frac{\hat{p}^i \hat{p}^j}{1 + \hat{\Omega} \cdot \hat{p}} \left[ h_{ij}(t, \hat{\Omega}) - h_{ij}(t_p, \hat{\Omega}) \right].$$

The physical mechanism of PTA detection relies on the fact that a GW perturbs the spacetime metric along the photon’s entire path from the pulsar to the Earth. The total timing residual is formally the integral of the metric perturbation  $h_{ij}$  along the line of sight. For a plane wave, this integral simplifies analytically to the difference between the metric perturbation at the two boundaries: the Earth and the Pulsar [5]. We can thus decompose the residual into two distinct components:

$$(9) \quad R(t) = R_E(t) - R_P(t_p),$$

where  $R_E(t)$  is the Earth term and  $R_P(t_p)$  is the Pulsar term. In practice, the Earth is not a fixed observatory: it orbits the Sun, introducing a time-varying geometric delay that would couple to the GW signal if left unmodeled. To remove this complication, all measured TOAs are first transformed to the Solar System Barycenter (SSB) using a Solar system ephemeris [13]. The SSB is where we could in principle balance the solar system on the tip of our finger. It serves as the common inertial reference point for a

PTA, so that “the Earth term” in eq. (9) really refers to the GW perturbation evaluated at the SSB.

In principle, once all TOAs are referred to the SSB, the array acts as a single detector at a common reference point: a passing GW perturbs the metric at the SSB, and this perturbation affects every pulsar’s TOA at the same instant. The timing residuals of all pulsars jump together, modulated only by each pulsar’s geometric antenna factor  $\hat{p}^i \hat{p}^j / (1 + \hat{\Omega} \cdot \hat{p})$ , which depends on the pulsar’s sky position relative to the GW propagation direction. It is this shared perturbation that gives rise to the Hellings and Downs spatial correlations, and in the limit of infinite pulsar distances [53], the GWB signal is essentially the auto-correlation of the Earth term.

In practice, achieving this common reference frame is a substantial undertaking, particularly for the IPTA, which must combine data from telescopes with different backends, calibration procedures, and TOA modeling choices (see sect. 10).

The Pulsar term,  $R_P(t_p)$ , represents the imprint of the GW field at the location of the pulsar itself. However, due to the finite speed of light, we observe this imprint with a significant time delay. The time at which the GW passed the pulsar,  $t_p$ , is related to the observation time  $t$  by:

$$(10) \quad t_p = t - \tau_a = t - \frac{L_a}{c} (1 + \hat{\Omega} \cdot \hat{p}),$$

where  $L_a$  is the pulsar distance,  $\hat{p}$  is the unit vector pointing to the pulsar, and  $\hat{\Omega}$  is the propagation direction of the GW.

Since pulsars are located at typical distances of  $L_a \sim 1$  kpc ( $\sim 3000$  light-years), the delay  $\tau_a$  is on the order of thousands of years. Furthermore, because every pulsar is at a different distance, the phase of the GW field at each pulsar is effectively random relative to the others. Consequently, the pulsar terms are uncorrelated between different pulsars. In stochastic background searches, the pulsar term therefore acts as an additional source of variance that does not contribute to the cross-correlation signal.

Despite this, the pulsar term carries unique astrophysical information. Since the pulsar term samples the GW field thousands of years in the past when it transited the pulsar, comparing the Earth and pulsar terms for a resolved CW source amounts to measuring the binary’s orbital evolution over thousands of years—effectively turning the PTA into a time machine (sect. 6.11). Furthermore, if pulsar distances can be measured to within a GW wavelength (e.g. via VLBI parallax), the pulsar term can be phased coherently, roughly doubling the effective signal power [54] and transforming the array into a true interferometer with a Galactic-scale baseline [55], dramatically improving sky localization (sect. 7).

**2.3. The General Plane Wave Framework.** – We now formalize the above by writing the metric perturbation as a general plane wave expansion. Any GW signal—whether from a single source or a superposition of many—can be decomposed as:

$$(11) \quad h_{ij}(t, \mathbf{x}) = \sum_A \int_{-\infty}^{\infty} df \int_{S^2} d\hat{\Omega} h_A(f, \hat{\Omega}) e^{i2\pi f(t - \hat{\Omega} \cdot \mathbf{x})} e_{ij}^A(\hat{\Omega}),$$

where  $f$  is the GW frequency,  $A = \{+, \times\}$  labels the polarization degrees of freedom,  $S^2$  indicates that the integral is performed on the two-sphere,  $\hat{\Omega}$  is a unit vector identifying the GW propagation direction,  $e_{ij}^A$  is the polarization tensor, and  $h_A$  is the amplitude.

In GR the sum runs over the two tensor polarizations  $A = \{+, \times\}$ ; alternative theories of gravity can introduce up to four additional modes (scalar and vector), each with a distinct polarization tensor and antenna pattern. These non-Einsteinian polarizations modify the Overlap Reduction Function (ORF) and are discussed in sect. 8.

The two-point function of a stationary, Gaussian, and unpolarized background reads:

$$(12) \quad \langle h_A^*(f, \hat{\Omega}) h_{A'}(f', \hat{\Omega}') \rangle = \delta^D(\hat{\Omega} - \hat{\Omega}') \delta_{AA'}^K \delta^D(f - f') H(f, \hat{\Omega}),$$

where  $\delta^K$  and  $\delta^D$  are Kronecker and Dirac deltas, respectively, and  $H(f, \hat{\Omega})$  is the one-sided power spectral density of the background. The ensemble average  $\langle \dots \rangle$  is performed over all realizations of the source population. The power spectrum can be factorized as  $H(f, \hat{\Omega}) = H(f)P(\hat{\Omega})$ , where  $H(f)$  describes the spectral content and  $P(\hat{\Omega})$  describes the angular distribution of GWB power, normalized so that  $\int_{S^2} P(\hat{\Omega}) d\hat{\Omega} = 4\pi$ . For a population of circular, GW-driven binaries  $H(f)$  follows a power law corresponding to  $h_c \propto f^{-2/3}$  [11], but environmental hardening mechanisms—stellar scattering and circumbinary gas torques—modify the spectral shape at low frequencies by altering the binary residence time in each frequency bin. These effects and the resulting  $da/dt$  contributions are detailed in sect. 4. For an isotropic background,  $P(\hat{\Omega}) = 1$ ; deviations from isotropy are the subject of sect. 5.

The timing residual induced in pulsar  $a$  by this background is:

$$(13) \quad R_a^{\text{GW}}(t) = \int df \frac{1}{2\pi i f} \int_{S^2} d\hat{\Omega} \sum_A h_A(f, \hat{\Omega}) F_a^A(\hat{\Omega}) \left(1 - e^{-2\pi i f L_a(1 + \hat{\Omega} \cdot \hat{p}_a)}\right) e^{2\pi i f t},$$

where  $L_a$  is the pulsar distance,  $\hat{p}_a$  is the direction to the pulsar, and

$$(14) \quad F_a^A(\hat{\Omega}) \equiv \frac{\hat{p}_a^i \hat{p}_a^j}{2(1 + \hat{\Omega} \cdot \hat{p}_a)} e_{ij}^A(\hat{\Omega})$$

is the antenna beam pattern function [56], which encodes the geometric sensitivity of the pulsar to GWs from direction  $\hat{\Omega}$ . The term in parentheses in eq. (13) is the difference between the Earth term (unity) and the Pulsar term (exponential) discussed above.

The cross-correlation of the timing residuals between pulsars  $a$  and  $b$  is then (taking the conjugate of pulsar  $b$ 's residual, so that the  $1/(2\pi i f)$  prefactors yield a real  $1/(2\pi f)^2$ ):

$$(15) \quad \langle R_a(f) R_b^*(f) \rangle = \frac{1}{(2\pi f)^2} H(f) \int_{S^2} d\hat{\Omega} P(\hat{\Omega}) \kappa_{ab}(f, \hat{\Omega}) \left[ \sum_A F_a^A(\hat{\Omega}) F_b^A(\hat{\Omega}) \right],$$

where  $\kappa_{ab}$  encodes the Earth–Pulsar term interference:

$$(16) \quad \kappa_{ab}(f, \hat{\Omega}) \equiv \left(1 - e^{-2\pi i f L_a(1 + \hat{\Omega} \cdot \hat{p}_a)}\right) \left(1 - e^{2\pi i f L_b(1 + \hat{\Omega} \cdot \hat{p}_b)}\right).$$

In the short-wavelength (incoherent) limit  $fL_a \gg 1$ , the pulsar terms average out and  $\kappa_{ab} \approx (1 + \delta_{ab})$  [53, 57]. In this limit, setting  $P(\hat{\Omega}) = 1$  and performing the sky integral, eq. (15) reduces to

$$(17) \quad \langle R_a(f) R_b^*(f) \rangle = \frac{H(f)}{(2\pi f)^2} \Gamma_{ab},$$

where  $\Gamma_{ab}$  is the ORF. The one-sided power spectral density  $H(f)$  is related to the characteristic strain by  $H(f) = h_c^2(f)/(12\pi^2 f^3)$  (see e.g. Ref. [11]), so the cross-power spectral density of the timing residuals can be written equivalently as

$$(18) \quad S_{ab}(f) = \frac{1}{12\pi^2 f^3} h_c^2(f) \Gamma_{ab}.$$

This connects the observable cross-correlated residuals directly to the GWB strain spectrum and the geometric response of the array. Note that  $S_{ab}$  has dimensions of  $\text{s}^3$  (or equivalently  $\text{yr}^3$ ), which is perhaps more intuitive when read as  $\text{s}^2/\text{Hz}$ : it is a power spectral density of a quantity (timing residuals) with dimensions of time. It is here that the two common spectral parameterizations present themselves: for a GW-driven circular binary population  $h_c(f) \propto f^{-2/3}$  (spectral index  $\alpha = -2/3$ ), the  $1/f^3$  prefactor converts this to a power spectral density  $S_{ab} \propto f^{-13/3}$  (spectral index  $\gamma = 13/3$ ). When plotting in residual space, the timing residual amplitude is  $\sqrt{S_{ab}(f)/T_{\text{obs}}}$ , which gives the residual rms on the  $y$ -axis in e.g. free spectral models.

Eq. 18 makes explicit that the cross-power factorizes into two independently measurable components: the ORF  $\Gamma_{ab}$ , which encodes the spatial correlations between pulsar pairs as a function of their angular separation, and the characteristic strain spectrum  $h_c(f)$ , which encodes the spectral content of the background. Both must be detected to claim a GWB: a common red-noise spectrum across pulsars without the Hellings-Downs spatial correlations could be mimicked by spatially correlated noise, while the angular pattern alone without a consistent spectrum would lack physical interpretation. We derive the ORF in the following section (sect. 2.4), and then turn to the characteristic strain spectrum in sect. 2.5.

**2.4. Derivation of the Hellings and Downs Curve.** – The ORF,  $\Gamma_{ab}$ , introduced in eq. (18), quantifies the geometric response of the array. To derive it, we define a frame where pulsar  $a$  lies on the  $z$ -axis and pulsar  $b$  lies in the  $x - z$  plane at an angular separation  $\zeta$  (see fig. 3). The GW propagation direction  $\hat{\Omega}$  is defined by polar angles  $(\theta, \phi)$ .

The coordinate system is defined as:

$$\begin{aligned} \hat{m} &= (\sin \phi, -\cos \phi, 0), \\ \hat{n} &= (\cos \theta \cos \phi, \cos \theta \sin \phi, -\sin \theta), \\ \hat{\Omega} &= (\sin \theta \cos \phi, \sin \theta \sin \phi, \cos \theta), \\ \hat{p}_a &= (0, 0, 1), \\ \hat{p}_b &= (\sin \zeta, 0, \cos \zeta). \end{aligned}$$

The response of a pulsar to a GW is governed by the antenna beam patterns  $F^+(\hat{\Omega})$  and  $F^\times(\hat{\Omega})$ . For pulsar  $a$  on the  $z$ -axis:

$$(19) \quad F_a^+ = -\frac{1}{2}(1 - \cos \theta)$$

$$(20) \quad F_a^\times = 0$$

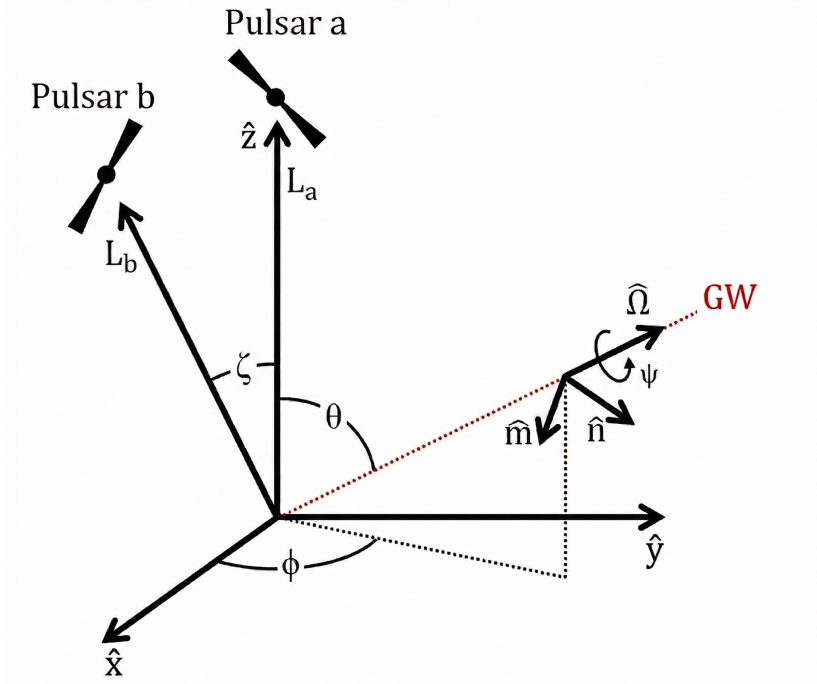


Fig. 3. – Computational frame used to define the ORF(s). Pulsar *a* lies at distance  $L_a$  on the  $+\hat{z}$  axis and pulsar *b* lies at distance  $L_b$  in the  $x$ - $z$  plane at an angular separation  $\zeta$ . The GW propagation direction  $\hat{\Omega}$  is specified by polar angle  $\theta$  and azimuthal angle  $\phi$  with respect to  $+\hat{z}$ . The principal polarization axes  $\hat{m}$  and  $\hat{n}$  are perpendicular to  $\hat{\Omega}$ , with  $\hat{m} \times \hat{n} = \hat{\Omega}$ , and define the  $+$  and  $\times$  polarization tensors that enter the antenna beam pattern  $F_a^A(\hat{\Omega})$  (eq. (14)). The polarization angle  $\psi$  rotates  $(\hat{m}, \hat{n})$  about  $\hat{\Omega}$  (sect. 6'2). This geometry determines the antenna pattern functions  $F_a^A$  and  $F_b^A$  and hence any spatial correlation.

For pulsar *b*, located at angle  $\zeta$ , the antenna patterns are more complex due to the rotation:

$$(21) \quad F_b^\times = \frac{(\sin \phi \sin \zeta)(\cos \theta \sin \zeta \cos \phi - \sin \theta \cos \zeta)}{1 + \cos \theta \cos \zeta + \sin \theta \sin \zeta \cos \phi},$$

$$(22) \quad F_b^+ = \frac{1}{2} \frac{(\sin \phi \sin \zeta)^2 - (\sin \zeta \cos \theta \cos \phi - \sin \theta \cos \zeta)^2}{1 + \cos \theta \cos \zeta + \sin \theta \sin \zeta \cos \phi}.$$

It is important to note that these specific patterns arise from the transverse-traceless tensor nature of GWs in GR. Alternative theories of gravity can predict up to four additional polarization modes (scalar and vector), which would possess distinct antenna patterns  $F^S(\hat{\Omega})$  and  $F^V(\hat{\Omega})$ . These alternative modes result in different angular correlation structures (e.g., monopolar or dipolar correlations) when integrated over the sky. We discuss the search for these beyond-GR signatures, including scalar “breathing” modes, in sect. 8.

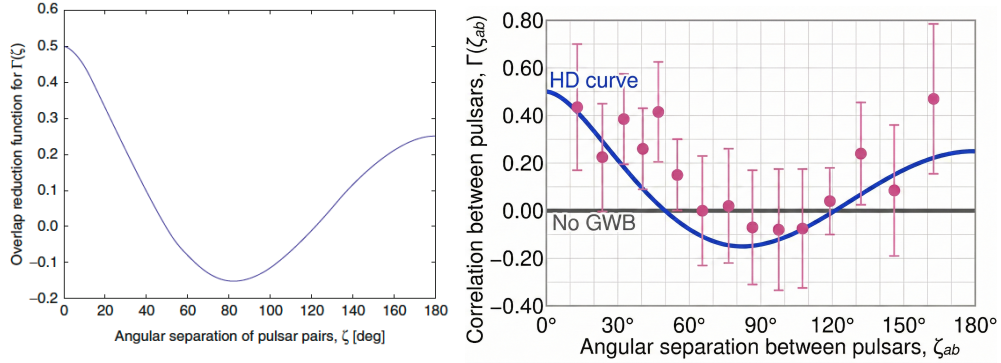


Fig. 4. – Left: The ORF for an isotropic stochastic GWB, called the Hellings and Downs curve. Right: The optimal statistic [52, 58] result for the GWB search from Agazie et al. [21]. The quantity actually plotted on the  $y$ -axis is  $\hat{A}^2 \Gamma_{ab}$ , where  $\hat{A}^2 \sim 10^{-30}$  is the maximum-likelihood estimator of the squared GWB amplitude; the axis label shows only  $\Gamma(\zeta_{ab})$  for presentation clarity. The binning of pulsar pairs by angular separation is for visual clarity only and has no bearing on the result.

The ORF is the sky-averaged product of these antenna patterns:

$$(23) \quad \Gamma_{ab} = \frac{1}{4\pi} \int_{S^2} d\hat{\Omega} (F_a^+ F_b^+ + F_a^\times F_b^\times)$$

The integrand—the product of beam patterns evaluated at a fixed sky direction  $\hat{\Omega}$ —is the single-source ORF  $\Upsilon_{ab}(\hat{\Omega})$ , the deterministic “fingerprint” of an individual GW source on the pulsar pair. The Hellings-Downs curve is thus the sky average of these fingerprints. We derive a closed-form expression for  $\Upsilon_{ab}$  in sect. 6.7.

Substituting the geometric expressions and integrating over  $\theta \in [0, \pi]$  and  $\phi \in [0, 2\pi]$  yields the standard analytic form for the Hellings and Downs correlation [6]:

$$(24) \quad \Gamma_{ab} = (1 + \delta_{ab}) \frac{1}{2} - \frac{1}{4} \left( \frac{1 - \cos \zeta}{2} \right) + \frac{3}{2} \left( \frac{1 - \cos \zeta}{2} \right) \ln \left( \frac{1 - \cos \zeta}{2} \right).$$

This form is normalized to 0.5 at  $\zeta \sim 0$  for distinct pulsars so that the autocorrelation yields 1.0, consistent with the standard literature.

This curve (fig. 4) is the “smoking gun” signature of a GWB. It features a maximum correlation of 0.5 at  $\zeta \sim 0^\circ$  (for distinct pulsars) and a minimum near  $\zeta \approx 90^\circ$ . For pulsars with small angular separations, the timing residuals are positively correlated (the pulsars appear to “bob” in sync). As the separation increases, the correlation drops, becoming negative at separations of  $\sim 90^\circ$ , before becoming positive again at wider angles.

Standard analyses often model the ORF assuming the pulsar term contribution averages to zero [53]. However, a rigorous treatment, as detailed in [57], includes the interference effects from the pulsar term, denoted as  $\kappa_{ab}$ . It has been shown that at low frequencies, where the gravitational wavelength is comparable to the separation between pulsars, the pulsar term does not simply vanish. Instead, it introduces Bessel function oscillations around the standard Hellings-Downs solution at small angles. While current PTAs often neglect this effect for typical angular separations, it becomes non-negligible

for pulsars with very small separations, such as those found in globular clusters or in double pulsar systems where both pulsars are being timed.

An alternative and concise derivation of the Hellings and Downs curve, avoiding any choice of coordinate frame, was given by Ali-Haïmoud, Smith & Mingarelli [59]. Defining  $x \equiv \hat{p}_a \cdot \hat{\Omega}$ ,  $y \equiv \hat{p}_b \cdot \hat{\Omega}$ , and  $\mu \equiv \cos \zeta = \hat{p}_a \cdot \hat{p}_b$ , the pairwise timing response function (eq. (15)) integrated over the sky can be split as

$$(25) \quad \mathcal{H}(\mu) = \mathcal{J}(\mu) + (1 + \mu/3),$$

where the first term collects the nontrivial part of the integral:

$$(26) \quad \mathcal{J}(\mu) \equiv 2 \int \frac{d^2 \hat{\Omega}}{4\pi} \frac{x^2 + y^2 - 2\mu xy - (1 - \mu^2)}{(1+x)(1+y)}.$$

The key is to change variables from sky coordinates to  $(x, y)$ , which are constrained to an ellipse  $x^2 + y^2 - 2\mu xy < 1 - \mu^2$ , with area element  $d^2 \hat{\Omega} = 2 dx dy / \sqrt{1 - \mu^2 - x^2 - y^2 + 2\mu xy}$ . This reduces  $\mathcal{J}$  to a factorized double integral: for fixed  $x$ , the inner integral over  $y$  evaluates to  $|x + \mu| - (1 + \mu x)$ , and the remaining outer integral over  $x$  yields  $\mathcal{J}(\mu) = 2(1 - \mu) \ln[(1 - \mu)/2]$ . Combining gives the Hellings and Downs function in the compact form

$$(27) \quad \mathcal{H}(\mu) = \frac{3 + \mu}{3} + 2(1 - \mu) \ln\left(\frac{1 - \mu}{2}\right).$$

Note that this expression follows the normalization convention of Ref. [59], in which  $\mathcal{H}(1) = 4/3$ ; to recover the standard normalization used earlier in this review, where  $\Gamma_{ab} = 1/2$  at  $\zeta \sim 0$  for distinct pulsars and  $\Gamma_{ab} = 1$  for the autocorrelation, one identifies  $\Gamma_{ab} = \frac{1}{2}(1 + \delta_{ab}) \mathcal{H}(\mu)/\mathcal{H}(1) = \frac{3}{8}(1 + \delta_{ab}) \mathcal{H}(\mu)$ . This frame-independent approach also generalizes naturally to anisotropic backgrounds, as discussed in sect. 5.

While the standard analysis assumes the specific shape of the Hellings-Downs curve, a more agnostic approach is to decompose the spatial correlations into a basis of Legendre polynomials,  $P_\ell(\cos \zeta_{ab})$ . Roebber & Holder [60] showed that the angular power spectrum of the PTA redshift map is the harmonic transform of the Hellings-Downs curve, demonstrating that the quadrupole carries the dominant sensitivity. Building on these foundations, Nay et al. [61] developed a complete harmonic analysis framework for PTAs that enables model-independent reconstruction of the ORF directly from the timing residuals. By measuring the Legendre coefficients  $C_\ell$ , one can rigorously test for the presence of the quadrupolar ( $\ell = 2$ ) signature predicted by GR without assuming it *a priori*. This formalism was already mature by the time the NANOGrav 15-yr GWB evidence was published, and was cited in the GWB evidence paper itself [21].

The NANOGrav collaboration applied this harmonic analysis to the 15-yr dataset [62], providing an important and independent measurement of the GWB. They found that the data disfavor a purely monopolar or dipolar structure and are consistent with the Hellings-Downs prediction, although the recovery of the exact quadrupolar shape is currently limited by the number of unique pulsar pairs at small angular separations. This independent measurement technique offers direct insight into the structure of the Hellings-Downs curve itself: by reconstructing the ORF multipole by multipole, harmonic analysis can reveal deviations from GR, constrain alternative polarization content, and

probe frequency-dependent modifications to the spatial correlations that would otherwise be invisible. It can also distinguish the GWB from correlated noise sources like clock errors ( $\ell = 0$ ) or ephemeris drift ( $\ell = 1$ ), see e.g. Tiburzi et al. [63], providing an independent verification of the GWB evidence.

**2.5. The Characteristic Strain Spectrum.** – Assuming this background is dominated by circular, inspiraling SMBHBs, the strain from a single binary is given by [64]:

$$(28) \quad h = \frac{8\pi^{2/3} \mathcal{M}^{5/3}}{10^{1/2} D_L(z)} f_r^{2/3},$$

where  $\mathcal{M}$  is the chirp mass,  $D_L(z)$  is the luminosity distance, and  $f_r = f(1+z)$  is the rest-frame frequency.

The total energy density of the background  $\rho_{\text{GW}}$  is related to the characteristic strain by [11, 46]:

$$(29) \quad \frac{d\rho_{\text{GW}}}{d\ln f} = \frac{\pi}{4} f^2 h_c^2(f).$$

By integrating the comoving number density of mergers  $\dot{\phi}_{\text{BHB}}(z)$ , we arrive at the standard power-law representation for the characteristic strain:

$$(30) \quad h_c^2(f) = \frac{4}{3\pi^{1/3}} \frac{1}{f^{4/3}} \iint \frac{\mathcal{M}^{5/3}}{(1+z)^{1/3}} \dot{\phi}_{\text{BHB}}(\mathcal{M}, z) \frac{dt_r}{dz} d\log_{10} \mathcal{M} dz.$$

Measuring  $h_c$  is therefore a direct probe of the physics in the double integral above, eq. (30): the SMBHB merger rate density  $\dot{\phi}_{\text{BHB}}$  and, critically, the chirp mass distribution [65–67]. The steep  $\mathcal{M}^{5/3}$  scaling of the integrand makes the chirp mass the dominant factor governing the GWB amplitude, and therefore the most important parameter for forward models of the SMBHB population [40]. This integration yields the characteristic power-law slope  $h_c(f) = A_{\text{yr}}(f/f_{\text{yr}})^{-2/3}$  for astrophysical GWB searches.

**2.6. A discrete population of SMBHBs.** – It is important to recognize that the characteristic strain spectrum  $h_c(f) \propto f^{-2/3}$  derived above represents the ensemble average of the GW energy density [11]. However, we inhabit a single realization of the Universe containing a finite, discrete population of binaries. We observe a single realization rather than an ensemble, so the measured strain spectrum will be jagged, with overdensities and underdensities relative to the smooth  $f^{-2/3}$  power law (see fig. 2).

This deviation arises from the frequency-dependent source count per frequency bin,  $\Delta N(f)$ . At low frequencies,  $\Delta N \gg 1$ , and the superposition of many sources produces Gaussian statistics where the mean and median strain converge. At high frequencies, the rapid evolution of binaries ( $df/dt \propto f^{11/3}$ ) drives the occupancy  $\Delta N$  unity or below: the expected number of SMBHBs drops from  $\sim 10^6$  at 2 nHz to  $\sim 10^3$  at 20 nHz. In this shot-noise regime, a given frequency bin is dominated by perhaps one loud source, and the median strain—which characterizes the typical bin in our realization—diverges from the ensemble mean. Sesana et al. [46] first identified this spectral break, referring to it as a “knee” in the characteristic strain spectrum where the transition from the continuous to discrete regime occurs, predicting  $f_{\text{knee}} = 37_{-13}^{+15}$  nHz.

Using a semi-analytic SMBHB population model calibrated to the NANOGrav 15-yr GWB amplitude, Agazie et al. [28] carried out the first search for discreteness in real PTA data. They found that a broken power law provides a better fit to the GWB strain spectrum than a pure  $f^{-2/3}$  power law, with  $f_{\text{knee}} = 25_{-19}^{+42}$  nHz, consistent with the Sesana et al. prediction. Their analysis also identified a  $\sim 2\sigma$  excess at 16 nHz, consistent with the presence of a single loud SMBHB at that frequency (see sect. 6 for targeted and all-sky CW searches). However, unmodeled pulsar noise could also be responsible for this excursion; custom noise models (see sect. 9) will be essential for determining whether such features are astrophysical or pulsar noise/ISM related. Overall, the observed spectral excursions are fully consistent with expectations from a discrete SMBHB population, or additional unmodeled white noise, and require no additional physics.

The discreteness of the background carries a key diagnostic: a GWB that exhibits spectral irregularities at high frequencies must be astrophysical in origin, since primordial backgrounds from processes such as cosmic strings or phase transitions are formed by the superposition of vastly more sources and will appear smooth across the PTA band. Importantly, signs of discreteness in the GWB spectrum may be observable before either GWB anisotropy (sect. 5) or individually resolved CW sources, making spectral irregularities a near-term probe of the astrophysical nature of the signal. In this same regime, the background also acquires net polarization, since a small number of dominant sources each contribute a coherent polarization state (sect. 5.3).

### 3. – GWB Predictions and Limits

The path to the current GWB evidence has been shaped by a complex interplay between astrophysical theory and observational constraints. For nearly a decade, the field grappled with an apparent tension: while early models predicted a loud background, pulsar timing limits seemed to rule them out, driving theorists toward increasingly pessimistic scenarios. We now understand that this tension was largely illusory a product of both conservative astrophysical assumptions and subtle biases in early data analysis.

*The Foundational Era (1995–2013).* – The framework for the stochastic background was established in the 1990s and early 2000s. Foundational analytic work by Rajagopal & Romani [68] and Jaffe & Backer [69] demonstrated that the incoherent superposition of signals from cosmic binaries would result in a red noise spectrum with a characteristic strain  $h_c(f) \propto f^{-2/3}$  [11]. These early models, along with Wyithe & Loeb [70], predicted amplitudes in the range  $A_{\text{yr}} \sim 10^{-15}$ , setting the sensitivity targets for the first generation of PTA experiments.

The statistical toolkit for PTA searches was also rapidly maturing. van Haasteren et al. (2009) [71] performed the first Bayesian search for the GWB using real pulsar timing data, establishing the likelihood framework that underpins modern analyses. On the frequentist side, Anholm et al. (2009) [52] derived the optimal cross-correlation statistic in the frequency domain. Beyond detection, the groundwork for characterizing the GWB was also laid during this period. Mingarelli et al. (2013) [56] developed the spherical harmonic formalism for GWB anisotropy, quantifying the expected angular power spectrum from a discrete population of SMBHBs, while Taylor & Gair (2013)[72] introduced practical Bayesian search methods for these spherical harmonics. Furthermore, Lee, Jenet & Price (2008) [73] showed that PTAs are sensitive to non-Einsteinian GW polarizations—scalar and vector modes predicted by alternative theories of gravity—

and subsequently demonstrated that PTAs can constrain the graviton mass through the frequency-dependent dispersion it imprints on the ORF [73].

This era culminated in the semi-analytic synthesis of Sesana et al. (2008) and Sesana (2013) [39]. By anchoring binary merger rates to observed galaxy luminosity functions and assuming efficient evolution, these works established a standard benchmark of  $A_{\text{yr}} \approx 1 \times 10^{-15}$ .

*The “Stalling” Crisis (2014–2018).* – As PTAs collected more data without a detection, theoretical models shifted downward to accommodate the lack of a signal. It became clear that the transition from kpc-scale galaxy mergers to pc-scale binaries is not instantaneous. If the mechanisms for hardening the binary—dynamical friction, stellar scattering, and gas drag—are inefficient, the binary may stall at parsec separations (the “Final Parsec Problem”).

Even if binaries do merge, environmental coupling can attenuate the signal. Ravi et al. [51], Sampson et al. [74], and Dvorkin & Barausse [75] demonstrated that strong environmental coupling accelerates the inspiral at low frequencies, depleting the number of binaries radiating in the lower end of the PTA band. Large-volume hydrodynamical simulations such as Illustris [76] further suggested that realistic galactic timescales would suppress the amplitude to  $A_{\text{yr}} \sim 0.4 \times 10^{-15}$ —nearly an order of magnitude below the early predictions.

An important theoretical development during this period was the realization that triple SMBH interactions can resolve the final parsec problem. In hierarchical structure formation, sequential galaxy mergers naturally deliver a third black hole to the nucleus before the existing binary has coalesced. Bonetti et al. [77] modeled the post-Newtonian evolution of massive black hole triplets in galactic nuclei and showed that three-body interactions efficiently shrink the inner binary’s orbit, driving it into the GW-dominated regime. They established a robust lower limit of  $A_{\text{yr}} \gtrsim 10^{-16}$  for the stochastic GWB, demonstrating that even in the most pessimistic scenarios for stellar and gas-driven hardening, triplet interactions alone guarantee a detectable signal floor. Independently, Ryu et al. [78] studied the stellar-dynamical hardening of SMBHBs through direct  $N$ -body simulations of their interactions with the surrounding stellar environment, confirming that three-body stellar scattering efficiently extracts orbital energy and angular momentum from the binary. Their predicted GWB amplitude was consistent with the Bonetti et al. floor, reinforcing the conclusion that the final parsec problem does not prevent SMBHBs from reaching the GW-driven regime.

*The Noise Modeling Breakthrough (2020–2021)* . – While theorists were refining environmental models, a parallel breakthrough occurred in data analysis. For years, PTA upper limits (e.g., from PPTA and NANOGrav) appeared to rule out amplitudes above  $A_{\text{yr}} \sim 10^{-15}$ , reinforcing the pessimistic theoretical outlook (see Fig. 5 of [45] for a compilation of these limits over time). However, pivotal work by Hazboun et al. (2020) [79] and Goncharov et al. (2022) [80] revealed that these limits were artificially low due to these effects in pulsar noise modeling.

Hazboun et al. (2020) identified the problem from the prior side. They demonstrated that Bayesian priors on intrinsic pulsar red noise are critical to the recovered GWB upper limit. In previous analyses, standard uniform priors on the red noise amplitude and spectral index allowed the per-pulsar noise models to absorb power that was, in fact, common across the array. The noise models were effectively “eating” the GWB signal, biasing the recovered amplitude downward and producing overly stringent upper limits.

By systematically varying the prior choices and quantifying their impact on the common-process recovery, Hazboun et al. showed that the published NANOGrav limits could shift upward by factors of several once more physically motivated priors were adopted.

Goncharov et al. (2022) approached the problem from the model-selection side using PPTA data. Rather than focusing on priors, they showed that intrinsic spin noise in individual pulsars can be covariant with a spatially correlated common-spectrum process. When the noise model does not account for this covariance—for example, by fitting each pulsar independently before searching for a common signal—power can leak between the two components in either direction: the common process can be absorbed into individual noise terms (suppressing the GWB), or conversely, correlated pulsar noise can masquerade as a GWB signal. Their key contribution was demonstrating that a simultaneous, joint fit of individual pulsar noise and the common process is essential, and that the outcome depends sensitively on which pulsars are included and how their noise is modeled.

Together, these two studies revealed that previous PTA upper limits had been artificially aggressive. When the methodological biases were corrected through flexible hierarchical priors [81] and customized per-pulsar noise models [32], the observational constraints relaxed significantly, revealing that the GWB had likely been present in the data at  $A_{\text{yr}} \sim 2\text{--}3 \times 10^{-15}$  all along.

*The Modern Era (2021–Present).* – With the observational ceiling lifted, the theoretical landscape has realigned around high-amplitude models. The current GWB evidence is best explained by models that emphasize the contribution of the most massive black holes ( $M_{\text{BH}} > 10^9 M_{\odot}$ ). Forward models anchored to the Velocity Dispersion Function (VDF) [82, 83] naturally predict higher amplitudes than traditional GSMF-based approaches, as the tighter  $M_{\text{BH}}\text{--}\sigma$  relation avoids the upward scatter of low-mass galaxies that can bias stellar-mass-based estimates (see sect. 4 for a detailed comparison). This preference for massive black hole populations is supported by recent JWST observations, described above. Objects such as GN-z11 [84] exhibit black hole masses that are over-massive relative to their host galaxies compared to local scaling relations, suggesting that the universe may produce massive seeds or facilitate rapid accretion more efficiently than standard hierarchical models predict.

Taking a complementary approach, Casey-Clyde et al. [85] developed an inverse model anchored to the quasar luminosity function (QLF): rather than predicting  $h_c$ , they take the observed GWB amplitude as input and infer the underlying SMBHB population—including the local number density, mass distribution, and the fraction of quasars associated with merging binaries. This is a concrete realization of the program outlined in eq. (30): measuring  $h_c$  constrains the physics in the double integral, and the QLF model exploits this by using the GWB measurement to extract the merger rate density  $\dot{\phi}_{\text{BHB}}$  via the observed quasar population rather than galaxy-merger assumptions (see fig. 7 for a schematic comparison and fig. 5 for the resulting merger rate densities).

Meanwhile, large-volume simulations like ASTRID [86] now capture the rare, ultra-massive  $z \sim 0.3$  binaries missed by smaller boxes. However, their fiducial GWB predictions remain below the measured amplitude (e.g.  $A_{\text{yr}} \approx 7 \times 10^{-16}$  for ASTRID), which may reflect AGN feedback prescriptions, or other modeling choices [87]. More broadly, Lapi et al. [88] use a semi-empirical framework to highlight a persistent tension between local SMBH demographics and the GWB amplitude, suggesting that reconciling the two may require revisions to the assumed mass function, accretion history, or both.

*The Astrophysical GWB Ceiling.* – A useful sanity check on any forward model for the GWB is that no astrophysical population can radiate more GW energy than the rest mass it is able to process through relativistic inspirals. This observation can be turned into a population-agnostic upper bound on the characteristic strain amplitude, which we refer to as an energetic ceiling, see Mingarelli (2026) [89]. The ceiling is not a substitute for population synthesis, but it provides a conservative guardrail: any model that violates it is unphysical, independent of microphysics.

We start from the relation between the GW energy density and the characteristic strain (cf. eq. (29)). Integrating over the PTA band,

$$(31) \quad \rho_{\text{gw}} = \rho_c \int_0^{f_{\text{max}}} \Omega_{\text{gw}}(f) \frac{df}{f} = \frac{2\pi^2 \rho_c}{3H_0^2} \int_0^{f_{\text{max}}} f h_c^2(f) df,$$

where  $\rho_c$  is the critical density and  $H_0$  is the Hubble constant. Substituting the inspiral power law  $h_c(f) = A(f/f_{\text{ref}})^{-2/3}$  from sect. 2 yields

$$(32) \quad \rho_{\text{gw}} = \frac{\pi^2 \rho_c}{H_0^2} A^2 f_{\text{ref}}^{4/3} f_{\text{max}}^{2/3}.$$

The astrophysical input is that the total GW energy radiated by the population cannot exceed a fraction  $\epsilon_{\text{gw}}$  of the rest-mass density  $\rho_{\text{src}}$  that is processed through GW-efficient inspirals:

$$(33) \quad \rho_{\text{gw}} \leq \epsilon_{\text{gw}} \rho_{\text{src}}.$$

Here  $\rho_{\text{src}} = f_{\text{merge}} \rho_{\bullet}$ , where  $f_{\text{merge}}$  is the fraction of the SMBH mass density that is processed through mergers and  $\rho_{\bullet}$  is the local SMBH mass density. Equating eq. (32) and eq. (33) and solving for  $A$  gives a conservative upper bound,

$$(34) \quad A \leq \frac{H_0}{\pi} f_{\text{ref}}^{-2/3} f_{\text{max}}^{-1/3} \left( \frac{\epsilon_{\text{gw}} \rho_{\text{src}}}{\rho_c} \right)^{1/2}.$$

The physical meaning is simple: at fixed processed mass budget, the spectral amplitude is larger when the signal terminates at lower  $f_{\text{max}}$ , i.e. when the population is dominated by higher-mass binaries.

The key observational input is the local SMBH mass density. Liepold & Ma [35] revised this quantity upward using the volume-limited MASSIVE survey [90], which provides a more complete census of the most massive early-type galaxies ( $M_* \gtrsim 10^{11.5} M_{\odot}$ ) than earlier photometric surveys. Convolving their GSMF with the  $M_{\bullet}-M_*$  scaling relation of McConnell & Ma [91], they derive

$$(35) \quad \rho_{\bullet} = (1.8_{-0.5}^{+0.8}) \times 10^6 M_{\odot} \text{Mpc}^{-3},$$

notably higher than earlier estimates from shallower surveys or the Soltan argument, which typically yield  $\rho_{\bullet} \sim (3-6) \times 10^5 M_{\odot} \text{Mpc}^{-3}$  [92–95].

For the PTA band, the GWB is composed of the inspiral phase of the cosmic SMBHB population. For binaries with spin  $a = 0.7$  [96], the inspiral-phase radiative efficiency is  $\epsilon_{\text{gw}} \approx 0.02$ , with the remaining energy radiated during merger and ringdown above the

ISCO frequency [97, 98]. For ultra-massive systems with  $\mathcal{M}_{\text{c,eff}} \approx 10^{10} M_{\odot}$ , the observed ISCO frequency is  $f_{\text{max}} \approx 400$  nHz. Adopting a maximal merger fraction  $f_{\text{merge}} \sim 0.1$  [94] and the Liepold & Ma [35] mass density, eq. (34) yields a benchmark ceiling in the PTA band [89]:

$$(36) \quad A_{\text{PTA}} \leq 1.6_{-0.3}^{+0.3} \times 10^{-15} \left( \frac{\epsilon_{\text{gw}}}{0.02} \right)^{1/2} \left( \frac{\rho_{\text{src}}}{1.8 \times 10^5 M_{\odot} \text{Mpc}^{-3}} \right)^{1/2} \left( \frac{f_{\text{max}}}{400 \text{ nHz}} \right)^{-1/3} \left( \frac{f_{\text{ref}}}{1 \text{ yr}^{-1}} \right)^{-2/3},$$

where the uncertainties are propagated from the Liepold & Ma mass density. This ceiling is within  $1\sigma$  of the NANOGrav, EPTA, and PPTA measurements (see fig. 5). The fact that current PTA results cluster near this scale, rather than orders of magnitude below it, implies that PTAs are probing the high-efficiency end of the allowed astrophysical parameter space.

The agreement between the ceiling and observed amplitudes also has implications for the broader SMBH population. The Liepold & Ma density is notably higher than estimates from QLFs via the Soltan argument. As noted by Sato-Polito et al. [83], boosting the mass function at the ultra-massive end ( $\log_{10} M_{\bullet}/M_{\odot} \gtrsim 10$ ) would predict Poisson fluctuations in the free spectrum that are not yet evident in the NANOGrav data, suggesting that the resolution of the amplitude question may involve a combination of a modestly richer mass function and refined noise modeling rather than a single dramatic correction at the highest masses.

#### 4. – Modeling the GWB

The amplitude and spectral shape of the GWB contain a wealth of information about the history of galaxy formation and black hole growth. As derived in sect. 2, the characteristic strain spectrum (eq. (30)) is set by the SMBHB merger rate density and chirp mass distribution, and connects directly to the cross-power spectral density of the timing residuals (eq. (18)). To decode this information, we rely on population synthesis models that link the observable properties of galaxies (such as stellar mass and merger rate) to the invisible population of GW-emitting binaries.

Broadly, these models fall into three categories: (1) Major Merger Models, which track the hierarchical assembly of dark matter halos and galaxies; (2) Quasar-based Models, which use the population of AGN as tracers for merger activity; and (3) Astrophysics-agnostic Models, which parameterize the binary population directly without assuming specific host galaxy relations.

Before describing the statistical models, it is useful to outline the physical journey of a SMBHB (see fig. 6). The process begins when two galaxies, each hosting a central SMBH, become gravitationally bound. The SMBHs sink toward the center of the merger remnant via dynamical friction against the background of stars and dark matter on kiloparsec scales. Once the black holes form a bound pair, dynamical friction becomes inefficient. The binary must continue to shrink through interactions with its environment before GW emission can drive the system to coalescence. The total orbital decay rate is the sum of three contributions:

$$(37) \quad \left( \frac{da}{dt} \right) = \left( \frac{da}{dt} \right)_{\text{GW}} + \left( \frac{da}{dt} \right)_{\star} + \left( \frac{da}{dt} \right)_{\text{gas}}$$

1. **Stellar Hardening (pc scale):** At parsec scales, binaries harden by scattering

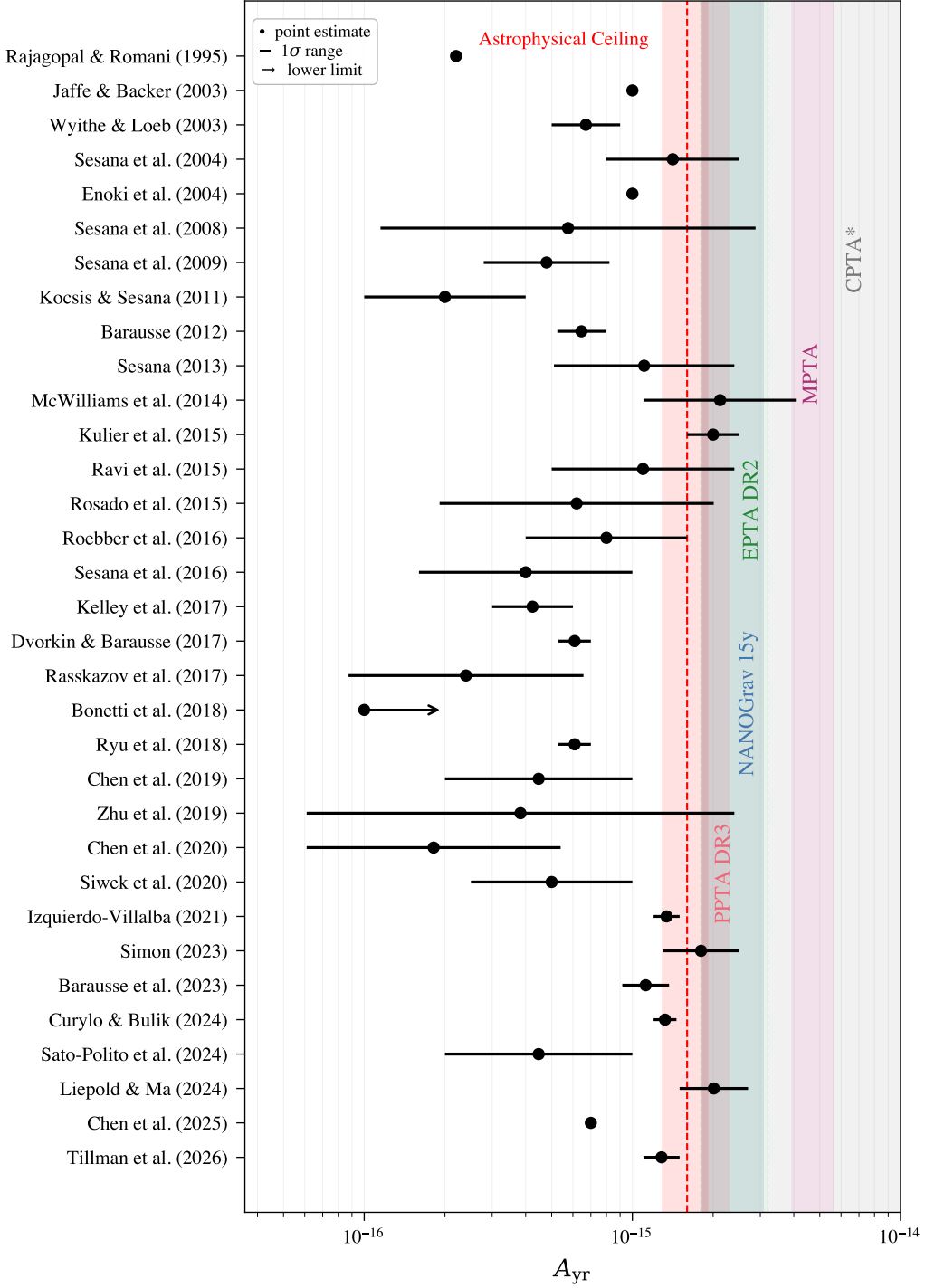


Fig. 5. – Predicted GWB characteristic strain amplitudes at  $f = 1 \text{ yr}^{-1}$  from 33 astrophysical models spanning three decades of work [35, 46, 47, 51, 68–70, 75–78, 82, 83, 87, 99–117]. \*CPTA upper limits span three order of magnitude in amplitude and has been truncated for clarity.

individual stars from the loss cone. The hardening rate is typically parameterized as [120, 121]:

$$(38) \quad \left(\frac{da}{dt}\right)_* = -\frac{\rho H}{\sigma} a^2,$$

where  $\rho$  is the stellar density,  $\sigma$  is the velocity dispersion, and  $H \approx 15 - 20$  is a dimensionless hardening parameter. This mechanism is efficient at low frequencies but fades as the binary shrinks ( $da/dt \propto a^2$ ). If stellar hardening dominates, the residence time of binaries at low frequencies is reduced, causing a turnover or flattening of the GWB spectrum to  $h_c(f) \propto f$  at  $f \lesssim 10$  nHz. The time spent in this phase is encoded in the merger timescale  $\tau_G$ , which is a critical astrophysical uncertainty for all population models.

- Gas-Driven Migration (sub-pc scale):** In gas-rich environments, circumbinary disks can exert torques on the binary. While highly model-dependent, the migration rate is often scaled to the local accretion rate  $\dot{M}$  [47, 122]:

$$(39) \quad \left(\frac{da}{dt}\right)_{\text{gas}} \propto -\frac{\dot{M}}{\mu} a^{1/2},$$

where  $\mu$  is the reduced mass. Gas-driven migration typically results in spectral indices flatter than the GW-only prediction (e.g.,  $h_c(f) \propto f^{-7/6}$  or similar), depending on the specific disk viscosity and cavity interaction models [47].

- Gravitational Wave Emission (milliparsec scale):** At small separations, GW emission becomes the dominant energy loss mechanism. For a circular binary of mass ratio  $q = M_2/M_1$  and total mass  $M_{\text{tot}}$ , the decay rate is given by Peters (1964) [123]:

$$(40) \quad \left(\frac{da}{dt}\right)_{\text{GW}} = -\frac{64}{5} \frac{M_1 M_2 M_{\text{tot}}}{a^3}.$$

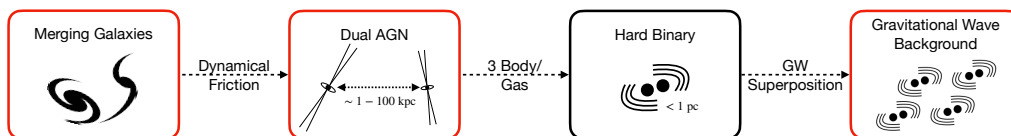


Fig. 6. – **The SMBHB Lifecycle.** (Left) Following a galaxy merger, dynamical friction from the stellar and dark matter background drives the two SMBHs toward the center of the remnant, from  $\sim$  kpc separations down to  $\sim$  pc scales on timescales of  $\sim 100$  Myr–Gyr. The galaxy merger rate that initiates this process is described by eq. (41). (Center) At kiloparsec-to-parsec scales, if both black holes are accreting, the system may be observable as a dual AGN [118, 119]. Further hardening requires three-body stellar scattering or circumbinary gas drag to overcome the “final parsec problem.” The physics governing these stages is captured by eq. (37). (Right) Once the binary reaches milliparsec separations, GW emission becomes efficient, driving the system to coalescence. These binaries are potential CW sources (sect. 6). The incoherent superposition of signals from this final phase constitutes the nanoHertz GWB (sect. 2).

Since the frequency scales as  $f \propto a^{-3/2}$ , this leads to the rapid evolution  $\dot{f} \propto f^{11/3}$  and the standard characteristic strain spectrum  $h_c(f) \propto f^{-2/3}$ .

PTAs probe the final, GW-dominated inspiral phase. However, the environmental hardening mechanisms above shape the population of binaries that reach the PTA band, and their imprint on the GWB spectrum is observable. Recent PTA analyses search for these signatures by fitting for a broken power law or allowing the spectral index  $\gamma$  to deviate from 13/3 at low frequencies [41]. The population models below must account for the time elapsed during these earlier hardening phases to correctly predict the merger rate at redshift  $z$ .

**4.1. Major Merger Models.** – The most direct approach models the SMBHB population semi-analytically by deriving the SMBHB merger rate from the galaxy merger rate, which is in turn derived from the observed galaxy pairing rate [39, 108, 110, 124].

The galaxy differential pairing rate per unit proper time,  $t$ , logarithmic galaxy stellar mass,  $\log_{10} M_*$ , and galaxy mass ratio,  $q_G$ , is modeled as:

$$(41) \quad \dot{\phi}_{G,\text{pair}} = \frac{d^3 \Phi_{G,\text{pair}}}{dt d \log_{10} M_* dq_G} = \phi_*(M_*, z) \frac{\mathcal{F}(M_*, z, q_G)}{\tau_G(M_*, z, q_G)},$$

where  $\phi_*(M_*, z)$  is the galaxy stellar mass function (GSMF) describing the density of galaxies at a given mass and redshift, and  $\mathcal{F}$  is the pair fraction. The critical astrophysical uncertainty lies in  $\tau_G$ , the galaxy merger timescale. This is the proper time elapsed between the pairing of two galaxies at  $z_{\text{pair}}$  and their merger at  $z_{\text{merge}}$ .

To translate galaxy mergers into black hole mergers, standard models rely on empirical scaling relations, typically chaining  $M_* \rightarrow M_{\text{bulge}} \rightarrow M_{\text{BH}}$ . In the standard GSMF framework, we scale from bulge mass to black hole mass using:

$$(42) \quad \log_{10} M_{\text{BH}} = \alpha + \beta \log_{10} \left( \frac{M_{\text{bulge}}}{10^{11} M_{\odot}} \right) \pm \Delta,$$

where  $\Delta$  represents the intrinsic scatter. This scatter is physically important; it allows for the possibility that a moderate-mass galaxy hosts an unexpectedly massive black hole. Given the steep mass scaling of the GW signal ( $h \propto \mathcal{M}^{5/3}$ ), even a small number of “over-massive” black holes scattered upward by  $\Delta$  can dominate the background signal. We compute the final SMBHB merger rate,  $\dot{\phi}_{\text{BHB}}$ , by convolving the galaxy merger rate with the probability distribution of BH masses  $P(\log_{10} M_{\text{BH}} | \log_{10} M_{\text{bulge}})$ .

However, recent work has highlighted that the velocity dispersion ( $\sigma$ ) of the host galaxy may be a more fundamental predictor of black hole mass than stellar mass. Simon [82] first explored the VDF as an alternative proxy for the SMBH mass function, comparing predictions from the GSMF, an inferred VDF (derived from the GSMF via the Faber–Jackson relation), and a spectroscopic VDF measured directly from galaxy surveys. The VDF-based approaches predict a higher abundance of massive black holes and correspondingly larger GWB amplitudes than the standard GSMF chain, while also exhibiting less dependence on the assumed intrinsic scatter in the  $M_{\text{BH}}$ –host relation.

Building on this, Sato-Polito et al. (2024) demonstrate that modeling the population based on the VDF rather than the GSMF significantly alters the predicted GWB. The  $M_{\text{BH}} - \sigma$  relation is tighter (has lower intrinsic scatter) than  $M_{\text{BH}} - M_*$ , so VDF-based models avoid the “up-scattering” of low-mass galaxies into the high-mass regime that

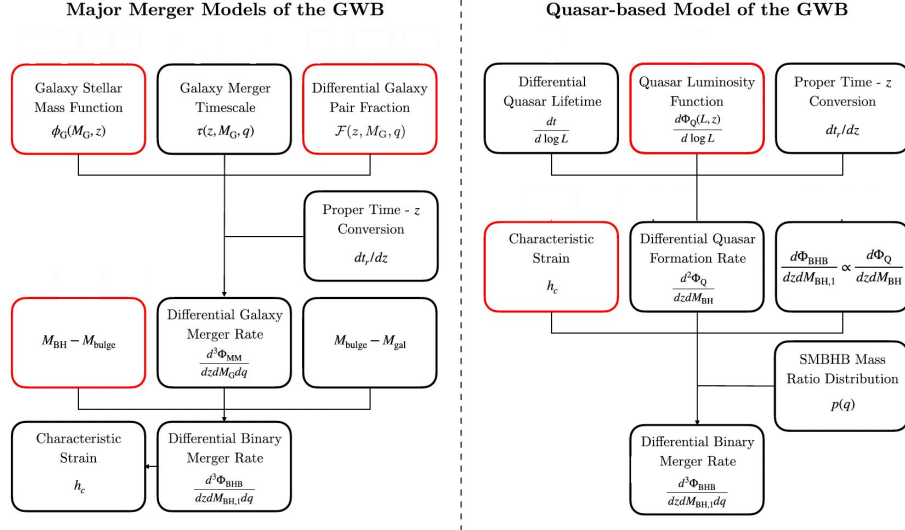


Fig. 7. – Comparison of model frameworks. Major merger models (left) are forward models: they start from galaxy stellar mass functions and pair fractions to predict the GWB amplitude. Quasar-based models (right) are better suited to population inference: they take the observed GWB amplitude as input and use the QLF to constrain the underlying SMBHB population. Red boxes indicate observational inputs; black boxes indicate theoretical components. The two approaches are complementary—forward models predict the signal, while QLF-based inference extracts the population physics from the measurement (eq. (30)). Figure adapted from [85].

often plagues GSMF-based estimates. Interestingly, despite the lower scatter, the VDF implies a higher abundance of massive black holes at the high-mass end ( $M_{\text{BH}} \gtrsim 10^9 M_{\odot}$ ) compared to standard GSMF convolutions. Consequently, these models naturally predict a higher GWB amplitude that is consistent with recent PTA measurements, potentially resolving the tension without invoking exotic binary evolution physics [83].

**4.2. Quasar-based SMBHB Models.** – An alternative approach exploits the connection between SMBHBs and AGN. Galaxy major mergers are believed to trigger quasar activity by funneling gas to the central black holes [125–127].

Quasar-based models [85, 118] use the observed quasar population as a proxy for the SMBHB population. This has the advantage of relying on the QLF, which is well-measured out to high redshifts [128, 129]. In these models, the binary merger rate density is proportional to the QLF or a derived triggering rate:

$$(43) \quad \dot{\phi}_{\text{BHB}}(\mathcal{M}, z) \frac{dt_{\text{r}}}{dz} = \phi_0 p_{\mathcal{M}}(\mathcal{M}) \hat{\phi}_{\text{QSO}}(z)$$

where  $\phi_0$  is a normalization constant calibrated to the local universe ( $z = 0$ ),  $p_{\mathcal{M}}$  is the chirp mass probability distribution, and  $\hat{\phi}_{\text{QSO}}(z)$  describes the redshift evolution of the quasar density. Alternatively, one can link the merger rate directly to the quasar

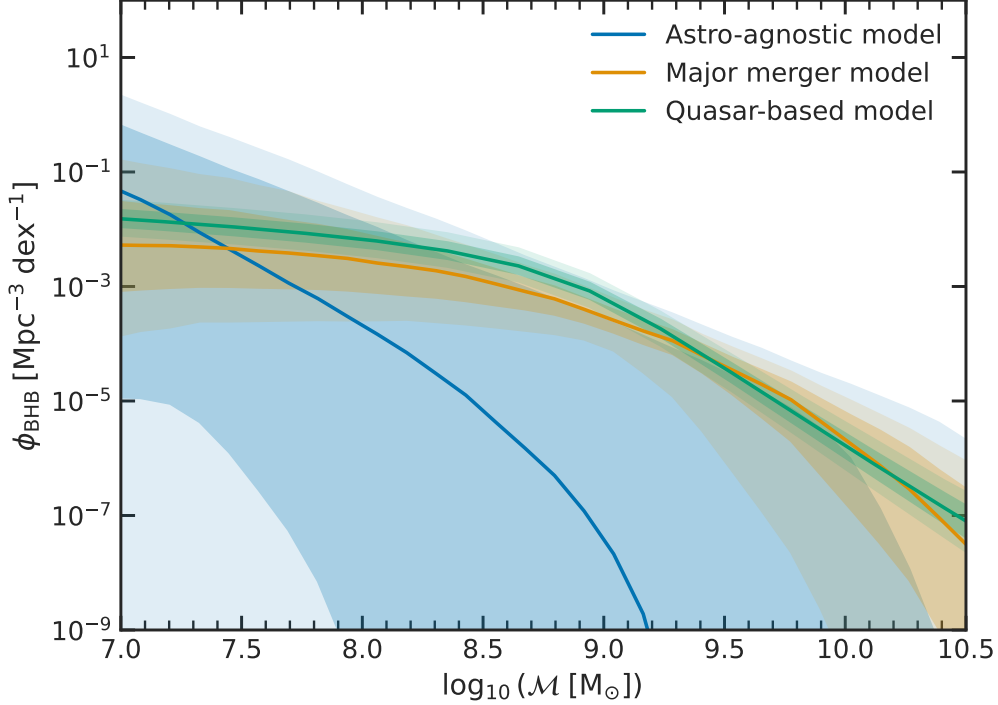


Fig. 8. – Comparison of three SMBHB merger rate models which all produce a GWB amplitude consistent with NANOGrav 15-yr results ( $A_{\text{GWB}} \approx 2.4 \times 10^{-15}$ ). Despite their different assumptions astro-agnostic (blue), major-merger (yellow), and quasar-based (green) all three can reproduce the observed signal, illustrating the current degeneracy in astrophysical interpretation.

triggering rate  $\dot{\phi}_{\text{QSO}}$ :

$$(44) \quad \hat{\phi}_{\text{QSO}}(M_{\text{BH}}, z) = \frac{\dot{\phi}_{\text{QSO}}(M_{\text{BH}}, z) \frac{dt_x}{dz}}{\int \dot{\phi}_{\text{QSO}}(M_{\text{BH}}, z=0) \frac{dt_x}{dz} \Big|_{z=0} d \log_{10} M_{\text{BH}}}$$

By anchoring the merger rate to the visible population of accreting black holes, these models provide an independent check on the major-merger scenarios derived from stellar mass functions (see fig. 7 for a schematic comparison).

The dependence of the predicted GWB on the underlying population parameters is illustrated in fig. 9. The amplitude is most sensitive to the local SMBHB number density  $\Phi_{\text{BHB},0}$  and the minimum primary black hole mass  $M_{\text{BH},1,\text{min}}$ , with a weaker dependence on  $z_{\text{max}}$ . Reproducing the NANOGrav 15-yr amplitude requires either a high number density of binaries or a population dominated by massive systems. Dual AGN fractions can independently constrain  $\Phi_{\text{BHB},0}$  [118, 119], while CW detections of individual binaries probe the high-mass end of the population. Kis-Tóth et al. [130] further test this quasar–merger connection by computing the GWB from merger-triggered quasars using the observed QLF as a constraint on the SMBHB population, finding that the predicted signal is consistent with the NANOGrav amplitude for plausible merger

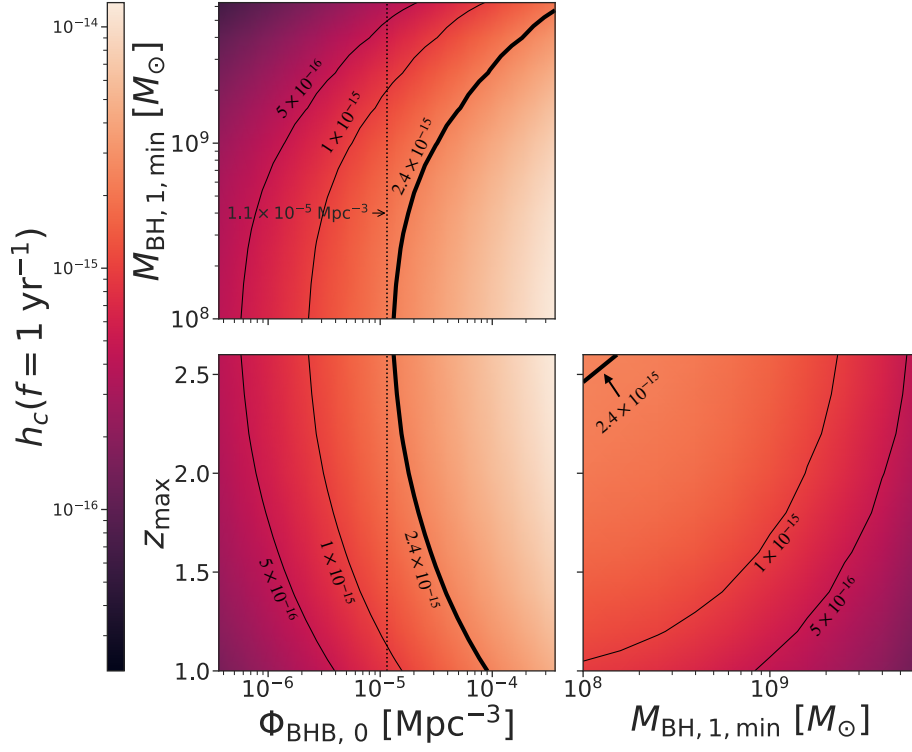


Fig. 9. – GWB characteristic strain amplitude  $h_c(f = 1 \text{ yr}^{-1})$  as a function of three parameters of the quasar-based SMBHB population model: the local binary number density  $\Phi_{\text{BHB},0}$ , the minimum primary black hole mass  $M_{\text{BH},1,\text{min}}$ , and the maximum contributing redshift  $z_{\text{max}}$ . Contours are labeled by the corresponding strain amplitude. The thick contour marks  $h_c = 2.4 \times 10^{-15}$ , corresponding to the NANOGrav 15-yr GWB measurement. The dotted vertical line indicates the local SMBHB number density of  $1.1 \times 10^{-5} \text{ Mpc}^{-3}$ . Figure adapted from [85], updated to the NANOGrav 15-yr amplitude.

parameters.

**4.3. Astrophysics-agnostic Models.** – Finally, we can adopt an “astrophysics-agnostic” approach. Rather than assuming specific scaling relations or galaxy pairing fractions, these models parameterize the merger rate  $\dot{\phi}_{\text{BHB}}$  directly using a flexible functional form, such as a modified Schechter function [131]:

$$(45) \quad \dot{\phi}_{\text{BHB}} = \dot{\phi}_{\text{BHB},0} \left( \frac{\mathcal{M}}{10^7 \text{ M}_\odot} \right)^{-\alpha_{\mathcal{M}}} e^{-\mathcal{M}/\mathcal{M}_*} (1+z)^{\beta_z} e^{-z/z_*}.$$

This method is useful for placing robust upper limits on the merger rate without being tied to the uncertainties of galaxy evolution physics. However, because the GWB spectrum integrates over the entire population, current PTA data primarily constrain the normalization  $\dot{\phi}_{\text{BHB},0}$ , while leaving the shape parameters ( $\alpha_{\mathcal{M}}, \beta_z$ , etc.) largely unconstrained [124]. Despite their different assumptions, all three model classes can reproduce

the observed GWB amplitude, illustrating the current degeneracy in astrophysical interpretation (fig. 8).

## 5. – Gravitational Wave Background Anisotropy

While the initial measurement of the GWB relies on the characteristic Hellings-Downs correlation curve, this curve represents the response to an *isotropic* background. However, the physical GWB is formed by the superposition of discrete sources distributed throughout the Universe, and perfect isotropy is an approximation that must eventually break down. Mapping the angular distribution of GW power across the sky is therefore a major focus of PTA science.

The search for anisotropy is both important and interesting because it serves as a powerful discriminator of the GWB’s origin. A background generated by cosmological processes, such as inflation or phase transitions, is expected to be isotropic to a very high degree. In contrast, an astrophysical background arising from the cosmic population of SMBHBs must inherit the spatial structure of the Universe. This angular structure depends strongly on frequency, creating distinct physical regimes for anisotropy searches.

The search for spatial anisotropy is also deeply intertwined with tests of GR. While the standard analysis assumes the quadrupolar Hellings-Downs correlation characteristic of tensor (spin-2) waves, alternative theories of gravity predict the existence of scalar (spin-0) and vector (spin-1) polarization modes. These non-Einsteinian modes generate distinct angular correlation patterns—typically monopolar or dipolar—which modify the effective ORF.

From a data analysis perspective, this creates a problem: a deviation from the standard Hellings-Downs curve could arise either from a breakdown of isotropy (e.g., a clustered astrophysical background) or from a breakdown of GR (e.g., a scalar background component). Disentangling these effects requires a generalized map-making approach that simultaneously reconstructs the angular power spectrum for all possible polarization modes. We discuss the physical nature of these alternative polarizations and current observational limits in detail in sect. 8.

In the following, we review the mathematical frameworks developed to detect and characterize angular structure in the GWB (sect. 5.1), then derive the scaling laws that govern intrinsic shot-noise anisotropy and the transition between the low-frequency clustering regime and the high-frequency shot-noise regime (sect. 5.2). We examine the limiting case of a single dominant source and its distinct angular signature (sect. 5.2.1), and conclude with cross-correlations between PTA sky maps and galaxy catalogs as a probe of the LSS traced by the GWB (sect. 5.4).

*A note on notation.*—Throughout this section,  $\gamma_{pq}(\hat{\Omega})$  denotes the directional geometric kernel that encodes the antenna-pattern response of a pulsar pair  $(p, q)$  to GW power arriving from direction  $\hat{\Omega}$ . This should not be confused with the scalar spectral index  $\gamma$  (e.g.,  $\gamma = 13/3$  for the power spectral density of circular SMBHB-driven residuals) used elsewhere in this review.

**5.1. Search Methods for Anisotropy.** – Several complementary techniques have been developed to detect and characterize GWB anisotropy, including spherical harmonic decompositions, pixel-based mapping, square-root spherical harmonics, and Fisher matrix approaches. These frameworks have been extended to incorporate astrometric deflections [132] and circular polarization of the anisotropic background [133]. We summarize the main approaches below.

**5.1.1. Spherical Harmonics.** Mingarelli et al. (2013) [56] introduced the spherical harmonic decomposition of GW power for PTAs, deriving generalized ORFs for arbitrary angular distributions. Taylor and Gair (2013) [72] applied this framework to simulated data, and Taylor et al. (2015) [134] performed the first search using real data from EPTA DR1; see sect. 5.6.

As derived in sect. 2.3, the cross-correlation power spectrum (eq. (15)) depends on the angular power distribution  $P(\hat{\Omega})$ . In the isotropic limit  $P(\hat{\Omega}) = 1$ , this reduces to the Hellings-Downs curve. For anisotropic searches, we define the geometric kernel  $\gamma_{pq}(\hat{\Omega})$  (adopting the  $(p, q)$  convention standard in the anisotropy literature [56, 72]):

$$(46) \quad \gamma_{pq}(\hat{\Omega}) = 2 \frac{(\hat{p} \cdot \hat{q} - (\hat{p} \cdot \hat{\Omega})(\hat{q} \cdot \hat{\Omega}))^2}{(1 + \hat{p} \cdot \hat{\Omega})(1 + \hat{q} \cdot \hat{\Omega})} - (1 - \hat{p} \cdot \hat{\Omega})(1 - \hat{q} \cdot \hat{\Omega}),$$

such that the observed cross-power is simply the sky-integral of the intensity map weighted by this kernel:

$$(47) \quad \mathcal{R}_{pq}^{\text{GW}}(f) = \frac{1}{(4\pi f)^2} H(f) \int_{S^2} d\hat{\Omega} P(\hat{\Omega}) \gamma_{pq}(\hat{\Omega}).$$

Map reconstruction methods essentially invert this integral equation. However, the number of statistically independent angular modes one can constrain is strictly bounded by the number of pulsar pairs,  $N_{\text{pair}} = N_{\text{psr}}(N_{\text{psr}} - 1)/2$ . Pixel-based approaches (e.g., using HEALPix) often face ill-conditioned covariance matrices scaling as  $\mathcal{O}(N^2)$ , making basis decomposition methods preferred for current data. A further limitation is that spherical harmonics form an orthogonal basis on the full sky, implicitly assuming a uniform distribution of pulsars. In practice, regional PTAs have pulsars concentrated in their own hemisphere, so the spherical harmonics modes are no longer orthogonal over the sampled sky, leading to mode coupling and leakage of power between multipoles. This motivates the Fisher-matrix and pixel-based approaches discussed below, which naturally account for non-uniform sky coverage.

**5.1.2. Square-Root Spherical Harmonics.** The spherical harmonic basis provides a natural framework for decomposing  $P(\hat{\Omega})$ . However, a direct decomposition can yield unphysical negative power values. To ensure positive-definiteness ( $P(\hat{\Omega}) \geq 0$ ) by construction, it is advantageous to decompose the *square root* of the power [135, 136]:

$$(48) \quad P(\hat{\Omega})^{1/2} = \sum_{L=0}^{\infty} \sum_{M=-L}^L a_{LM} Y_{LM}(\hat{\Omega}).$$

Squaring this expansion to obtain  $P(\hat{\Omega})$  introduces non-linear coupling between the  $a_{LM}$  coefficients, but the parameterization guarantees  $P(\hat{\Omega}) \geq 0$  by construction, providing a robust physical prior for Bayesian searches. However, the underlying basis functions are still spherical harmonics, so the square-root decomposition inherits the same sensitivity to anisotropic pulsar distributions: mode coupling from incomplete sky coverage affects the  $a_{LM}$  coefficients just as it does the standard  $c_{\ell m}$ . This basis was adopted for the NANOGrav 15-yr anisotropy search [137]; see sect. 5.6.

**5.1.3. Pixel-based Methods.** An alternative to the spherical harmonic decomposition is to map the GW power directly in a pixel basis [138]. The angular distribution of power,  $P(\hat{\Omega})$ , is modeled as piecewise constant across  $N_{\text{pix}}$  disjoint sky regions:

$$(49) \quad P(\hat{\Omega}) = \sum_{i=1}^{N_{\text{pix}}} P_i,$$

where  $P_i$  is the power in the  $i$ -th pixel and the sum runs over disjoint sky regions defined by the HEALPix pixelization. The cross-power spectral density (eq. (47)) then becomes a sum over pixels, weighted by the integral of the geometric kernel  $\gamma_{pq}(\hat{\Omega})$  over each pixel area.

The primary advantage of pixel-based methods is their flexibility; they are agnostic to the global shape of the background and are particularly effective at identifying localized “hotspots” or anisotropic features that would require high- $\ell$  modes to resolve in a spherical harmonic basis. Furthermore, unlike standard spherical harmonic expansions, which can produce unphysical negative power due to truncation, the pixel basis naturally has  $P_i \geq 0$ . While technically bounded by the number of unique baselines, the number of independent pixels one can robustly constrain is in practice limited by the intrinsically broad antenna pattern of the PTA: the geometric kernel  $\gamma_{pq}(\hat{\Omega})$  varies slowly across the sky, making adjacent pixels highly degenerate and limiting the number of independent pixels the array can resolve. This is also referred to as the pixels being correlated. For current PTAs, this limits robust reconstructions to low spatial resolutions (e.g.,  $N_{\text{pix}} \lesssim 48$  for the EPTA; see [139]), although this will scale dramatically with the advent of next-generation facilities like the DSA-2000 [140] and the SKAO [141].

Full pixel-based reconstruction inverts the complete pixel-pixel response matrix via Bayesian inference or maximum-likelihood methods, jointly fitting all pixels and thereby deconvolving the array’s beam pattern to produce a “clean map.” The PTA baseline configuration has blind spots, so the response matrix is typically ill-conditioned, requiring regularization (e.g., SVD truncation) to suppress noise amplification in insensitive modes. Grunthal et al. [142] show that accounting for spatially variable resolution in this regularization can improve the significance of localized features by up to a factor of two.

**5.1.4. The Radiometer.** The *radiometer*, originally developed for ground-based GW detectors by Ballmer [143] and Mitra et al. [144] and now widely adopted in PTA analyses (see [145] for a systematic comparison of PTA search bases), takes the opposite limit to full pixel reconstruction: it inverts only the diagonal of the response matrix, estimating each pixel independently. For a target direction  $\hat{\Omega}_0$ , the radiometer estimator is

$$(50) \quad \hat{P}(\hat{\Omega}_0) = \frac{\sum_{p<q} w_{pq} \gamma_{pq}(\hat{\Omega}_0) \hat{\rho}_{pq}}{\sum_{p<q} w_{pq} \gamma_{pq}^2(\hat{\Omega}_0)},$$

where  $\hat{\rho}_{pq}$  is the measured cross-correlation for pair  $(p, q)$  and  $w_{pq}$  are inverse-variance weights. Scanning  $\hat{\Omega}_0$  across the sky produces a “dirty map” of GW power, analogous to the dirty image in radio interferometry. By ignoring inter-pixel correlations, the radiometer is computationally inexpensive and numerically stable even for arrays with sparse coverage, making it well suited for rapid identification of localized hotspots. The trade-off is that the broad antenna patterns of the pulsar pairs smear localized sources

across the sky—frequently producing antipodal sidelobes on the opposite side of the sky, a characteristic artefact of the PTA beam pattern—and the single-direction estimates are correlated through shared pulsars. This approach has been used in recent anisotropy searches by the MPTA [146] and PPTA [147]; see sect. 5.6.

**5.1.5. Fisher Matrix Formalism.** Ali-Haïmoud, Smith & Mingarelli [59, 139] developed a Fisher matrix formalism for anisotropic GWB searches that addresses the limitations of the spherical harmonic and pixel bases described above. In the weak-signal limit, the Fisher information matrix for the band-integrated GWB intensity map is:

$$(51) \quad \mathbf{F}_f(\hat{\Omega}, \hat{\Omega}') = \frac{1}{(4\pi f)^4} \sum_{p \neq q} \mathcal{T}_p(f) \mathcal{T}_q(f) \frac{2T_{pq} \Delta f}{\sigma_{p,f}^2 \sigma_{q,f}^2} \gamma_{pq}(\hat{\Omega}) \gamma_{pq}(\hat{\Omega}'),$$

where  $\mathcal{T}_p(f)$  is the transmission function encoding information loss from the timing model fit,  $T_{pq}$  is the effective observation time for pair  $(p, q)$ , and  $\sigma_{p,f}$  is the noise power spectrum of pulsar  $p$ . Unlike the spherical harmonic basis, which assumes uniform sky coverage,  $\mathbf{F}$  is constructed directly from the discrete pulsar positions and noise properties, so it naturally accounts for the anisotropic distribution of pulsars in any real PTA.

The eigenvectors of  $\mathbf{F}$  (eigenmaps) form an orthogonal, PTA-specific basis for the observable sky. At most  $N_{\text{pair}}$  eigenmaps have non-zero eigenvalues, setting a hard limit on the number of independent angular modes the array can constrain. Reconstructing the GWB in this basis rather than in spherical harmonics avoids the small-scale leakage problem (sect. 5.5): spatial modes to which the array is insensitive are automatically filtered out, preventing unmodeled high- $\ell$  power from aliasing into the measured low- $\ell$  coefficients.

A key result of this formalism is that the principal maps are, in general, statistically correlated with the GWB monopole [139]. For any finite, anisotropically distributed set of pulsars, searching for anisotropy simultaneously with the monopole degrades the sensitivity to both. This arises because the pairwise timing response functions  $\gamma_{pq}(\hat{\Omega})$  are not orthogonal to an isotropic background, so the monopole amplitude is coupled to all angular modes. The severity of this coupling depends on the specific pulsar configuration: Ali-Haïmoud et al. [139] showed that for the EPTA, the minimum detectable monopole amplitude increases by up to  $\sim 30\%$  when simultaneously fitting for a hotspot, depending on its sky location.

A further insight concerns the pulsar autocorrelations, i.e. the common uncorrelated red noise (CURN) model. The single-pulsar timing response  $\gamma_{\hat{p}\hat{p}}(\hat{\Omega})$  is sensitive not only to the GWB monopole but also to a dipole projected along  $\hat{p}$  and a quadrupole projected twice onto  $\hat{p}$  (eq. 38 of [139]). Each pulsar therefore picks up a different combination of these low-order multipoles in its red noise spectrum. When using autocorrelations to set upper limits on the GWB amplitude, one must account for these anisotropic contributions; neglecting them biases the inferred monopole [139].

**5.1.6. Timing-Residual Maps and BiPOSH.** The methods above reconstruct the angular power distribution  $P(\hat{\Omega})$  that enters the cross-power spectral density (eq. (47)). A complementary approach asks a more fundamental question: is the GWB *statistically* isotropic? Rather than fitting a map, one tests whether the covariance structure of the timing residuals is consistent with isotropy.

In the limit of a large, dense array, the timing residuals can be treated as a scalar field  $z(\hat{\Omega})$  on the celestial sphere [60], which is the convolution of the true GW sky with

the PTA response function. Decomposing this field into spherical harmonics,

$$(52) \quad z(\hat{\Omega}) = \sum_{\ell=2}^{\infty} \sum_{m=-\ell}^{\ell} z_{\ell m} Y_{\ell m}(\hat{\Omega}),$$

an isotropic background produces a diagonal covariance:  $\langle z_{\ell m} z_{\ell' m'}^* \rangle = C_{\ell}^z \delta_{\ell\ell'} \delta_{mm'}$ . Anisotropy breaks this diagonality by coupling different  $(\ell, m)$  modes, just as gravitational lensing couples CMB multipoles. The Bipolar Spherical Harmonic (BiPOSH) formalism [148] captures these off-diagonal correlations:

$$(53) \quad \langle z_{\ell m} z_{\ell' m'}^* \rangle = C_{\ell}^z \delta_{\ell\ell'} \delta_{mm'} + \sum_{L=1}^{\infty} \sum_{M=-L}^L (-1)^{m'} \langle \ell m \ell' - m' | L M \rangle A_{\ell\ell'}^{LM},$$

where  $\langle \ell m \ell' - m' | L M \rangle$  are the Clebsch-Gordan coefficients. The BiPOSH coefficients  $A_{\ell\ell'}^{LM}$  vanish for an isotropic background and encode the angular scale and orientation of any anisotropy:  $L = 1$  captures dipolar structure (e.g., from a nearby dominant source or our motion relative to the GWB rest frame), while  $L = 2$  captures quadrupolar patterns arising from the large-scale distribution of galaxies. At low GW frequencies where millions of sources contribute,  $A_{\ell\ell'}^{LM} \approx 0$  and the background is effectively isotropic; at higher frequencies where the source population thins (sect. 5.2), shot noise from discrete binaries breaks isotropy and drives the off-diagonal terms to grow. Sato-Polito & Kamionkowski [149] have extended this formalism to characterize the expected spectrum of stochastic GW anisotropies in the PTA band.

The BiPOSH coefficients connect directly to the angular power distribution  $P(\hat{\Omega})$  of eq. (47). Parameterizing the anisotropy as

$$(54) \quad P(\hat{\Omega}) = 1 + \sum_{L>0} \sum_{M=-L}^L g_{LM} Y_{LM}(\hat{\Omega}),$$

one can construct a minimum-variance estimator for the physical anisotropy coefficients from the measured BiPOSH spectrum:

$$(55) \quad \widehat{g}_{LM} = \frac{\sum_{\ell\ell'} (\widehat{g}_{LM})_{\ell\ell'} (\Delta g_{LM})_{\ell\ell'}^{-2}}{\sum_{\ell\ell'} (\Delta g_{LM})_{\ell\ell'}^{-2}},$$

where the sum runs over all accessible multipole pairs. This provides a model-independent statistic for testing whether the nanoHertz GW sky exhibits clustering or localized excess power.

**5.2. Scaling Laws and the Shot Noise Regime.** – Having established the methods used to search for anisotropy, we now turn to the signal itself: what level of anisotropy does nature produce? The level of anisotropy can be quantified by the ratio  $\sigma_{\text{gw}}/\mu_{\text{gw}}$ , where  $\mu_{\text{gw}}$  is the expected GW energy density from all sources within a solid angle  $d\Omega$ , and  $\sigma_{\text{gw}}$  is the standard deviation of this energy density due to Poisson fluctuations in the number and distance of contributing sources. This was first calculated in [56] by considering the statistics of sources within a resolution element  $d\Omega$ .

The original derivation (eq. 29 in [56]) approximated the solid angle of a multipole  $\ell$  as  $d\Omega \approx 4\pi/2\ell$ . However, in standard spherical harmonic decompositions, the solid angle of a resolution element scales more steeply as  $d\Omega \approx 4\pi/\ell^2$ . Updating the derivation with this standard geometric mapping modifies the scaling from a square-root to a linear dependence on  $\ell$ . We thus present the updated scaling relation for the anisotropy level:

$$(56) \quad \frac{\sigma_{\text{gw}}}{\mu_{\text{gw}}} \approx 0.2 \left( \frac{f}{10^{-7}\text{Hz}} \right)^{11/6} \left( \frac{5\text{yr}}{T_{\text{obs}}} \right)^{-1/2} \left( \frac{\ell}{2} \right) \alpha^{1/2},$$

where  $f$  is the GW frequency,  $T_{\text{obs}}$  is the total observation time, and  $\alpha$  is a factor of order unity related to the redshift distribution of sources. This result is fully consistent with recent analytical modeling by Sato-Polito & Kamionkowski (2024) [149], who derived the scaling of the relative angular power spectrum in the shot-noise limit. They found the power ratio scales as  $C_\ell/C_0 \propto f^{11/3}$ , which matches the square of our amplitude scaling in eq. (56) (since  $(\sigma/\mu)^2 \propto f^{11/3}$ ). eq. (56) highlights the strong frequency dependence of the signal. The steep power-law distribution of the source population ( $dN/df \propto f^{-11/3}$ ) creates two complementary regimes: the clustering regime (low frequency,  $f \lesssim 10$  nHz), and the shot noise regime (high frequency,  $f \gtrsim 25$  nHz).

In the clustering regime, millions of binaries simultaneously contribute ( $\Delta N \gg 1$ ; eq. (7)), suppressing shot-noise fluctuations. The residual anisotropy is then dominated by the spatial clustering of the source population: SMBHBs reside in massive galaxies that trace the cosmic web, and cross-correlating GWB maps with galaxy surveys can recover this LSS imprint (sect. 5.4).

As frequency increases, the bin occupancy  $\Delta N$  (eq. (7); fig. 2) drops steeply and the characteristic strain spectrum (sect. 2.5) departs from the smooth  $h_c \propto f^{-2/3}$  power law. Roebber et al. [107] showed that Poisson noise begins to dominate the strain spectrum above  $f \gtrsim 20$  nHz, and Agazie et al. [28] confirm this using the NANOGrav 15-yr data, finding that  $h_c(f)$  breaks from the power law at  $f \approx 26$  nHz. Above this frequency, the spectrum is shaped by individual loud sources rather than a smooth ensemble average, and anisotropy from discrete binaries should emerge—bridging the gap between stochastic background searches and CW searches (sect. 6).

The frequency at which this transition occurs depends on the SMBHB mass scale: for  $\mathcal{M} = 10^{10} M_\odot$  binaries and  $T_{\text{obs}} = 20$  yr, eq. (7) gives  $\Delta N \approx 6$  at  $f = 60$  nHz, so only a handful of systems occupy each frequency bin. Recent evidence that SMBHBs may be more massive than previously assumed [35] would push this transition to even lower frequencies.

**5.2.1. Anisotropy from a Single Bright Source.** In the extreme limit of the shot-noise regime, the “background” may be dominated by a single, deterministic CW source. Recent targeted searches in the NANOGrav 15-yr dataset have modeled this limit analytically [42], and we sketch the derivation below.

We can model the characteristic strain squared field,  $h_c^2(\hat{\Omega})$ , as the sum of a uniform isotropic component and a single point source localized at  $\hat{\Omega}_0$ :

$$(57) \quad h_c^2(\hat{\Omega}) = h_{c,\text{iso}}^2 + h_{c,\text{CW}}^2 \delta(\hat{\Omega} - \hat{\Omega}_0).$$

For all multipoles  $\ell > 0$ , the isotropic contribution vanishes, and the power spectrum is

driven entirely by the point source. This produces a “white” angular power spectrum:

$$(58) \quad C_\ell = \frac{(h_{c,CW}^2)^2}{4\pi} \quad \text{for } \ell > 0.$$

However, the “isotropic” background  $h_{c,iso}^2$  is itself a superposition of discrete sources, which introduces a stochastic shot noise floor. As detailed in [150], the total observed power spectrum is:

$$(59) \quad C_\ell^{\text{tot}} = C_\ell^{\text{stoch}} + \frac{(h_{c,CW}^2)^2}{4\pi} + 2\delta_{\ell 0} \bar{I} h_{c,CW}^2.$$

Because a point source projects equally onto all spherical harmonics, a CW produces a flat  $C_\ell$  for  $\ell > 0$  (eq. (58)); power concentrated at a single  $\ell$  would not be consistent with a CW. The stochastic shot noise  $C_\ell^{\text{stoch}}$  from the background population is also approximately flat, so distinguishing the two contributions requires the CW signal to stand above this floor.

As the source population thins at high frequencies ( $\Delta N \rightarrow 1$ ; eq. (7)), the background transitions to the single-source regime where this flat  $C_\ell$  signature becomes the dominant feature. Agarwal et al. [42] exploit this in the first systematic targeted search for CW sources in SMBHB candidates, using the flat  $C_{\ell>0}/C_0$  ratio as part of the CW detection protocol (sect. 6) to assess whether individual binaries are detectable in the angular power spectrum.

**5.3. *GWB Polarization from Anisotropies.*** – The search for anisotropy is incomplete without considering the polarization of the signal. While a purely stochastic, cosmological GWB is expected to be unpolarized, the “popcorn” background produced by individual SMBHBs will exhibit significant local polarization. As noted by Kato and Soda [151], distinguishing between the intensity and polarization modes is critical for disentangling these discrete foregrounds from a parity-odd cosmological background. Sato-Polito and Kamionkowski [133] showed that PTAs can in principle measure the circular polarization (Stokes  $V$ ) of the GWB, providing a direct probe of parity violation in the gravitational sector. Conneely et al. [152] further formalized this by demonstrating that the standard power-spectrum approach is insufficient for anisotropic backgrounds; instead, a full decomposition into Stokes parameters ( $I, Q, U, V$ ) is required to capture the spatial distribution of the sources. Building on this, Jow, Tsai, and Pen [153] recently argued that the GWB sky should formally be treated as a polarized field. The Earth term samples the two tensor polarizations ( $+$  and  $\times$ ) differently depending on the source position, so the effective resolution of the array is maximized only when reconstructing the full polarized map. In this framework, the PTA acts as a full-sky polarimeter, where “hotspots” of circular polarization could serve as unique tracers for individual binaries sitting just below the detection threshold (sect. 6).

**5.4. *Cross-Correlation Analysis.*** – The spatial distribution of the GWB offers a novel window into the LSS of the Universe. As the GWB is generated by the incoherent superposition of signals from SMBHBs, it naturally inherits the clustering properties of their host galaxies. Since these massive galaxies reside in the densest peaks of the cosmic web, the GWB acts as a biased tracer of the underlying dark matter distribution [154–156].

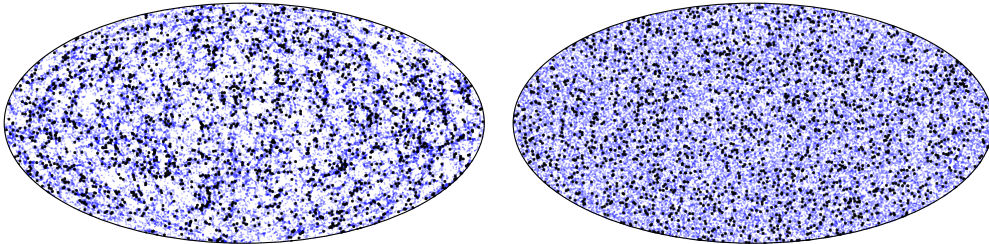


Fig. 10. – **The GWB as a Tracer of LSS.** An illustration of how a GWB map informed by LSS (left) differs from one where source positions are isotropized (right). While only 1-4% of galaxies host active SMBHBs, the resulting GWB anisotropy carries the imprint of the cosmic web. Detecting this structure requires cross-correlation with galaxy catalogs to overcome the shot noise of individual loud sources [85, 157].

This connection enables a powerful probe of cosmic structure: cross-correlating GWB anisotropy maps with electromagnetic galaxy surveys. Recent work by [157] has demonstrated that this technique is essential for extracting astrophysical information from the background. While the auto-correlation of the GWB is often dominated by the “shot noise” of a few loud, nearby sources, the cross-correlation signal is driven by the bulk population of binaries that trace the LSS.

At low frequencies ( $f \lesssim 10$  nHz; fig. 2), millions of binaries contribute to the signal. In this regime, the GWB anisotropy should statistically mirror the galaxy distribution. However, in any single realization of the Universe, the signal can be masked by Poissonian fluctuations from bright binaries. Ref. [157] showed that by effectively filtering out these loud sources (e.g., by imposing a strain cut of  $h_{\text{res}} \sim 10^{-16}$ ), the underlying LSS imprint becomes retrievable.

Importantly, while auto-correlation analyses struggle to distinguish an LSS-imprinted background from a uniform Poissonian distribution, cross-correlations break this degeneracy. Simulations indicate that with next-generation PTA sensitivity, cross-correlations could detect the LSS imprint at  $> 3\sigma$  significance for angular resolutions of  $\ell_{\text{max}} \geq 42$ , providing further evidence for the astrophysical origin of the GWB (fig. 10). Since  $\ell_{\text{max}} \sim N$  (sect. 7.3), reaching  $\ell \gtrsim 42$  will require the large number of suitable millisecond pulsars anticipated by the SKAO [141] and DSA-2000 [140].

**5.5. Challenges in Detecting Anisotropy.** – Despite the promise of anisotropy searches, significant observational and systematic hurdles remain. The anisotropy S/N depends on how uniformly the array samples the sky, since each pulsar-pair baseline couples to the angular modes of  $P(\hat{\Omega})$  through a geometric response that varies across the sky [145, 158]. A further fundamental limitation is cosmic variance: even a statistically isotropic GWB from a finite population will exhibit realization-dependent deviations from Hellings–Downs correlations that can mimic or mask true anisotropy [159]. The most immediate practical limitation is the anisotropic distribution of pulsars. Current arrays like NANOGrav are heavily biased toward the Northern hemisphere and the Galactic plane, creating a window function that distorts the reconstructed sky maps. The IPTA will improve sky coverage, but until it does, analysis methods must account for this non-uniform sampling to avoid introducing spurious dipolar or quadrupolar power.

A fundamental limitation in reconstructing the GWB anisotropy arises from the finite

number of pulsar pairs available to sample the continuous GW sky. While eq. (47) describes the cross-power  $\mathcal{R}_{pq}^{\text{GW}}$  as an integral over the entire celestial sphere, current arrays can only effectively constrain a finite set of angular modes. This mismatch between the infinite degrees of freedom in the physical sky and the finite rank of the array's response leads to a systematic bias known as “small-scale leakage” [160].

We can see how this problem emerges directly from the map-making formalism. By decomposing the angular power distribution  $P(\hat{\Omega})$  into spherical harmonics  $Y_{\ell m}(\hat{\Omega})$ , the integral in eq. (47) transforms into a linear system. For a specific pulsar pair indexed by  $k$  (corresponding to pair  $p, q$ ), the timing residual cross-power is:

$$(60) \quad \mathcal{R}_k = \sum_{\ell=0}^{\infty} \sum_{m=-\ell}^{\ell} a_{\ell m} \Gamma_{k, \ell m},$$

where  $a_{\ell m}$  are the harmonic coefficients of the GWB sky and  $\Gamma_{k, \ell m}$  are the geometric projection factors derived from the ORF:

$$(61) \quad \Gamma_{k, \ell m} \propto \int_{S^2} d\hat{\Omega} Y_{\ell m}(\hat{\Omega}) \gamma_{p_k q_k}(\hat{\Omega}).$$

This allows us to write the entire array's response in compact matrix notation. Let  $\mathbf{R}$  be the vector of measured cross-correlations for all pairs, and  $\mathbf{a}$  be the vector of sky coefficients. The measurement equation is simply  $\mathbf{R} = \Gamma \mathbf{a}$ .

Crucially, the vector  $\mathbf{a}$  contains coefficients up to  $\ell \rightarrow \infty$ . However, we probe a finite amount of pulsar pairs, therefore we have the ability of constraining at most  $N_{\text{pairs}}$  real spherical harmonic coefficients or, equivalently, multipoles up to a maximum reconstructed scale  $\ell_{\text{max}}^{\text{rec}} = \left\lfloor \sqrt{\frac{N_{\text{psr}}(N_{\text{psr}}-1)}{2}} + 4 - 1 \right\rfloor$ . We must therefore split the sky into the accessible Large-Scale (LS) modes and the unmodeled Small-Scale (SS) modes:

$$(62) \quad \mathbf{R} = \Gamma_{\text{LS}} \mathbf{a}_{\text{LS}} + \Gamma_{\text{SS}} \mathbf{a}_{\text{SS}}.$$

Standard analysis pipelines operate under the assumption that the sky is effectively band-limited to  $\ell_{\text{max}}^{\text{rec}}$ , modeling the data as  $\mathbf{R} \approx \Gamma_{\text{LS}} \mathbf{a}_{\text{LS}}$ . Solving this inverse problem (e.g., via generalized least squares) yields an estimator  $\hat{\mathbf{a}}_{\text{LS}}$ :

$$(63) \quad \hat{\mathbf{a}}_{\text{LS}} = (\Gamma_{\text{LS}}^T \mathbf{C}^{-1} \Gamma_{\text{LS}})^{-1} \Gamma_{\text{LS}}^T \mathbf{C}^{-1} \mathbf{R},$$

where  $\mathbf{C}$  is the covariance matrix of the residuals. However, the physical data  $\mathbf{R}$  contains the  $\Gamma_{\text{SS}} \mathbf{a}_{\text{SS}}$  term defined in eq. (62). Substituting the full expression for  $\mathbf{R}$  into the estimator reveals the bias:

$$(64) \quad \hat{\mathbf{a}}_{\text{LS}} = \mathbf{a}_{\text{LS}} + \underbrace{(\Gamma_{\text{LS}}^T \mathbf{C}^{-1} \Gamma_{\text{LS}})^{-1} \Gamma_{\text{LS}}^T \mathbf{C}^{-1} \Gamma_{\text{SS}} \mathbf{a}_{\text{SS}}}_{\text{Leakage Bias}}.$$

The recovered coefficients are thus the sum of the true large-scale signal and a deterministic projection of the small-scale sky. The array's window function essentially aliases high- $\ell$  power into the low- $\ell$  map.

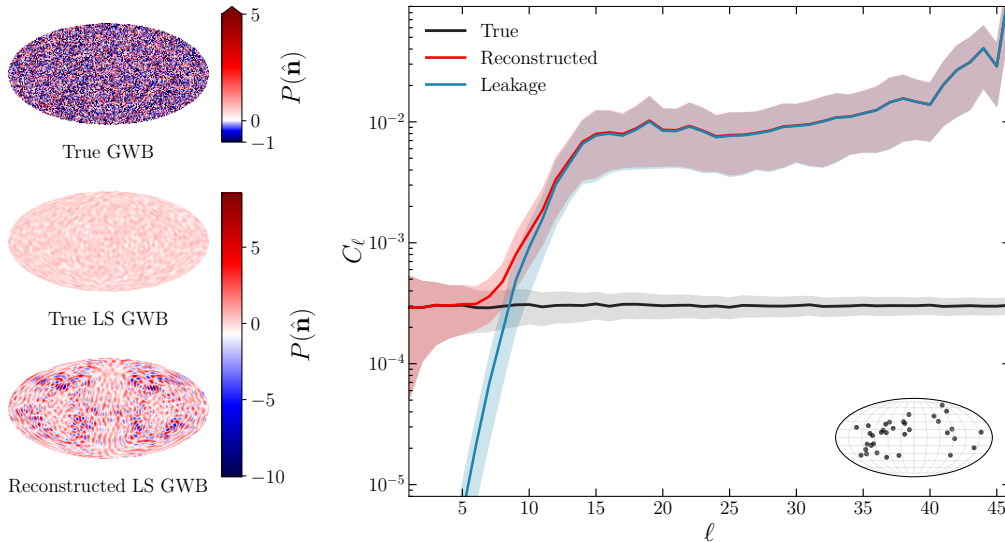


Fig. 11. – *Left panels*: individual realization of a true GWB with power up to  $\ell_{\max}^{\text{GWB}} = 250$  (*top panel*), its large-scale component with power up to  $\ell_{\max}^{\text{rec}} = 22$  (*central panel*), and reconstructed large-scale background, including small-scale leakage, up to  $\ell_{\max}^{\text{rec}} = 22$  (*bottom panel*). *Right panel*: envelopes of true (*black*), reconstructed (*red*), and leakage (*blue*) correlated residual angular power spectra for  $10^3$  realizations of the GWB and the NANOGrav pulsar geometry. Both covariance and likelihood regularization are applied (see [160] for further details). Solid lines indicate the median value of angular power spectra.

This bias propagates when quantifying the angular power spectrum  $C_\ell$ . Since the small-scale coefficients  $\mathbf{a}_{\text{SS}}$  are statistically independent of  $\mathbf{a}_{\text{LS}}$ , the measured power spectrum is inflated. The expectation value of the reconstructed power  $\hat{C}_\ell$  becomes:

$$(65) \quad \langle \hat{C}_\ell^{\text{rec}} \rangle = C_\ell^{\text{true}} + C_\ell^{\text{leakage}} = C_\ell^{\text{true}} + \sum_{\ell' > \ell_{\max}^{\text{rec}}} M_{\ell\ell'} C_{\ell'}^{\text{true}}.$$

Here,  $M_{\ell\ell'}$  is a mode-mixing matrix determined entirely by the array geometry. It quantifies how much power from a physical mode  $\ell'$  leaks into the reconstructed mode  $\ell$ .

fig. 11 illustrates the impact of small-scale leakage for a realistic PTA configuration (NANOGrav 15-yr pulsar sky). The left panels show a single realization of a GWB with power up to  $\ell_{\max}^{\text{GWB}} = 250$  (top), its true large-scale component up to  $\ell_{\max}^{\text{rec}} = 22$  (middle), and the reconstructed large-scale map including leakage (bottom). The reconstructed map is visibly contaminated by spurious small-scale features not present in the true large-scale sky. The right panel quantifies this effect statistically over  $10^3$  realizations. The reconstructed angular power spectrum (red) significantly exceeds the true large-scale spectrum (black) across all multipoles, with the excess power (blue) arising entirely from small-scale leakage.

For astrophysical backgrounds where power is distributed broadly across scales (e.g., a population of discrete binaries tracing LSS), the leakage term  $\sum M_{\ell\ell'} C_{\ell'}$  is non-negligible. This term can overestimate the true large-scale anisotropy by an order of magnitude [160].

The bias persists regardless of observational details. Whether the array samples the

sky isotropically, uniformly, or inhomogeneously (as in NANOGrav), the mode-mixing structure  $M_{\ell\ell'}$  remains qualitatively similar. Introducing regularization schemes to stabilize ill-conditioned matrices (such as ridge penalties or SVD truncation) cannot eliminate the leakage. Regularization modifies the pseudoinverse  $\Gamma_{\text{LS}}^+$ , trading the original leakage for a combination of regularization bias (which pulls the reconstructed large-scale coefficients away from their true values even in the absence of small-scale power) and residual small-scale contamination. Adding realistic timing noise to the covariance matrix does not fundamentally alter the leakage phenomenology, though it modifies the detailed form of  $M_{\ell\ell'}$  by changing the effective weights in the least-squares fit.

The most serious consequence of small-scale leakage emerges when attempting to interpret anisotropy measurements in physical terms. The distorted maps and inflated  $C_\ell$  values are fundamentally incompatible with the true LSS pattern of the SMBHB population. Cross-correlating PTA maps with galaxy catalogs to establish the astrophysical origin of the GWB (sect. 5.4) relies on matching the true large-scale clustering signal. If the GW map contains spurious power leaked from small scales, the inferred correlation will be systematically biased. Since the mode-mixing is geometry-dependent, different PTA configurations analyzing the same sky will infer systematically different (and systematically incorrect) large-scale power spectra, creating apparent inconsistencies between datasets that arise not from cosmic variance but from the different leakage patterns of each array.

Perfect reconstruction of LSS without prior knowledge of small-scale content would require either complete absence of small-scale power ( $\mathbf{a}_{\text{SS}} = \mathbf{0}$ ), achieving extremely high resolution such that  $\mathcal{R}_{\text{SS}} \ll \mathcal{R}_{\text{LS}}$  for all pairs, or constructing estimators with intrinsic orthogonality between large- and small-scale contributions (for instance,  $\Gamma_{\text{LS}}^+ \Gamma_{\text{SS}} = \mathbf{0}$ ). None of these conditions can be met for realistic PTAs. Addressing small-scale leakage will require explicit modeling of the unresolved power in statistical pipelines through joint inference of  $\mathbf{a}_{\text{LS}}$  and parametrized models for the small-scale spectrum, hierarchical Bayesian frameworks that marginalize over small-scale realizations, or orthogonal estimators designed to suppress mode-mixing. As PTAs improve their sensitivity and expand to larger arrays, understanding and mitigating this systematic effect will be essential for reliable anisotropy detection and interpretation.

**5.6. Recent Results and Future Prospects.** – To date, dedicated searches for GWB anisotropy have been carried out by EPTA [134], NANOGrav [137], MPTA [146], and PPTA [147].

The NANOGrav 15-yr anisotropy search [137] placed a 95% upper limit on the dipole power ( $C_1/C_0 \lesssim 27\%$ ). However, the search was restricted to low frequencies ( $f < 10$  nHz), where millions of sources contribute per frequency bin and the background is expected to be nearly isotropic. Furthermore, constraints on higher multipoles ( $\ell > 1$ ) effectively returned the Bayesian prior, indicating that current low-frequency data is insensitive to small-scale structure.

In contrast, recent results from the MPTA offer a glimpse into the high-frequency regime where anisotropy is physically expected. Using the radiometer (eq. (50)) on only 4.5 years of data but with high cadence, MeerKAT probed frequencies up to  $\sim 21$  nHz. At these frequencies, the source population thins out, and “popcorn” shot noise should begin to dominate. Intriguingly, the MeerKAT analysis recovered a  $\sim 2\sigma$  power fluctuation at a sky location coincident with J1536+0441, a SMBHB candidate identified with the NANOGrav 15-yr data, but which is itself consistent with noise [146, 150].

The PPTA DR3 analysis by Chen et al. [147] employed both radiometer and square-

root spherical harmonic bases on 30 MSPs spanning up to 18 years, performing a per-frequency search in the lowest five frequency bins. No statistically significant anisotropy was found: the angular power spectra in the square-root spherical harmonic basis remain below the  $3\sigma$  detection threshold at all multipoles and frequencies. However, a potential hotspot at 5.26 nHz was identified in both bases ( $p = 0.016$  in the radiometer,  $p = 0.021$  in the spherical harmonic analysis), though it lies in a region of low array sensitivity and has no corresponding CW signal in PPTA DR3 searches. This feature is reminiscent of the  $\sim 2\sigma$  hotspot at 7 nHz found by the MPTA [146].

These results align with recent theoretical modeling by Gardiner et al. [161] and Lemke et al. [158]. They demonstrate that while the low-frequency GWB is smooth, the popcorn noise from individual sources becomes the dominant feature at  $f \gtrsim 10$  nHz, consistent with the analytical derivation from [56], eq. (56). Their models predict that anisotropy should be readily detectable in this regime ( $C_{\ell>0}/C_0 \sim 10^{-2} - 10^{-1}$ ), which may help turn high-frequency anisotropy searches into a tool for identifying sub-threshold CW candidates.

Schult et al. [162] have introduced a “frequency-resolved anisotropy” search designed to exploit this regime. Unlike standard GWB searches that integrate over a broad frequency band assuming a power-law spectrum, this “spike-pixel” approach searches for excess power localized in both sky position and frequency bin, allowing pixel-based methods to identify candidate CW sources as hotspots of monochromatic power even when the S/N is insufficient for a full deterministic template fit.

Future analyses may therefore pivot to this transition zone. The intrinsic anisotropy grows steeply with frequency ( $C_{\ell>0}/C_0 \propto f^{11/3}$ ; eq. (56)), directing searches to high-frequency bins, while extended baselines improve frequency resolution ( $\Delta f = 1/T_{\text{obs}}$ ) and expanding the array increases  $\ell_{\text{max}} \sim N$ . Per-frequency estimators such as the anisotropic PFOS [163] are specifically designed for this regime, localizing anisotropy to individual frequency bins while properly accounting for inter-pair covariance and cosmic variance [159]. A systematic frequentist forecast by Konstandin et al. [145] quantifies the prospects and limitations of such searches, finding that broadband searches lose sensitivity compared to per-frequency approaches. By combining the long baselines of the IPTA with the high cadence and low white noise of the SKAO and the future DSA-2000, we can move beyond upper limits and begin to map the discrete sources that comprise the GW sky.

## 6. – Continuous Gravitational Waves

The search for individual, inspiraling SMBHBs complements the search for GWB anisotropy and the evidence for the monopole (or the isotropic GWB). While the GWB arises from the incoherent superposition of millions of unresolvable sources, CWs are deterministic, monochromatic signals from the loudest individual binaries in the cosmic population.

Theoretical work has shown that the isotropy of the GWB is an approximation; individual realizations of the Universe produce a jagged strain spectrum dominated by the few nearest or most massive sources [40, 46, 56, 89, 106, 164]. The resulting anisotropy (sect. 5) and polarization of the background are intimately connected to the CW source population: a single bright binary contributes both a deterministic CW signal and a localized “hotspot” in the GWB intensity and polarization maps (sect. 5.2.1). However, current analysis pipelines typically separate the problem into two distinct strategies: (1) All-Sky Searches, which scan the entire sky for unknown sources, and (2) Targeted

Searches, which leverage electromagnetic catalogs to test specific binary hypotheses.

**6.1. Electromagnetic Counterparts.** – Electromagnetic counterparts to SMBHBs are essential for realizing the multi-messenger potential of PTAs (for recent reviews, see [67, 165–167]). With PTA CW detections expected to have poor sky localization (90% credible areas of  $\sim 30$ –240 deg<sup>2</sup>; [168]), an electromagnetic association is often the only practical route to identifying a unique host galaxy and measuring a redshift. Beyond localization, electromagnetic data provide independent constraints on the astrophysical environment (gas-rich versus gas-poor), the accretion state, and the dynamical mechanisms that govern binary hardening (sect. 4; eq. (37)).

In gas-rich systems, the leading expectation is that a SMBHB excavates a low-density cavity while accreting through streams that feed mini-disks. Time-dependent accretion can imprint periodic variability across optical, UV, and X-ray bands [169, 170]. Observationally, time-domain surveys have produced large samples of periodically varying quasars (e.g., [171, 172]), though these are subject to high false-positive rates from red noise and quasi-periodic disk variability. Spectroscopy offers a complementary handle via offset broad lines or drifting velocity centroids [173, 174], while direct imaging with e.g. VLBI can resolve dual nuclei at wider (kpc-scale) separations (fig. 6). However at those separations, the black holes are not yet emitting significant gravitational radiation [175].

**6.2. Signal Model.** – The timing residual induced by a continuous GW source is the contraction of the transverse-traceless metric perturbation  $h_{ab}(t, \hat{\Omega})$  with the impulse response of the pulsar–Earth baseline. For a source located at sky position  $\hat{\Omega}$ , the residual  $s(t)$  in a pulsar  $p$  is given by:

$$(66) \quad s(t) = \sum_{A=+, \times} F^A(\hat{\Omega}) [h_A(t) - h_A(t_p)],$$

where  $t_p = t - L(1 + \hat{\Omega} \cdot \hat{p})/c$  is the retarded time at the pulsar (see sect. 2.2 for the general Earth–Pulsar term decomposition), and  $F^A$  are the antenna pattern functions. The two terms in brackets sample the binary at two epochs separated by the light-travel time  $L/c \sim 10^3$ – $10^4$  yr; we exploit this in sect. 6.11 to measure binary evolution over millennial timescales.

A frequent point of confusion in the literature is the treatment of the polarization angle,  $\psi$ . In some conventions,  $\psi$  appears explicitly in the antenna patterns  $F^A(\hat{\Omega}, \psi)$ ; in others, it is absorbed into the time-dependent waveform components  $h_A(t, \psi)$ . These two approaches are mathematically equivalent, representing a choice of basis vectors for the polarization tensor.

**6.2.1. The Polarization Angle as a Basis Rotation.** The GW polarization is defined relative to a set of principal axes perpendicular to the propagation direction  $\hat{\Omega}$ . Let us define a fixed celestial basis  $(\hat{u}, \hat{v})$  in the plane of the sky (e.g., aligned with Right Ascension and Declination). The principal axes of the source, denoted  $(\hat{m}, \hat{n})$ , are rotated relative to this fixed basis by the polarization angle  $\psi$ :

$$(67) \quad \begin{aligned} \hat{m} &= \hat{u} \cos \psi + \hat{v} \sin \psi \\ \hat{n} &= -\hat{u} \sin \psi + \hat{v} \cos \psi \end{aligned}$$

The metric perturbation can be written in the source frame  $(\hat{m}, \hat{n})$  using the intrinsic amplitudes  $\mathcal{A}_+$  and  $\mathcal{A}_\times$ :

$$(68) \quad h_{ab}(t) = \mathcal{A}_+(t)(\hat{m}_a\hat{m}_b - \hat{n}_a\hat{n}_b) + \mathcal{A}_\times(t)(\hat{m}_a\hat{n}_b + \hat{n}_a\hat{m}_b).$$

Substituting the rotation relations for  $\hat{m}$  and  $\hat{n}$  into this equation projects the waveform onto the fixed sky basis  $(\hat{u}, \hat{v})$ . This operation mixes the plus and cross components via the double-angle terms  $\cos 2\psi$  and  $\sin 2\psi$ . This leads to two distinct conventions for writing the signal model:

*Convention I:  $\psi$  in the Waveform*

In this convention, we fix the antenna patterns to the celestial basis  $(\hat{u}, \hat{v})$ . The antenna patterns  $F^+(\hat{\Omega})$  and  $F^\times(\hat{\Omega})$  depend only on the source and pulsar positions. The polarization angle  $\psi$  is carried by the waveform terms  $h_{+,\times}(t)$ .

$$(69) \quad \begin{aligned} h_+(t) &= -\sin[2\Phi(t)](1 + \cos^2 \iota) \cos 2\psi - 2 \cos[2\Phi(t)] \cos \iota \sin 2\psi \\ h_\times(t) &= -\sin[2\Phi(t)](1 + \cos^2 \iota) \sin 2\psi + 2 \cos[2\Phi(t)] \cos \iota \cos 2\psi \end{aligned}$$

*Convention II:  $\psi$  in the Antenna Pattern*

Alternatively, one can define the antenna patterns aligned with the source axes  $(\hat{m}, \hat{n})$ . In this case, the waveform  $h_{+,\times}(t)$  describes the intrinsic strain in the binary frame (independent of  $\psi$ ), and the antenna patterns become functions of  $\psi$ , related to the Convention I patterns  $F^{+,\times}(\hat{\Omega})$  by:

$$(70) \quad \begin{aligned} F^+(\hat{\Omega}, \psi) &= \cos 2\psi F^+(\hat{\Omega}) + \sin 2\psi F^\times(\hat{\Omega}) \\ F^\times(\hat{\Omega}, \psi) &= -\sin 2\psi F^+(\hat{\Omega}) + \cos 2\psi F^\times(\hat{\Omega}) \end{aligned}$$

While physically identical, this convention implies that the ‘‘sensitivity’’ of the detector changes as the source rotates, which can be conceptually less transparent for array-wide analyses. For clarity and computational efficiency, we recommend Convention I: treating  $F^A$  as fixed geometric coefficients and including the  $\psi$  rotation matrices directly in the signal templates.

**6.3. All-Sky Searches.** – All-sky searches attempt to detect CWs without prior spatial or frequency information (fig. 12). This pipeline must marginalize inclination, polarization, and phase.

The sensitivity of these searches has improved steadily, but they have yet to yield a detection. The most recent constraints are summarised in tab. II. The NANOGrav 15-yr [150], IPTA DR2 [176], and PPTA DR3 [177] searches report sky-averaged 95% upper limits on the strain amplitude  $h_0$  at specific frequencies where each array is most sensitive. The PPTA DR3 is sensitive to binaries with  $\mathcal{M} \geq 10^9 M_\odot$  out to luminosity distances of 50–200 Mpc, depending on sky direction. The EPTA DR2 analysis [178] takes a different approach: rather than reporting per-frequency upper limits, it constrains the strain amplitude jointly across the full searched band using a Bayesian model comparison framework, obtaining  $\log_{10} h_{95} = -13.75$  for a model that includes a Hellings–Downs-correlated GWB, per-pulsar custom noise (PSRN), and a single continuous GW source (GWB+PSRN+CGW). The EPTA array is most sensitive near 20 nHz, where binaries with  $\mathcal{M} > 10^9 M_\odot$  are detectable out to the Virgo and Fornax clusters (16.5 and 19.3 Mpc, respectively).

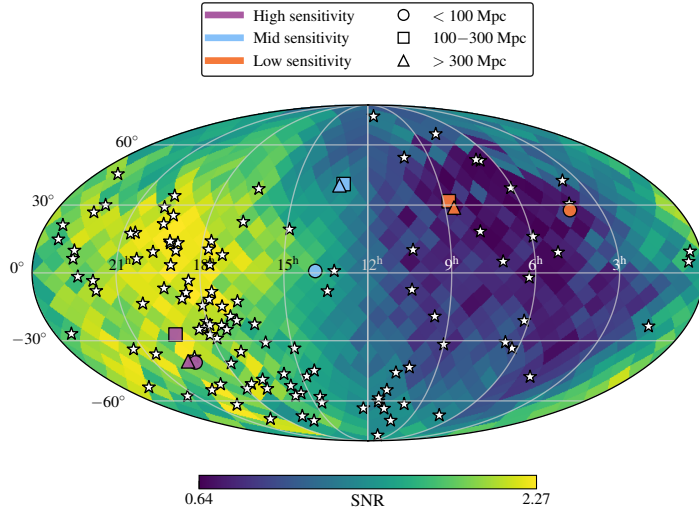


Fig. 12. – Skymap of the simulated PTA sensitivity, where each pixel is colored by the expected  $S/N$  of a CW source at fixed  $d_L = 150$  Mpc, averaged over GW frequencies (2, 6, 20 nHz), chirp masses ( $10^8$  and  $10^9$ ,  $M_\odot$ ), and 100 random draws of  $\cos \iota$ ,  $\psi$ , and  $\Phi_0$ . Pulsar positions are shown as white stars. We inject into nine galaxies, grouped by sensitivity into high (purple), mid (light blue), and low (orange) regions, demarcated by ellipses of the same color. Within each group, injections span three distance bins: near ( $< 100$  Mpc, circles), mid (100-300 Mpc, squares), and far ( $> 300$  Mpc, triangles). Figure by P. Petrov

A critical systematic hurdle for all-sky searches is “GWB confusion.” As array sensitivity improves, the threshold for detecting a single source drops into the regime of the stochastic background itself. The EPTA DR2 analysis recently identified a candidate at  $\sim 4.6$  nHz with a Bayes factor favoring a CW against uncorrelated noise. However, when a Hellings-Downs-correlated GWB component was added to the model, the Bayes factor for the CW dropped to  $\sim 1$ , indicating that the signal was indistinguishable from the background. This degeneracy implies that blind searches may be reaching a confusion limit where identifying a unique source requires higher  $S/N$  than previously expected. A promising path forward is to exploit the deterministic cross-correlation fingerprint of a CW source, which differs qualitatively from the Hellings-Downs curve of the isotropic GWB (sect. 6.7).

**6.4. Targeted Searches.** – Targeted searches fix the source parameters—sky location ( $\hat{\Omega}$ ), luminosity distance ( $D_L$ ), and often the GW frequency ( $f_{\text{GW}}$ )—based on electromagnetic evidence. This creates a highly conditional, falsifiable test: *if* a specific galaxy hosts a binary as described by electromagnetic models, is it consistent with PTA data?

A recent comprehensive study using the NANOGrav 15-yr dataset applied this method to 114 SMBHB candidates selected from the CRTS, ZTF, and radio catalogs [42]. By fixing source parameters, the study achieved a median sensitivity improvement of  $2.6\times$  (and up to  $15\times$ ) relative to all-sky limits at the same frequency. These constraints are now beginning to cut into the astrophysically plausible parameter space for objects like 3C 66B, ruling out high-mass binary models that were previously allowed Iguchi et al. [179]. The analysis highlighted two candidates, J1536+0441 and J0729+4008, whose

TABLE II. – *Current sky-averaged 95% upper limits on the CW strain amplitude from all-sky searches. For NANOGrav, IPTA, and PPTA the frequency column lists the single frequency of peak sensitivity; for EPTA DR2 it lists the Bayesian search band over which the limit is obtained jointly (see text).*

PTA	Data set	$h_0^{95\%}$	$f$ (nHz)	Ref.
NANOGrav	15-yr	$8 \times 10^{-15}$	6	[150]
IPTA	DR2	$9.1 \times 10^{-15}$	10	[176]
PPTA	DR3	$7 \times 10^{-15}$	10	[177]
EPTA	DR2	$17.8 \times 10^{-15}$	1–14	[178]

Bayes factors initially favored a CW over the rest of the population. Ruling them out required developing a systematic detection protocol, described below.

**6.5. The first steps of a protocol for CW detection.** – A statistically significant Bayes factor is a necessary, but not sufficient, condition for claiming a CW detection. Based on the analysis of candidates in the NANOGrav 15-yr targeted search, Agarwal et al. [42] define a suite of ten tests divided into three categories—electromagnetic (electromagnetic) consistency checks, GWB consistency checks, and statistical validation checks—which we reproduce here as a concrete example of the multi-messenger vetting required for CW claims (tab. 2 of [42]). This checklist applies specifically to the case of targeted searches where priors are drawn from periodic light curves in an electromagnetic catalog, though the framework is likely useful more broadly.

*Electromagnetic consistency checks.*—These tests verify that the electromagnetic properties of the candidate are consistent with the binary hypothesis:

1. **Extended Periodicity:** The optical or infrared periodicity that originally flagged the candidate must persist in extended monitoring. A periodicity that fades or changes character in new data undermines the binary hypothesis.
2. **Spectral Features:** Broad emission line profiles (e.g.,  $H\alpha$ ,  $H\beta$ ) should show velocity shifts or profile changes consistent with orbital motion over the baseline of spectroscopic monitoring.

*GWB consistency checks.*—These tests assess whether the candidate is consistent with the measured GWB and astrophysical population models:

3. **CRTS–GWB Consistency:** The number of periodic AGN candidates in surveys such as CRTS that are consistent with being SMBHBs should be compatible with the rate predicted by the measured GWB amplitude and SMBHB population models.
4. **Population Synthesis:** The GW-inferred total mass and frequency of the candidate should fall within the credible region of simulated SMBHB populations drawn from galaxy merger rates and scaling relations.
5. **GWB Anisotropy:** A sufficiently loud CW source should produce a detectable anisotropy in the GWB at its sky location and frequency (sect. 5.2.1), and should leave a flat imprint in the GWB strain spectrum across all  $\ell$  at the source frequency.

*Statistical validation checks.*—These tests probe whether the GW signal itself is robust:

6. **Distinct from GWB:** The candidate must remain significant when a Hellings–Downs-correlated GWB component is included in the noise model. A signal that is absorbed by the GWB ( $\mathcal{B}_{\text{HD}}^{\text{CW+HD}} \approx 1$ ) may be a fluctuation of the stochastic background rather than a discrete source.
7. **Signal Coherence:** A true CW induces a coherent phase evolution across the array. This is tested by scrambling the phases or sky positions of the pulsars [180]; a detection is robust only if the unscrambled Bayes factor is a significant outlier ( $p < 0.003$ ) relative to the scrambled null distribution.
8. **Dropout Analysis:** The support for the signal should be distributed across the array, rather than driven by a single noisy pulsar. A dropout analysis [181] calculates the Bayes factor contribution from each pulsar; if the signal vanishes when a single pulsar is removed, it is likely a noise artifact (e.g., unmodeled red noise or ISM events).
9. **Random Targeting:** The candidate should not be consistent with noise after accounting for the number of targets searched. If random sky positions produce comparable Bayes factors after trial-factor corrections, the detection is not significant.
10. **Software Cross-check:** Results must be reproduced with independent analysis pipelines (e.g., `enterprise` and `QuickCW`) to guard against software-specific systematics.

The IPTA has established a CW Detection Task Force to develop and formalize such protocols for the global array, and future efforts in this vein will be essential as sensitivity improves and the first credible candidates emerge.

**6.6. Comparison: Targeted vs. All-Sky.** – The choice between all-sky and targeted searches represents a trade-off between discovery space and sensitivity. All-sky searches are unbiased and can find “dark” binaries invisible to electromagnetic surveys, but they are computationally expensive and suffer from poor localization ( $> 100 \text{ deg}^2$ ) and high trial factors. Targeted searches improve strain sensitivity by factors of  $\sim 2$ – $10$  and enable immediate host identification, but they are blind to sources not present in electromagnetic catalogs.

Crucially, the two methods face different limiting factors. All-sky searches are currently limited by *GWB confusion*—the inability to distinguish a single weak source from the collective background. Targeted searches bypass this by fixing the spatial correlations, but they are limited by the *quality of electromagnetic priors* (e.g., uncertainty in the  $P_{\text{orb}}$  to  $f_{\text{GW}}$  mapping). Future progress will likely require a hybrid approach: using all-sky maps to identify “hotspots” of excess power, which are then cross-correlated with galaxy catalogs to perform targeted follow-up.

**6.7. Deterministic Fingerprints of CWs.** – A single bright SMBHB is the deterministic limit of the stochastic background, and one can treat the spatial cross-correlations as the primary observable in both regimes. In standard practice, stochastic searches use cross-correlations (via the Hellings–Downs curve), while CW searches often emphasize per-pulsar matched filtering in the time domain. This division creates a method gap: the

same physical detector is being analyzed with two inconsistent notions of what constitutes signal.

The appropriate unifying object is the single-source overlap reduction function (ORF),  $\Upsilon_{ab}$  [182]. For a single monochromatic source at sky location  $\hat{\Omega}_0$ , the time-averaged cross-correlation of the timing residuals between pulsars  $a$  and  $b$  is, in the Earth-term limit, is the function  $\Upsilon_{ab}$ . It is purely geometric: it depends on the source direction  $\hat{\Omega}_0$ , the binary inclination  $\iota$ , polarization angle  $\psi$ , and the positions of pulsars  $a$  and  $b$ , but not on the source amplitude or frequency. It is the kernel of the Hellings–Downs curve: the isotropic stochastic ORF  $\Gamma_{ab}$  introduced in sect. 2.4 is the sky average of  $\Upsilon_{ab}$  over source directions (eq. (75)). Note that the integrand  $F_a^+ F_b^+ + F_a^\times F_b^\times$  used to derive the Hellings–Downs curve in sect. 2.4 is the same expression after averaging over  $\iota$  and  $\psi$ ; the full  $\Upsilon_{ab}$  retains this orientation dependence. Unlike the Hellings–Downs curve,  $\Upsilon_{ab}$  explicitly breaks statistical isotropy.

Working in a computational frame where pulsar  $a$  lies on the  $+\hat{z}$  axis and pulsar  $b$  lies in the  $x$ - $z$  plane at angular separation  $\zeta$ , Mingarelli et al. [182] derive a closed-form expression for the single-source ORF of a GW source propagating from direction  $(\theta, \phi)$ :

$$(71) \quad \Upsilon_{ab}(\theta, \phi, \zeta, \iota, \psi) = \frac{1}{8} (1 + 6 \cos^2 \iota + \cos^4 \iota + \sin^4 \iota \cos 4\psi) \mathcal{K} \mathcal{N}_+ - \frac{1}{4} \sin^4 \iota \sin 4\psi \mathcal{K} \mathcal{N}_\times,$$

with

$$(72) \quad \mathcal{K}(\theta, \phi, \zeta) \equiv \frac{1 - \cos \theta}{1 + \cos \theta \cos \zeta + \sin \theta \sin \zeta \cos \phi},$$

$$(73) \quad \mathcal{N}_+(\theta, \phi, \zeta) \equiv (\cos \phi \cos \theta \sin \zeta - \sin \theta \cos \zeta)^2 - \sin^2 \phi \sin^2 \zeta,$$

$$(74) \quad \mathcal{N}_\times(\theta, \phi, \zeta) \equiv \sin \zeta \sin \phi (\cos \theta \sin \zeta \cos \phi - \sin \theta \cos \zeta).$$

Here  $\mathcal{K}$  is a geometric kernel encoding the Earth-term timing response, and  $\mathcal{N}_+$ ,  $\mathcal{N}_\times$  capture the  $+$ - and  $\times$ -polarization responses respectively [182]. Unlike the Hellings–Downs curve, which depends only on pulsar separation, eq. (71) depends on the specific sky location of the GW source relative to each pulsar pair as well as the binary inclination and polarization angle. Each SMBHB therefore imprints a distinct geometric fingerprint on the array, encoding its sky position and polarization content.

Explicitly,

$$(75) \quad \Gamma_{ab} \propto \int \frac{d\hat{\Omega}}{4\pi} \Upsilon_{ab}(\hat{\Omega}, \iota, \psi),$$

so deviations from Hellings–Downs in realistic SMBHB populations can be interpreted as incomplete averaging over a finite number of bright fingerprints rather than as a failure of the stochastic framework.

It is important to distinguish this pair-level fingerprint from the separation-averaged correlation studied by Cornish and Sesana [183], who demonstrated that even a single bright binary reproduces the Hellings–Downs curve once the cross-correlations are binned by angular separation and averaged over many pulsar pairs. For a sufficiently large, isotropically distributed array, this pair-averaging is equivalent to integrating over source directions, so the mean correlation as a function of  $\zeta$  converges to Hellings and

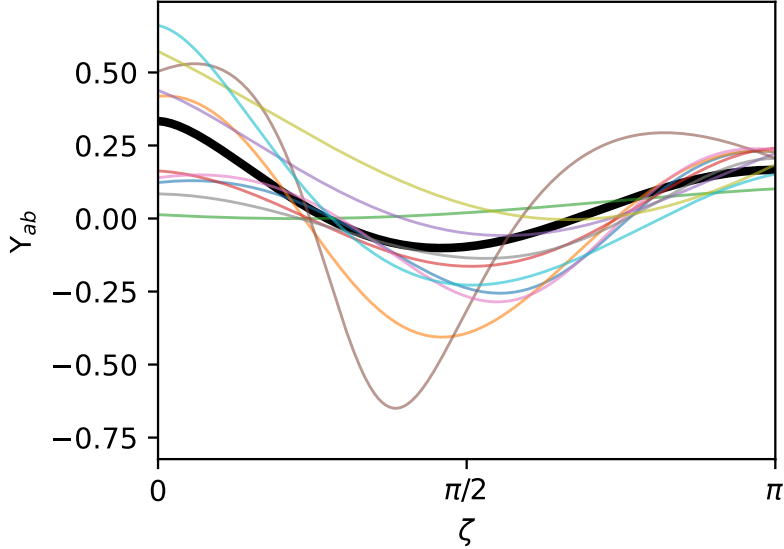


Fig. 13. – Single-source fingerprints  $\Upsilon_{ab}(\zeta)$  (eq. (71)) for 10 randomly drawn GW source sky locations, each shown as a colored, un-normalized curve. The Hellings–Downs curve (black) is the sky-average of these fingerprints (eq. (75)). Individual fingerprints can differ markedly from Hellings–Downs, illustrating that a single bright SMBHB imprints a geometry-dependent pattern on the array that is generically non-Hellings–Downs. Figure adapted from Ref. [182].

Downs regardless of whether the signal is a Gaussian background or a single quadrupolar source. The fingerprint  $\Upsilon_{ab}$  addresses a complementary question: what is the exact cross-correlation between a specific pair of pulsars for a source at a particular sky location? This pair-level pattern generically departs from the Hellings–Downs curve and depends on the full set of angles  $(\theta, \phi, \zeta, \iota, \psi)$ . The Hellings and Downs limit is recovered only upon averaging  $\Upsilon_{ab}$  over source directions or, equivalently, over pulsar positions at fixed separation [183, 184]. The scatter and variance around the Hellings and Downs curve observed in population-level simulations [50, 162, 185] can therefore be traced to incomplete averaging over a finite number of single-source fingerprints.

The practical consequence is that  $\Upsilon_{ab}$  provides a direct test between a single CW and an isotropic background even when the spectral models are identical. A CW can masquerade as a GWB in analyses that only fit for a common red process with a fixed Hellings and Downs ORF.

Injection-and-recovery studies in simulated PTA data compare four cross-correlated spectral models for a single CW source [182]: the full  $\Upsilon_{ab}(\theta, \phi, \zeta, \iota, \psi)$  model; the spike-pixel (SP) model, sect. 5.1.3; a Hellings–Downs-correlated model, eq. (25); and a purely auto-correlated (diagonal) model. At template  $S/N = 30$ , the Bayes factors over pulsar noise alone are  $\mathcal{B} \approx 1611$  ( $\Upsilon_{ab}$ ),  $\mathcal{B} \approx 159$  (Hellings–Downs), and  $\mathcal{B} > 1$  (diagonal). The  $\Upsilon_{ab}$  model is favored over the SP model at all  $S/N$  ( $\mathcal{B}_{\text{SP}}^{\Upsilon} = 2.14 \pm 0.02$  at  $S/N = 30$ ), reflecting the additional constraining power of the inclination and polarization angles (sect. 6.2.1). The Hellings–Downs-correlated search recovers excess power at the correct GW frequency but absorbs it into an isotropic GWB component—the degeneracy dis-

cussed in sect. 6 and noted by Cornish and Sesana [183]. At  $S/N = 15$ , the  $\Upsilon_{ab}$ -based models yield  $\mathcal{B}^{\text{CW}} > 1$  while the Hellings–Downs and auto-correlated models do not. Importantly, sky localization improves by a factor of  $\sim 11\times$  when cross-correlations are included.

This is especially relevant for the weak-signal regime that PTAs will inhabit for first evidence of individual binaries, where the total signal power can be dominated by auto-correlations. In that limit, time-domain coherence tests that require precise pulsar distances are difficult: exploiting pulsar terms coherently demands distance knowledge at the level of a GW wavelength. In contrast, Earth-term fingerprints require only spatial cross correlations, in analogy with the Hellings and Downs curve. Cross-correlated spectral searches based on  $\Upsilon_{ab}$  therefore provide a robust intermediate step between stochastic detection and fully coherent CW matched filtering.

Operationally, one can view  $\Upsilon_{ab}$  as the natural statistic for an early detection protocol: (i) detect excess power; (ii) demonstrate spatial coherence against a conservative null (e.g., an auto-correlated CW-like model); (iii) test the CW fingerprint against the isotropic Hellings–Downs hypothesis or together with it; and (iv) only then attempt full coherent waveform inference with pulsar terms (sect. 6.11) where warranted by data quality and distance precision (sect. 6.12).

**6.8. Strong Lensing.** – Just like electromagnetic signals, GWs from distant sources can be lensed by foreground mass distributions such as stars, galaxies, and galaxy clusters. While electromagnetic signals become louder by a factor of  $\mu$ —the magnification factor associated with the lens surface mass distribution—the strains of GW signals from individual sources experience amplification by a factor of  $\sqrt{\mu}$  such that  $h_{\text{lensed}} = \mu^{1/2}h$ , see e.g. Ezquiaga [187]. Strong lensing in particular also gives rise to multiple images of the background source. Khusid et al. [188] investigates strong gravitational lensing as a tool for broadening the PTA sensitive volume and extracting richer multimessenger information from SMBHB systems.

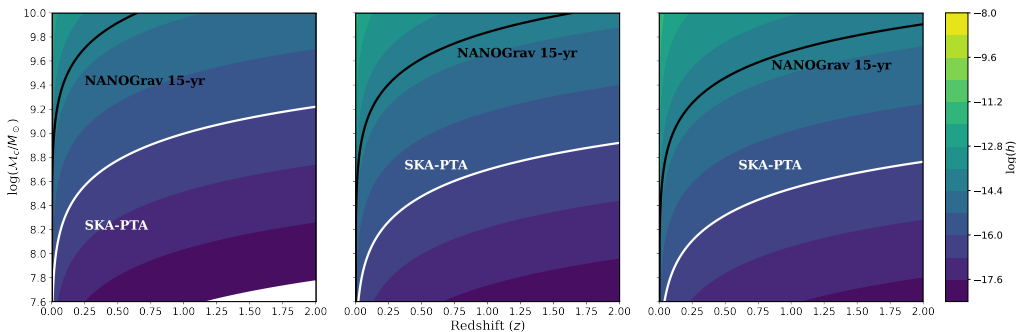


Fig. 14. – Strong lensing of GWs improves the PTA detection volume by sufficiently amplifying the strains of signals from distant and/or not massive enough binary systems. These GWs can be detected by current and future PTAs, namely NANOGrav (15-yr dataset strain upper limit [150], black) and SKA-PTA, see Xin et al. [186] (white). For a fixed  $f_{\text{GW}} = 6$  nHz (presently the most sensitive GW frequency [150]), we demonstrate the broadening of detectable  $z$ – $\mathcal{M}$  parameter space under three representative lensing scenarios: (left) a simplified spherical foreground lens model with a modest  $\mu = 3$ , (center) an elliptical lens model with  $\mu = 30$ , and (right) an elliptical lens model with optimistic  $\mu = 100$ .

Lensing improves PTA detection prospects two-fold, by amplifying otherwise sub-threshold CW signals produced by sources that are too far away or not massive enough, see eq. (28). For example, a constant  $\mu = 3$  due to strong lensing not only increases the PTA detection volume by a factor of  $\sim 5$  for a fixed set of intrinsic SMBHB properties, but it also permits the detection of GWs from systems that are  $3^{3/10} \approx 1.4$  times less massive in chirp mass for fixed  $D_L(z)$  and  $h$ . The most recent result from the NANOGrav 15-yr dataset [150] places a 95% upper limit of  $8 \times 10^{-15}$  on CW strain amplitude, while future datasets in the SKAO era (henceforth SKA-PTA) are expected to be sensitive to  $h \gtrsim 10^{-16}$  [186]. fig. 14 gives three different cases of magnification— $\mu = 3, 30,$  and  $100$ , for lensing configurations ranging from modest to exceptional, respectively—to demonstrate how the amplification of CW strain from strong lensing effectively improves PTA sensitivity.

Ref. [188] predicts the number of expected SKA-PTA-detectable strongly lensed SMBHBs as a function of redshift and the additional astrophysical information that such sources offer by virtue of lensing effects. The population calculation entails binning the  $z$ — $\mathcal{M}$  parameter space, populating those bins with SMBHBs emitting detectable lensed GWs ( $h_{\text{lensed}} \geq 10^{-16}$ ) using a BH mass function derived from either a GSMF [190] or a QLF [128], and applying cuts according to binary fraction and strong lensing probabilities. The authors take the result calculated using the QLF to be representative, since there exists sufficient evidence for quasars as tracers of galaxy mergers, hence SMBHB

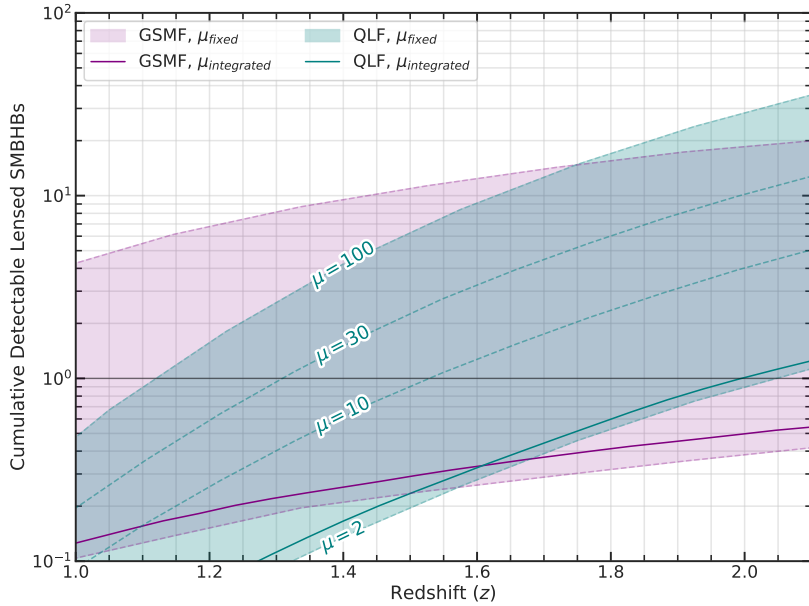


Fig. 15. – The predicted cumulative distribution of detectable strongly lensed SMBHBs in the SKA-PTA era, computed using both the GSMF (purple) and the QLF (teal). The wide bands show the spread of the population for different magnification  $2 \leq \mu \leq 100$ , fixed- $\mu$  examples given by the dashed curves. The solid curves represent a representative population obtained by marginalizing over  $\mu$  in each  $z$ — $\mathcal{M}$  bin according to the probability density function given in Dai et al. [189] (see Sec. 4.4.2 of [188]). The most realistic distribution—the solid teal curve—yields approximately a few detectable strongly lensed systems within  $z \approx 2$ .

mergers [191], and find an expected  $\sim$  few detectable strongly lensed SMBHBs within  $z \approx 2$  as shown in fig. 15.

Those detectable strongly lensed sources serve as exciting candidates for extracting multi-messenger astrophysics. In particular, the binary separation of a sufficiently low- $f_{\text{GW}}$  lensed SMBHB might be amplified enough for electromagnetic counterparts of the individual SMBHBs to be electromagnetically resolvable within each image [188] by multi-wavelength instruments such as ngVLA [192], VLBI [193], and the SKAO itself [194]. If such a binary is in an opportune caustic configuration with respect to a foreground elliptical galaxy lens, see e.g. Barnacka [195], sufficient time delays between images would permit the tracking of its frequency evolution across different PTA frequency bins [188]. These “golden” binaries will be some of the most rich multi-messenger systems in the Universe upon their detection

**6.9. Joint Likelihood Multi-Messenger Analysis.** – The standard approach to multi-messenger characterization has been to use electromagnetic surveys to identify candidates, which are then used to construct priors for a targeted PTA search. While effective, this priors-only method discards information by treating the datasets as independent. A more rigorous framework, recently introduced by Charisi et al. [196], employs a joint likelihood analysis that simultaneously fits the electromagnetic light curves and the pulsar timing residuals as a single data stream.

In this framework, the total likelihood is the product of the individual instrument likelihoods,  $\mathcal{L}_{\text{tot}} = \mathcal{L}_{\text{em}} \times \mathcal{L}_{\text{PTA}}$ , linked by common physical parameters (e.g., chirp mass  $\mathcal{M}$ , period  $P_{\text{orb}}$ , and inclination  $\iota$ ). Ref. [196] demonstrated that this approach significantly tightens parameter constraints compared to separate analyses. By leveraging the sensitivity of light curves to orbital phase and period alongside the PTA’s sensitivity to mass and distance, the joint fit breaks degeneracies between e.g. chirp mass and luminosity distance, that are inherent in single-messenger studies.

The primary promise of the joint likelihood approach is its ability to extract measurements from signals that would be sub-threshold in either detector alone. It effectively lowers the detection horizon by demanding consistency between the two channels. However, the method is computationally expensive and highly model-dependent. It relies on the assumption that the electromagnetic variability (e.g., Doppler boosting or accretion modulation) is correctly modeled; a mismatch between the assumed electromagnetic mechanism and the physical reality could bias the recovered GW parameters. It also requires high-cadence electromagnetic monitoring contemporaneous with PTA observations to track the orbital phase coherently [196].

**6.10. Cosmology with Bright Sirens.** – Beyond characterizing binary astrophysics, CW detections offer a novel probe of cosmology. A SMBHB detected by a PTA acts as a standard siren: the GW signal provides a direct measurement of the luminosity distance  $D_L$ , independent of the cosmic distance ladder [197, 198]. If the binary has an identified electromagnetic counterpart (a “bright siren”), the host galaxy provides the redshift  $z$ .

The combination of a GW-derived  $D_L$  and an electromagnetically derived  $z$  allows for a direct measurement of the Hubble constant  $H_0$  [199]. Constraining the dark energy equation of state  $w$  requires sources at redshifts where the  $D_L(z)$  relation is sensitive to the expansion history beyond  $H_0$ , which is likely beyond the reach of current PTAs but may become accessible in the SKAO era. Unlike standard candles (e.g., Cepheids, Supernovae Ia), standard sirens do not require calibration against local anchors, making them an invaluable cross-check on the current “Hubble tension” between early- and late-

Universe measurements [200, 201].

The precision of a bright siren measurement depends critically on breaking the degeneracy between the binary inclination  $\iota$  and  $D_L$  that is inherent in the GW amplitude. An independent electromagnetic constraint on  $\iota$ —for example from spectroscopic radial-velocity modelling of a binary AGN—would significantly tighten  $D_L$ , but such measurements remain challenging and model-dependent [166]. Wang et al. [199] estimate that even with the  $\iota$ - $D_L$  degeneracy, a small number of bright sirens at  $z \lesssim 0.1$  could yield competitive  $H_0$  constraints, particularly when combined with the joint likelihood framework of sect. 6.9.

**6.11. Binary Evolution: The PTA Time Machine.** – While the Pulsar term acts as incoherent self-noise for stochastic background searches (sect. 2.2), it is a vital signal for single-source science. For a CW source, the binary evolves (chirps) due to GW emission. The light-travel delay  $\tau_a \sim L_a/c \sim 10^3$ – $10^4$  yr means that the Pulsar term provides a snapshot of the binary’s state thousands of years in the past. If the binary is inspiraling ( $df/dt > 0$ ), the frequency imprinted on the Pulsar term,  $f_P$ , will be lower than the frequency observed at the Earth term,  $f_E$ . For a circular inspiral, the two are related by [55]:

$$(76) \quad \omega(t_p) = \omega_0 \left[ 1 - \frac{256}{5} \mathcal{M}^{5/3} \omega_0^{8/3} (1 + \hat{\Omega} \cdot \hat{p}) \frac{L}{c} \right]^{-3/8},$$

where  $\omega_0$  is the Earth-term angular frequency.

For nearby, massive binaries, the frequency difference  $\Delta f = f_E - f_P$  may be measurable. This allows PTAs to function as a dynamical time machine: by comparing the signal at the Earth and the pulsar, we can directly measure the binary’s evolution over millennial timescales [54, 55]. This measurement breaks degeneracies between the chirp mass  $\mathcal{M}$  and the luminosity distance  $D_L$  that are otherwise coupled in the Earth-term-only signal.

Beyond measuring the inspiral rate, Mingarelli et al. [55] showed that the pulsar term encodes higher-order post-Newtonian (pN) corrections to the orbital phase, enabling measurements of SMBHB spins. In particular, the spin-orbit (1.5pN) and spin-spin (2pN) coupling terms modify the phase evolution between the Earth and pulsar terms, so that the frequency difference  $\Delta f$  depends not only on  $\mathcal{M}$  but also on the individual spin magnitudes and orientations. With sufficient pulsar distance precision, PTAs can therefore test the pN expansion up to 2pN order through a direct comparison of the waveform at each pulsar and the Earth. However, extracting this physics requires knowing the pulsar distance  $L_a$  to high precision.

Indeed, whether the pulsar term is a signal or noise depends on the distance precision relative to the GW wavelength  $\lambda_{\text{gw}} = c/f$ . If the distance uncertainty  $\delta L_a \gtrsim \lambda_{\text{gw}}$ , the pulsar-term phase is effectively unconstrained and must be marginalized over. In this regime—which describes most current PTA pulsars at nanoHertz frequencies—the Earth term alone provides robust constraints on the GW frequency and total mass, while being orders of magnitude cheaper computationally [202]. Conversely, when  $\delta L_a \ll \lambda_{\text{gw}}$ , the pulsar term can be modeled coherently: Corbin & Cornish [54] showed that including it roughly doubles the effective signal power, while Lee et al. [203] demonstrated via Fisher matrix analysis that it is essential for accurate sky localization at high S/N, and can even be used in reverse to improve pulsar distance measurements from a strong CW detection. In a future PTA with precise distances for a subset of the array (see sect. 6.12), a hybrid

strategy may be useful: use the Earth term to drive detection and define the spatial correlation pattern (sect. 6.7), while selectively exploiting pulsar terms where distance precision is better than the detected GW wavelength (sect. 7).

**6.12. Pulsar Distances.** – To utilize the pulsar term for astrophysics, we must know the pulsar distance  $L_a$  well enough that the accumulated phase uncertainty does not exceed one gravitational wave cycle:  $2\pi f \delta L_a/c < 1$ , i.e.  $\delta L_a < c/(2\pi f)$ . This criterion is therefore frequency-dependent: at  $f = 10$  nHz it requires  $\delta L_a \lesssim 1$  pc, but at picohertz frequencies the GW wavelength is so long that the constraint relaxes by orders of magnitude, and many pulsars already satisfy  $2\pi f L_a/c < 1$  (see sect. 11.1). Although  $\delta L_a \lesssim 1$  pc is often quoted as a blanket requirement, this applies specifically to the nanoHertz band.

Achieving parsec-level precision at nanoHertz frequencies is a major observational challenge. Traditional pulsar-timing parallax, which measures the annual modulation in arrival times due to the Earth’s orbit, is limited to nearby sources ( $\lesssim 1$  kpc) because the parallax signature scales as  $1/L$  and falls below the timing noise floor for more distant pulsars [204]. VLBI astrometry offers superior precision [205, 206] but is observationally expensive and limited to bright radio sources. Indirect methods, such as Dispersion Measure (DM) distances derived from Galactic electron density models (e.g., NE2001 [207] or YMW16 [208]), are available for all pulsars but suffer from systematic uncertainties of  $\sim 20 - 50\%$  [209]. The recently released NE2025 model [210] updates the Galactic free electron density using an expanded set of independent distance measurements and improved modeling of spiral structure, which should reduce DM-based distance uncertainties for some PTA pulsars.

In the *Gaia* era, new approaches are opening possibilities. Jennings et al. [211] used *Gaia* DR2 parallaxes of binary pulsar companions to obtain independent distance measurements. *Gaia* parallaxes can also be combined with radio timing to further refine the distance estimate, see Moran et al. [209]. Improving these distance measurements is a priority for the field, as it directly enhances the sensitivity of PTAs to CW sources and enables tests of GR that rely on the distance-dependent Shklovskii effect [212, 213].

## 7. – The Angular Resolution of PTAs

A recurring question in PTA science is how the angular resolution of a PTA scales with the number of pulsars  $N$ . Much of the confusion in the literature stems from conflating three distinct quantities: the detection S/N (which scales with the number of pulsar pairs), the number of simultaneously resolvable point sources, and the angular pixel size of a sky map. A further distinction, discussed in sect. 7.3, is between resolution (separating two sources) and localization (pinpointing one source), which can differ by orders of magnitude. Recent theoretical work has clarified these regimes, and we summarize them here.

**7.1. The Incoherent Regime.** – In a standard PTA, pulsar distances are not known to within a GW wavelength ( $\lambda_{\text{GW}} = c/f \sim 1$  pc at 10 nHz). The pulsar term therefore cannot be phased coherently and averages to noise, so the array relies solely on the Earth term for sky localization.

In this regime, adding pulsars improves two things at different rates. The number of CW sources that can be simultaneously resolved scales linearly with  $N$ : Boyle & Pen [214] showed that the  $2N$  independent constraints from the Earth term (two polarizations

per pulsar) support at most  $M_{\text{sources}} \approx (2/7)N$  binaries, given that each requires  $\sim 7$  parameters. This was confirmed numerically by Babak & Sesana [215], who found  $M \approx N/3$  before GWB noise limited the fit.

The angular resolution—the pixel size of a reconstructed sky map—does not scale with  $N$  in the same way. Jow et al. [153] proved that an Earth-term-only array possesses only  $\approx 32$  independent angular modes (16 pixels  $\times$  2 polarizations), corresponding to a resolution of  $\approx 58^\circ$ , regardless of how many pulsars are in the array. This limit is reached once  $N \gtrsim 20$ ; adding further pulsars improves the S/N per pixel but does not make the pixels smaller.

The saturation at  $N \approx 20$  was in fact anticipated by Sesana & Vecchio [216], who used a Fisher matrix analysis to show that the parameter estimation accuracy for a single CW source—including the sky localization error box  $\Delta\Omega$ —ceases to improve beyond  $\approx 20$  pulsars at fixed total S/N (see their Table I). The two results arise from the same underlying cause: the finite number of independent Earth-term angular modes. However, they address different questions. Sesana & Vecchio quantify how well a single known source can be localized, finding  $\Delta\Omega \approx 40 \text{ deg}^2$  for 100 pulsars at S/N = 10. Jow et al. ask how many distinct sources a sky map can simultaneously resolve, and further extend the analysis to polarization. Both conclude that the spatial information content of the Earth term is exhausted at  $N \sim 20$ ; beyond that, more pulsars buy sensitivity but not resolution.

The frequently cited  $N^2$  scaling refers to the detection sensitivity, not the angular resolution. The Optimal Statistic exploits cross-correlations between the  $N(N-1)/2$  pulsar pairs. Siemens et al. [217] showed that  $\rho \propto N$  across the weak, intermediate, and strong-signal regimes. More pulsars also provide denser sampling of the Hellings–Downs curve, or any ORF. None of this improves the angular pixel size, which is bounded by the  $\approx 32$  Earth-term modes regardless of  $N$  [153].

**7.2. The Coherent Regime.** – The incoherent limit can be broken if pulsar distances are measured to sufficient precision—for example, via VLBI parallax [206] or orbital kinematic measurements (see sect. 6.12). With well-constrained distances the pulsar term can be phased, and the array functions as a true interferometer with a Galactic-scale baseline  $D_{\text{array}} \sim \text{kpc}$ .

Tsai et al. [218] recently showed that, in this coherent regime, the angular resolution transitions to the diffraction limit:

$$(77) \quad \delta\theta_{\text{diff}} \approx \frac{1}{\text{S/N}} \frac{\lambda_{\text{GW}}}{D_{\text{array}}}.$$

The improvement depends sharply on the number of pulsars with precise distance measurements,  $N_{\text{dist}}$ . Each distance-constrained pulsar adds an independent constraint on the source direction, so the angular resolution improves as

$$(78) \quad \delta\theta \propto \left( \frac{1}{\text{S/N}} \right)^{N_{\text{dist}}/2}.$$

With as few as  $N_{\text{dist}} \approx 9$  distance-calibrated pulsars at S/N = 10, sub-arcminute localization becomes achievable, which is sufficient to identify electromagnetic counterparts of individual CW sources [218]. This result underscores the importance of ongoing pulsar astrometry programs (sect. 6.12) for PTA science.

**7.3. Implications for Searches.** – These resolution limits have direct consequences for search pipeline design. For GWB anisotropy searches (sect. 5), the sky power is decomposed into spherical harmonics  $Y_{\ell m}$ , and a central question is the maximum recoverable multipole  $\ell_{\max}$ . A PTA with  $N$  pulsars provides  $N(N-1)/2$  independent cross-correlations, which constrain the angular power spectrum coefficients  $a_{\ell m}$  [56, 59]. The number of recoverable coefficients is limited by the rank of the response matrix [59, 219]:

$$(79) \quad (\ell_{\max} + 1)^2 \lesssim \frac{N(N-1)}{2} \quad \implies \quad \ell_{\max} \sim N.$$

For CW searches, it is essential to distinguish resolution (the minimum angular separation at which two sources can be told apart) from localization (how precisely a single source can be pinpointed). Although the fundamental pixel size is coarse ( $\sim 60^\circ$ ), a single bright binary can be localized to much higher precision, just as a star on a CCD can be centroided to sub-pixel accuracy. Goldstein et al. [220] showed via Bayesian analysis that the localization area scales as  $\Delta\Omega \propto \rho^{-2}$ :

$$(80) \quad \Delta\Omega \propto \frac{1}{\rho^2},$$

so that a high-S/N source can be localized to  $< 10 \text{ deg}^2$ . However, Tsai et al. [218] showed that this localization eventually hits a floor set by the pulsar-distance uncertainty. In the coherent regime, this floor is removed and  $\Delta\Omega$  continues to shrink toward the diffraction limit.

In fact, localization is also highly non-uniform across the sky. Petrov et al. [221] computed sensitivity sky maps for realistic PTA configurations, showing that the ability to localize a source degrades by orders of magnitude in regions of sparse pulsar coverage compared to the PTA’s best-constrained sky locations.

## 8. – Search for New Physics

While the astrophysical population of SMBHBs provides a natural explanation for the nanoHertz GWB, PTAs also serve as a unique probe of the very early Universe. In the era between inflation and Big Bang Nucleosynthesis ( $t \sim 10^{-32}$  s to 1 s), the Universe may have undergone violent processes that generated substantial gravitational radiation. The horizon size at these epochs corresponds to nanoHertz frequencies today, giving PTAs a direct window into high-energy physics at energy scales ( $T \sim 1 \text{ MeV} - 1 \text{ GeV}$ ) inaccessible to terrestrial colliders.

Distinguishing these cosmological signals from the astrophysical foreground relies fundamentally on their spectral shapes and angular power distribution. While circular SMBHBs produce a power-law spectrum with a characteristic strain  $h_c(f) \propto f^{-2/3}$  (spectral index  $\gamma = 13/3$ ; eq. (30)), cosmological sources often predict distinct spectral slopes, broken power laws, or peaked spectra [26].

*Cosmic Strings.* – Cosmic strings are one of the most compelling candidates for a cosmological GWB. These one-dimensional topological defects can form during symmetry-breaking phase transitions in the early Universe (e.g., at the Grand Unification scale). As the string network evolves, it forms closed loops that oscillate and decay via gravitational radiation.

The resulting GWB spectrum depends on the string tension,  $G\mu$ , and the loop production efficiency. Unlike SMBHBs, cosmic string spectra are typically flatter ( $\gamma < 13/3$ ) or possess a spectral break in the PTA band. Current PTA limits on the string tension are stringent; for stable Nambu-Goto strings, the non-detection of a specific spectral shape constrains  $G\mu \lesssim 10^{-10}$  [222, 223]. If the observed common red noise is interpreted entirely as a cosmic string signal, it favors a tension of  $G\mu \in [10^{-11}, 10^{-10}]$ , a range relevant for models of inflation embedded in string theory or identifying metastable defects from lower-energy phase transitions [26].

*Cosmological Phase Transitions.* – The early Universe may have experienced first-order phase transitions (FOPTs) as it cooled. In a FOPT, bubbles of the new vacuum state nucleate, expand, and collide. This process generates GWs through three dominant mechanisms: (1) the collision of bubble walls, (2) sound waves generated in the primordial plasma, and (3) subsequent magnetohydrodynamic (MHD) turbulence [224, 225].

The peak frequency of the resulting GW spectrum is determined by the temperature of the Universe at the time of the transition,  $T_*$ . For PTAs, the sensitive band of 1–100 nHz corresponds to transitions occurring at the Quantum Chromodynamics (QCD) scale ( $T_* \sim 100$  MeV) or in a hidden “Dark Sector” at similar energies [226]. Recent proposals, such as a “Dark Big Bang,” suggest that dark matter could have been generated in a separate phase transition, producing a detectable GWB signal without disturbing standard nucleosynthesis [227].

*Primordial Gravitational Waves and Inflation.* – Standard slow-roll inflation predicts a background of primordial GWs (PGWs) with a red-tilted spectrum (tensor spectral index  $n_T < 0$ ), which would be unobservably faint at nanoHertz frequencies. However, a detection by PTAs would be transformative, implying non-standard inflationary physics.

Scenarios capable of boosting the signal to PTA sensitivities include “blue-tilted” inflation ( $n_T > 0$ ) [228], particle production during reheating [229], or second-order GWs induced by large scalar perturbations [230]. The latter mechanism is particularly intriguing as it connects the GWB to the formation of Primordial Black Holes (PBHs). If the GWB is sourced by second-order effects, the amplitude observed by PTAs could imply a significant population of sub-solar mass PBHs, potentially constituting a fraction of the dark matter [222].

*Ultralight Dark Matter.* – PTAs also function as direct detectors for local dark matter. Ultralight Dark Matter (ULDM), composed of scalar or vector bosons with masses  $m \sim 10^{-23}$  eV, behaves as a coherent wave on galactic scales. This oscillating field interacts with standard matter via gravity, inducing periodic fluctuations in the gravitational potential of the Milky Way and the spacetime metric itself. The theoretical framework for detecting this signal with pulsar timing was established by Khmelnsky & Rubakov [231], who showed that an oscillating scalar field produces a monochromatic timing residual at a frequency set by the particle mass ( $f \approx 2m/h$ ). Porayko & Postnov [232] derived the first constraints using existing pulsar data.

Unlike the stochastic GWB (sect. 2), a ULDM signal is deterministic and monochromatic, with no quadrupolar spatial structure, making it distinct from the red-noise processes characteristic of the GWB and CWs. Porayko et al. [233] placed the first PTA-based upper limits using the PPTA, and Battye et al. [234] extended these searches to time-dependent axion dark matter signals. Multiple PTAs have now carried out independent ULDM searches: NANOGrav using their 15-yr dataset [26] and the EPTA in

their second data release [235]. None have found evidence for ULDM, but together they place competitive constraints on the local dark matter density across the mass range  $m \sim 10^{-24}$ – $10^{-22}$  eV. The PPTA DR3 has pursued a complementary approach, using pulsar polarization data to search for axion-like dark matter via the cosmic birefringence effect [236].

*Tests of General Relativity and Alternative Polarizations.* – Beyond searching for exotic sources, PTAs offer a precision laboratory for testing the fundamental nature of gravity itself. General Relativity (GR) predicts that GWs possess only two tensor polarization modes: plus (+) and cross ( $\times$ ), which propagate at the speed of light. These modes generate the specific quadrupolar spatial correlation pattern described by the Hellings–Downs curve ( $\Gamma_{ab}^{\text{HD}}$ ; sect. 2.2, eq. (25), fig. 4).

However, many extensions to GR—such as scalar-tensor theories,  $f(R)$  gravity, or massive gravity—predict the existence of up to four additional polarization modes: two scalar modes and two vector modes [73, 237]. Each produces a distinct spatial correlation pattern. The scalar breathing mode (spin-0, transverse) has  $\Gamma_{ab}^{\text{ST}} = \frac{1}{4}(3 + \cos \zeta)$ , which is unity for co-located pulsars and remains positive ( $\frac{1}{2}$ ) even at  $\zeta = 180^\circ$  [237]. Unlike the tensor and breathing modes, whose ORFs depend only on the angular separation  $\zeta$ , the scalar longitudinal and vector mode ORFs remain frequency-dependent, scaling with the product  $fL$  where  $L$  is the pulsar distance [237]. This frequency dependence arises because the pulsar terms (sect. 6.11) do not average out for non-transverse polarizations as they do for the tensor modes. The scalar longitudinal mode (spin-0) produces a correlation that is approximately monopolar and can reach values orders of magnitude larger than the transverse modes for nearby pulsar pairs. In standard PTA analyses, a monopolar contribution to the cross-correlations is absorbed by the fit for a common clock correction, so a longitudinal-mode GWB would be indistinguishable from a clock error unless the analysis is specifically designed to separate them. The two vector (spin-1) modes likewise have frequency-dependent ORFs whose values grow for nearly co-aligned pulsars; their correlation pattern can be degenerate with Solar System ephemeris errors [238].

By decomposing the observed spatial correlations (sect. 2.2) into these tensor, scalar, and vector basis functions, PTAs can place stringent upper limits on the amplitude of non-Einsteinian modes [73, 237]. Current datasets remain consistent with pure GR, with Bayes factors disfavoring the presence of significant scalar or vector components [26].

Crucially, the search for these alternative polarizations is deeply intertwined with the search for anisotropy (sect. 5). A deviation from the standard Hellings–Downs curve could arise either from non-GR physics (e.g., a scalar background) *or* from a breakdown of isotropy (e.g., a clustered astrophysical background). Disentangling these effects requires a generalized map-making approach (sect. 5.1.3) that simultaneously reconstructs the angular power spectrum for all possible polarization modes. While computationally demanding, this joint analysis will be essential for the SKAO era to rigorously confirm that the detected signal is indeed the quadrupolar, isotropic background predicted by Einstein.

## 9. – Pulsar Noise Models

The inherent timing stability of millisecond pulsars and the ability to cross-correlate signals between pulsars (sect. 2) is tantamount for PTAs to detect GW signals [239]. However, the success of PTA experiments is also inherently tied to the challenges posed

by various noise processes. Sources of pulsar noise can originate from intrinsic processes at the pulsar itself, propagation effects through the interstellar medium (ISM), or clock errors and solar system ephemeris errors [31, 63, 240].

The impacts of noise on a GW analysis can be understood in terms of sensitivity curves [31, 241]. GW searches using PTAs are fundamentally limited at certain frequencies due to degeneracies with certain physical effects, which are accounted for by a deterministic timing model for each pulsar. For example, fits for the spindown of a pulsar resulting from by magnetic dipole radiation act as a quadratic high-pass filter, while fits for each pulsar’s precise sky location remove power at frequencies of 1/yr due to the Earth’s orbit. Unresolved stochastic “red” and “white” noise in each pulsar further limits sensitivity at low and high frequencies, respectively. Intrinsic pulsar red noise fundamentally limits sensitivity to low-frequency signals, such as from a GWB (sect. 2), while white noise is the dominant limitation at higher frequencies, where PTAs are more likely to resolve individual CW sources (sect. 6).

In practice, accurate noise modeling is a deep and complicated endeavor which introduces many challenges for GW measurements. The properties of any noise process may vary considerably from one pulsar to another [32, 242–244], and seemingly subtle noise modeling decisions have in fact played crucial roles in GW analyses. For example, failing to account for unmodeled noise in certain pulsars was found to bias GWB parameter estimation in a time-slicing analysis of the NANOGrav 11 yr data set [245]. It is also challenging to characterize pulsar noise without biasing the GW analyses. For instance, the past use of uniform priors on the amplitude of the intrinsic red noise in individual pulsars has been shown to result in overly low GWB amplitudes and upper limits [79]. Meanwhile, the failure to account for ensemble properties of intrinsic red noise across millisecond pulsars has been shown to result in spurious detections of GWB-like signals [18, 80, 246–248]. These challenges ultimately introduce an opportunity, as improvements to pulsar noise analysis and mitigation is a promising means to improve PTA sensitivity to GWs [31]. Furthermore, better characterization of pulsar noise can provide valuable scientific insights on the underlying astrophysics, such as ISM turbulence [249] and variations in the solar wind density [250, 251]. This dual-purpose analysis broadens the scope of pulsar noise analysis efforts beyond GW detection.

Of the types of noise sources affecting pulsar timing, perhaps the richest and most diverse are “chromatic,” meaning the magnitude of the timing delay depends on the radio frequency dependent [240, 244, 252]. Chromatic effects typically arise due to ISM propagation effects, and they must be mitigated by observing TOAs at several radio frequencies [253, 254]. However, multiple factors make the complete removal of chromatic noise difficult. These include the finite range and resolution of radio frequency coverage [255, 256] and the potential of mismodeling either the radio-frequency dependence or time-dependence of the chromatic delay [32, 253, 257].

Here we highlight DM and scattering variations as two prominent sources of chromatic noise. DM variations are changes in the integrated electron density content of the ISM and the solar wind along the line of sight. These are observed in nearly all pulsars and the time delay  $\Delta t$  from DM depends on radio frequency  $\nu$  as  $\Delta t \propto \nu^{-2}$ . [249, 258, 259]. DM variations can either be fit using a piecewise constant model [260], modeled as a Gaussian Process [261, 262], or measured directly alongside the TOA using wideband timing methods [263, 264], each method coming with advantages and disadvantages [265]. For example, the overall impact of the piecewise constant fit for DM variations is a broadband reduction in GW sensitivity across low and high GW frequencies [241]. Gaussian process models for DM variations impose a smaller penalty on sensitivity as they produce

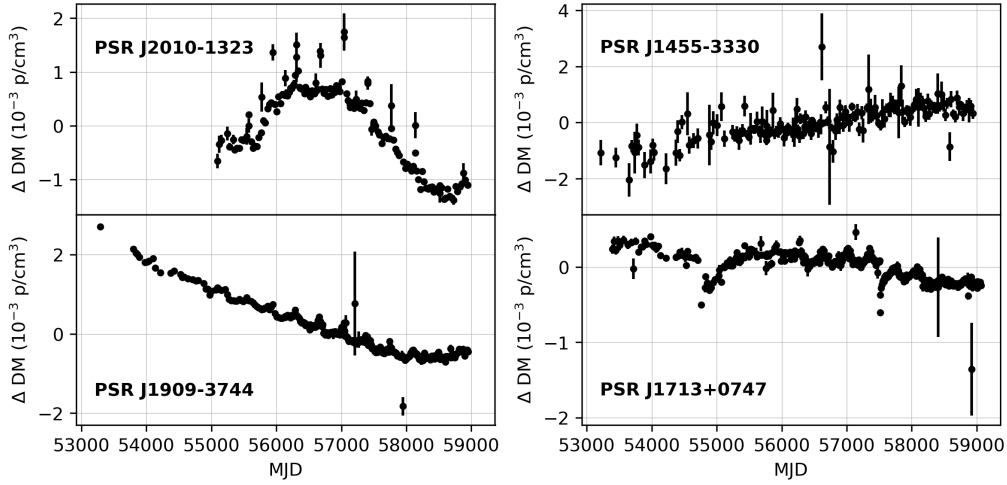


Fig. 16. – DM variations for four pulsars from the NANOGrav 15-yr data set [254]. DM variations can be linear, periodic, or stochastic, and may manifest very differently in different pulsars. DM cusps with annual periodicity originate from the solar wind. Mismodeled DM variations will propagate errors into the infinite-frequency TOA, reducing sensitivity to GWs.

more precise DM time series and occupy a much smaller prior volume in a Bayesian sense [265, 266], but they come with higher computational overhead and require accurate modeling for the time-dependent covariance of the variations. fig. 16 shows examples of DM time series from four pulsars from the NANOGrav 15-yr data set [254]. These showcase the variety and complexity of DM trends that may appear in different pulsars, which will propagate errors into the infinite-frequency TOA if imperfectly estimated [255]. In particular, the solar wind introduces quasi-periodic structures which are not well-modeled as Gaussian perturbations to the DM time series itself, instead requiring additional detailed models for the local solar wind electron density [250, 251, 267–269]. Importantly, the solar wind affects all pulsars viewed through the inner heliosphere, so solar wind-induced DM variations are correlated between pulsars at similar solar elongations, introducing a source of spatially correlated chromatic noise that must be distinguished from the GWB [63, 250].

We also note two sudden dips in the DM variations for PSR J1713+0747 in fig. 16. These highlight one of the bigger challenges for DM modeling and pulsar noise modeling in general, as these events are currently believed to be related either to intrinsic magnetospheric disturbances or complicated ISM phenomena such as plasma lensing, rather than a dispersive process [32, 270, 271]. However, since these events are intrinsically chromatic, they can be easily mismodeled as DM variations, at the cost of excess time-dependent noise that leaks into the achromatic noise channel [245, 257].

Time-variable scattering is another chromatic effect which results from frequency-dependent refraction and diffraction as the pulse propagates through inhomogeneities in the ISM [252, 272, 273]. While scattering is not expected to affect TOAs as strongly as DM variations, it is significantly more difficult to model, described mathematically as the convolution of the pulse profile with a pulse broadening function. The first order effect of scattering is to delay the TOA proportionally to the pulse broadening function,

which scales as  $\Delta t \propto \nu^{-4.4}$  for a Kolmogorov medium. However, a much broader range of chromatic dependencies may arise depending on the geometry of the ISM, the strength of the scattering, and the interplay between the pulse broadening function and the intrinsic pulse shape [31, 274, 275]. If scattering is not accounted for, it will be absorbed by the DM variations model, propagating time-and-DM-correlated errors into the achromatic delay and inflating the red and white noise levels [242, 257]. Gaussian processes have been used to partially correct for scattering using an appropriate covariance prior (which thereby reduces the degeneracy with DM variations) and a fixed prescription for the TOA scaling such as  $\Delta t \propto \nu^{-4}$  or  $\Delta t \propto \nu^{-\chi}$  with  $\chi$  as a free parameter [30, 32, 257, 271, 276], but this may still be insufficient for strongly scattered pulsars [269, 275, 277, 278]. A more promising technique for precise measurement and mitigation of the scattering delay is deconvolution of the pulse broadening function from the intrinsic pulse shape, see Young et al. [279], in particular using precise scintillation measurements from cyclic spectroscopy [280–282]. In practice, both methods will complement each other; cyclic spectroscopy applies best for the most highly scattered pulsars [281], whereas Gaussian processes should work better for weakly-scattered pulsars where the TOA shifts are more closely proportional to the scaling of the pulse broadening function [31, 275]. Beyond scattering, an inhomogeneous ISM may produce a variety of higher-order effects which are inextricably linked with scattering, including angle-of-arrival variations, refractive scintillation, diffractive scintillation, and frequency-dependent DM due to multipath propagation [31, 252, 278, 283, 284].

In contrast to chromatic noise, “achromatic” noise is not dependent on radio frequency. Achromatic noise can be caused by stochastic fluctuations in pulsar spindowns due to e.g., torques from the pulsar magnetosphere [285, 286], variable coupling between the neutron star crust and superfluid interior [287, 288], the presence of an asteroid belt [289, 290]. Mismodeled or unmodeled chromatic noise can arise as an achromatic noise process which can be mitigated [245, 255, 256, 269]. However, intrinsic sources of achromatic noise are less straightforward to mitigate, directly impacting GW sensitivity or potentially masquerading as a GW signal if the achromatic noise is present in enough pulsars [246, 248]. Thankfully, the value of PTAs lies in the ability to distinguish GW signals from achromatic noise, since GW signals are correlated between different pulsars, while any achromatic noise which originates from processes intrinsic to the pulsar will be uncorrelated between different pulsars. To illustrate, an example set of simulated pulsar timing residuals, decomposed into individual sources of chromatic and achromatic noise, is shown in fig. 17.

Overall, a rich phenomenology of achromatic and chromatic noise processes have been observed across PTA datasets and collaborations, with ever-increasing levels of comprehensiveness and model fidelity [30–33, 242–244, 257, 267–269, 291–293]. Focusing the present discussion on the NANOGrav 15-yr dataset, ref. [31] first performed a detailed analysis of the achromatic red noise (ARN) in the pulsars from the NANOGrav 15-yr dataset [254]. They found the pulsars could be grouped into three main categories: 1) pulsars with loud, shallow-spectral index ARN, 2) pulsars whose ARN disappears when modeling the GWB, and 3) pulsars where ARN was not detected (fig. 18, left side). The one outlier is PSR B1937+21, which exhibits a loud red noise process with a steep spectral index (fig. 18, right side). Ref. [31] suggest that for the pulsars in group 1, the majority of ARN likely results from mismodeled chromatic noise. Meanwhile, the dominant source of ARN in group 2 appears to be the GWB. Additionally, [31] found no significant evidence of excess noise on top of a power law red noise spectrum for all pulsars in the NANOGrav 15-yr data set.

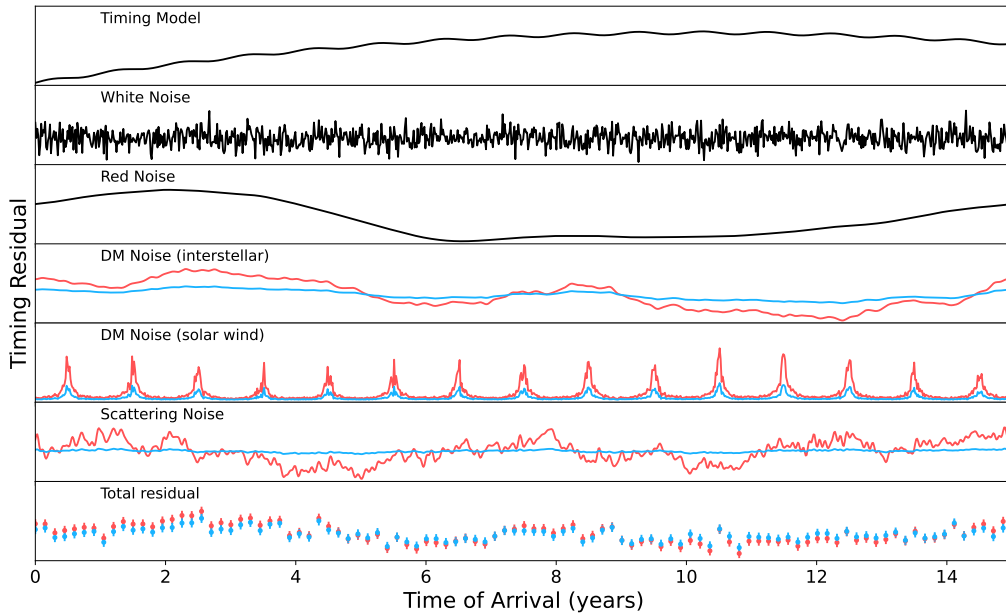


Fig. 17. – Simulated timing residuals as produced by different types of sources of noise. The top three panels show example contributions to a pulsar’s achromatic noise budget. First, a quadratic plus annual sinusoidal trend arising from perturbations to a simple timing model, white (time-uncorrelated) noise, and red (time-correlated) noise. The next three panels show examples of chromatic noise, in which the delay is larger for TOAs measured at lower radio frequency (shown in red) than a higher radio frequency (blue). In order we have stochastic DM variations from the interstellar medium, annually-modulated DM variations from the solar wind, and scattering variations which have a different radio-frequency dependence than DM. The total timing residuals are shown in the bottom panel, including the sum of all noise sources and a finite cadence of observations. The simulated residuals in this example assume each type of noise is described by a Gaussian process.

A more recent custom noise model analysis of the NANOGrav 15-yr dataset [269], in which detailed chromatic models are specified for each pulsar as driven by each pulsar’s dataset, provides striking confirmation and refinement of this picture. By replacing the standard DMX (piecewise-constant DM) model with customized chromatic noise models, the analysis found significant changes to the achromatic red noise in 19 of 67 pulsars. The results illuminate each of the three ARN categories identified by [31]. Among the 12 pulsars dominated by intrinsic red noise (IRN), five lost their ARN detection entirely (PSRs B1953+29, J1747–4036, J1802–2124, J1946+3417, and J2145–0750), confirming that their apparent “red noise” was in fact mismodeled chromatic noise arising due to non-dispersive effects. Among the 13 pulsars dominated by common red noise (CRN), four lost their ARN detection (PSRs J0437–4715, J1600–3053, J1738+0333, and J1744–3744), while PSR J1713+0747—one of the most precisely timed pulsars in the array—showed the largest shift, with  $\log_{10} A_{\text{RN}} = -14.7 \pm 0.4$  and  $\gamma_{\text{RN}} = 3.7 \pm 1.2$  under the custom noise model, compared to a higher amplitude and lower spectral index under DMX. This shift is driven by the explicit modeling of the two chromatic events (at MJDs 54758 and 57509) that had previously leaked power into the achromatic red noise spec-

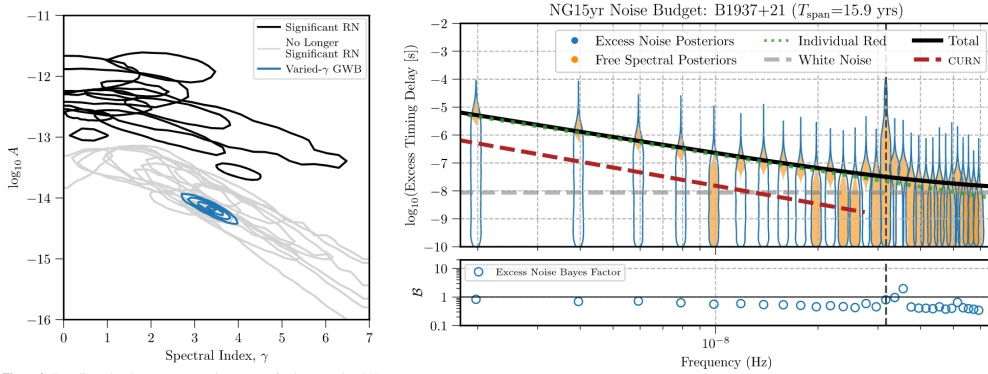


Fig. 18. – *Left*: The distribution of red noise parameters in the NANOGrav 15-yr data set [254]. Two dominant groups are displayed: one with loud, low spectral index ARN (black), and one whose values are more spectrally-consistent with the GWB (grey). The latter group is noticeably offset from the former and becomes insignificant in the presence of the GWB signal, implying the noise in these pulsars is indeed dominated by the GWB, whose parameters are in blue. *Right*: The noise budget of PSR B1937+21, including contributions from red noise, white noise, and the GWB without Hellings-Downs correlations (CURN). PSR B1937+21 is an exceptional millisecond pulsar with very loud and steep spin noise, and this is clear from its ARN spectrum, which is well above the GWB. Figures from [31].

trum and the DM variations (fig. 16). Among 42 more white-noise-dominated pulsars, five newly detected ARN (PSRs J0023+0923, J0636+5128, J1455–3330, J1944+0907, and J2043+1711), indicating that the standard noise model had been too rigid to reveal underlying low-level red processes. Furthermore, 24 of the 37 pulsars without ARN detections showed reduced 95% upper limits on the red noise amplitude, reflecting the improved noise separation. The custom noise model analysis [269] also found notable changes to the white noise parameters under customized chromatic models.

There are a few exceptional cases in which achromatic noise can still be correlated between pulsars. Errors in terrestrial/observatory time standards (“clock errors”), and errors in the solar system ephemerides (used to transform ToAs to the solar system barycenter), or errors in solar wind modeling may also introduce correlated noise between all pulsar pairs [63]. However, a GWB can still be distinguished from these sources by its ORF (sect. 2.2). Between pulsar pairs, clock errors introduce monopolar correlations, and ephemeris errors introduce dipolar correlations, whereas a GWB is uniquely characterized by Hellings–Downs correlations (eq. (25); [6]). Monopolar and dipolar correlations are measured to be far weaker than Hellings–Downs correlations in current PTA datasets [21].

Finally, choices in noise modeling continue to have strong bearing on current GW inferences. fig. 19 shows various examples of how different noise modeling choices impact inferred GWB properties across independent PTA datasets: EPTA DR2 [81, 294], the NANOGrav 15-yr dataset [21, 254], and PPTA DR3 [267, 295]. While the detailed prescriptions behind the noise models and the nature of the comparison differs for each of these analyses, the common link is that a deeper refinement of the pulsar noise models impacts the spectral characterization of the GWB. One may notice the commonality that refined noise modeling tends to drives the characterization towards lower amplitudes, and towards the steeper spectral index  $\gamma = 13/3$  predicted for SMBHBs; this naturally arises

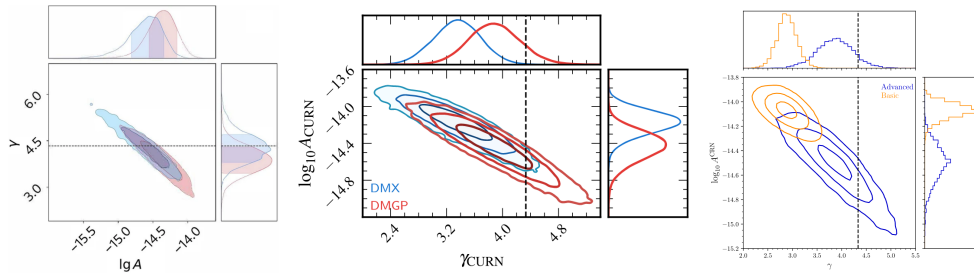


Fig. 19. – How GWB spectral parameter inferences are affected under different noise modeling assumptions, for three different datasets. *Left:* For EPTA DR2 [294], the inclusion of hierarchical priors and additional white noise models (blue) produce lower amplitude and higher spectral index GWB measurements than the original use of only achromatic and chromatic analysis (red) [81]. *Middle:* For the NANOGrav 15-yr dataset [254], a piecewise-constant DM variations model (blue) and a DM Gaussian process model with a power-law spectrum (red) also produce differences between recovered GWB parameters, with increased consistency with  $\gamma_{\text{GWB}} = 13/3$  using the Gaussian process model [21]. *Right:* For PPTA DR3 [295], a set of standard noise models (orange) and customized noise models (blue) result in stark differences between recovered GWB properties, again with the custom noise models favoring a steeper GWB spectrum much more consistent with  $\gamma_{\text{GWB}} = 13/3$  [267]. Figures from [21, 81, 267].

as many of the most difficult sources of noise to model are chromatic and produce errors with whiter spectra than low frequency GWs, leaking broadband power into GWB measurements. However, there is nothing intrinsic in these analyses that suggest the GWB should be closer to  $\gamma = 13/3$ , since noise pulsars are typically prescribed on the single pulsar level. Overall, it is clear that pulsar noise characterization impacts the inferred power spectrum of the GWB (eq. (30)), which ultimately impact understanding about the source of the GWB, as the GWB power spectrum is used to fit various SMBHB population parameters [34] and used to test different hypotheses about the GWB’s source [26]. This observations motivate continued, rigorous development of more accurate pulsar noise models. Sophisticated noise modeling approaches will only become more important for future prospects to identify individual binary sources of nanoHertz GWs (sect. 6). As discussed in sect. 3, the development of custom noise models has already shifted the inferred GWB spectral index toward the  $\gamma = 13/3$  predicted for circular SMBHBs (eq. (30)), underscoring the tight coupling between noise characterization and astrophysical interpretation.

## 10. – The International Pulsar Timing Array

The IPTA was established in 2010 [16] to combine the datasets of the regional PTAs into a single array. Beyond GW searches, the IPTA has pursued a broad science program, including constructing a pulsar-based timescale [296] and constraining Solar system ephemerides and planetary masses, including limits on the mass of Ceres and a hypothetical Planet 9 [238, 297].

An important early effort was the IPTA Mock Data Challenge (MDC) program, which provided standardized simulated datasets to benchmark and cross-validate the analysis pipelines developed independently by each regional PTA. The first MDC [298–300] tested the recovery of injected GWB and CW signals in realistic timing data, reveal-

TABLE III. –  $S/N$  scaling laws for each PTA signal class. Here  $N$  is the number of pulsars,  $T_{\text{obs}}$  is the observing timespan,  $\sigma_{\text{TOA}}$  the timing precision, and  $c$  the observing cadence. The  $\text{GWB}$  scaling assumes  $\gamma = 13/3$ . The three  $\text{GWB}$  regimes differ only in the  $T_{\text{obs}}$  exponent; the  $\text{GWB}$  scaling with  $N$  is linear across all regimes [217].  $\text{CW}$  scalings are from [164, 306];  $\text{BWM}$  from [307, 308].

Signal class	S/N ( $\rho$ )	References
GWB (weak signal)	$N T_{\text{obs}} (c/\sigma_{\text{TOA}}^2)^{3/13}$	[217]
GWB (intermediate)	$N T_{\text{obs}}^{5/13} (c/\sigma_{\text{TOA}}^2)^{3/13}$	[217]
GWB (strong signal)	$N T_{\text{obs}}^{3/13} (c/\sigma_{\text{TOA}}^2)^{3/13}$	[217]
CW (individual SMBHB)	$(N T_{\text{obs}} c/\sigma_{\text{TOA}}^2)^{1/2}$	[164, 306]
BWM (burst with memory)	$N^{1/2} T_{\text{obs}}^{3/2} (c/\sigma_{\text{TOA}}^2)^{1/2}$	[307, 308]

ing significant differences in how groups handled noise estimation and signal extraction. The second MDC [301, 302] introduced more complex scenarios, including non-Gaussian noise and multiple simultaneous signals. These exercises were instrumental in building confidence that the diverse software pipelines across the collaboration would yield consistent results when applied to real data—a prerequisite for the coordinated 2023 evidence announcements.

The IPTA’s first data release (DR1) [303] combined data from all three founding PTAs and placed a  $\text{GWB}$  upper limit, with noise characterization by Lentati et al. [242]. The second data release (DR2) [304] expanded the array to 65 pulsars with baselines up to 30 years, and was followed by a  $\text{GWB}$  search [20] and a  $\text{CW}$  search [176]. In anticipation of a detection, the IPTA Detection Committee established a formal checklist of validation criteria [29] that informed the interpretation of the 2023 regional results, which were subsequently compared in a joint analysis [305].

A persistent challenge for the IPTA is the long timescale of full data combination. Aligning time standards, harmonizing backend offsets, and fitting consistent noise models (sect. 9) across heterogeneous datasets is labor-intensive, causing IPTA releases to lag years behind the regional state of the art. However,  $\text{GWB}$  sensitivity scales with the number of pulsar pairs, and measurements of the full Hellings–Downs curve (sect. 2),  $\text{GWB}$  anisotropy (sect. 5), and individually resolvable  $\text{CW}$  sources (sect. 6) all benefit from a larger, globally distributed array. Several recent methods address the combination bottleneck, but first we summarize the quantitative scaling.

**10.1. The Need for Data Combination: Scaling Laws.** – The sensitivity of a PTA depends on the number of pulsars  $N$ , the observing timespan  $T_{\text{obs}}$ , the timing precision  $\sigma_{\text{TOA}}$ , and the observing cadence  $c$  (or equivalently the mean interval  $\Delta t = 1/c$ ). Tab. III collects the scaling relations for each signal class; we summarize the key points below.

For the  $\text{GWB}$ ,  $\rho \propto N$  across all three signal regimes [217]; what changes between regimes is the dependence on  $T_{\text{obs}}$  (tab. III). In the weak-signal limit  $\rho \propto T_{\text{obs}}$ , in the intermediate regime  $\rho \propto T_{\text{obs}}^{5/13}$ , and in the strong-signal limit  $\rho \propto T_{\text{obs}}^{3/13}$ . The per-pulsar dependence on  $c/\sigma_{\text{TOA}}^2$  enters with a shallow  $3/13$  exponent for the  $\text{GWB}$ , so the most efficient path to stronger  $\text{GWB}$  constraints is adding well-timed pulsars. By

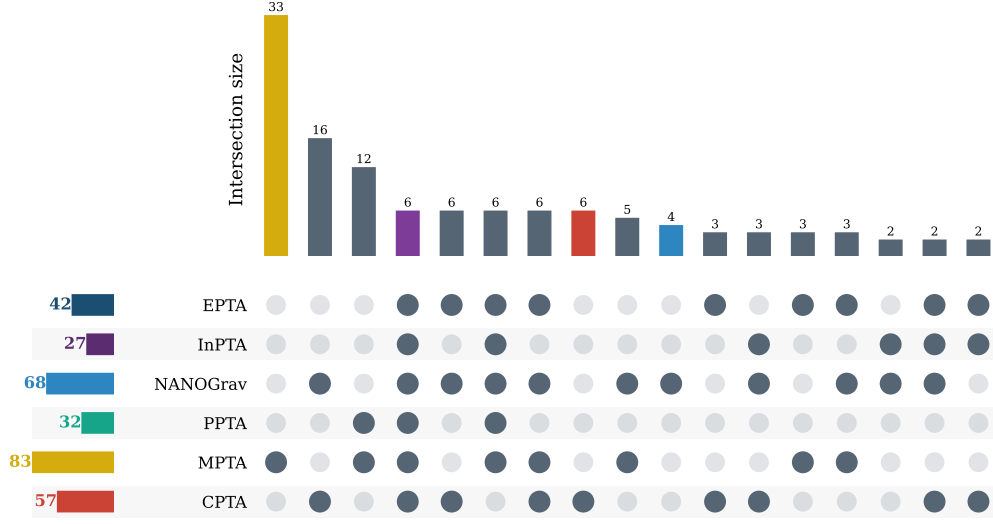


Fig. 20. – UpSet plot showing the overlap of pulsars currently being timed by regional PTAs contributing to the IPTA, based on each array’s most extensive data release. For EPTA, this is Desvignes et al. (2016) [309], not EPTA DR2. These pulsars have not necessarily been selected for IPTA DR3, which will be defined by its own selection criteria. Each column corresponds to pulsars timed by exactly the combination of PTAs indicated by the filled circles below; the bar height gives the count. Horizontal bars on the left show each PTA’s total. The 13 intersections containing a single pulsar are listed in tab. IV.

contrast, CW and BWM sensitivities scale as  $(c/\sigma_{\text{TOA}}^2)^{1/2}$ , so investments in wideband timing [253, 263, 264, 310–315], which lowers  $\sigma_{\text{TOA}}$  by averaging over broader frequency coverage and better constraining DM variations, or increased cadence have a stronger effect on the S/N. The BWM scaling carries an additional  $T_{\text{obs}}^{3/2}$  factor, making long uninterrupted baselines critical for memory searches.

Combining datasets across PTAs improves all of these quantities: it increases  $N$ , extends  $T_{\text{obs}}$ , and for pulsars observed by multiple PTAs, this increases the effective cadence  $c$  and broadens the radio frequency coverage, which improves noise characterization, and thereby lowers the effective  $\sigma_{\text{TOA}}$ .

For GWB anisotropy, the intrinsic shot-noise signal grows steeply with frequency,  $C_{\ell>0}/C_0 \propto f^{11/3}$  (eq. (56)), so the highest accessible frequency bins carry most of the anisotropy information. Accessing those bins requires high observing cadence, while detecting the underlying GWB with sufficient S/N to resolve angular structure requires  $T_{\text{obs}} \gtrsim 15$  yr [56]—a regime where the IPTA’s extended baselines provide a decisive advantage. More pulsars increase  $\ell_{\text{max}} \sim N$  (sect. 7.3), granting access to higher angular multipoles.

Beyond raw sensitivity, a global PTA provides qualitatively better sky coverage. Regional PTAs are limited by their telescope locations: NANOGrav covers primarily the northern sky, PPTA the south, and EPTA an intermediate band. The IPTA combines these into a nearly all-sky array. This is essential for CW searches because the antenna beam pattern  $F^A(\hat{\Omega}) \propto (1 + \hat{\Omega} \cdot \hat{p})^{-1}$  (sect. 2.2) depends on the angle between the pulsar direction  $\hat{p}$  and the GW propagation direction  $\hat{\Omega}$ : a CW source in a region of sky devoid

TABLE IV. – *Tabular companion to fig. 20. A filled circle indicates membership in that PTA. The upper part lists intersections containing two or more pulsars; the lower part lists the 13 single-occupant intersections by name. The six PTAs collectively time 131 unique pulsars. This does not define IPTA DR3, which will be determined by its own selection criteria.*

Count	Pulsar	EPTA	InPTA	NANOGrav	PPTA	MPTA	CPTA
33						•	
16				•			•
12					•	•	
6		•	•	•	•	•	•
6							•
6		•	•	•	•	•	
6		•		•		•	•
6		•		•			•
5				•		•	
4				•			
3		•		•		•	
3			•	•			•
3		•				•	
3		•					•
2		•	•	•			•
2			•	•			
2		•	•				•
1	J0437–4715		•	•	•	•	
1	J0614–3329			•	•	•	
1	J1455–3330	•	•	•		•	
1	J1614–2230		•	•		•	
1	J1741+1351			•	•		•
1	J1744–1134	•	•		•	•	•
1	J1824–2452A				•		
1	J1832–0836			•	•	•	•
1	J1857+0943	•	•	•	•		•
1	J1911–1114	•				•	•
1	J1939+2134	•	•	•	•		
1	J2150–0326					•	•
1	J2234+0944			•		•	•
<b>131</b>	<b>Total unique pulsars</b>						

of pulsars produces a weak response across the entire array, while a pulsar nearly aligned with a source maximizes the antenna response [56, 164]. Full-sky coverage also eliminates geometric blind spots for anisotropy searches, ensuring sensitivity to angular modes at all multipoles.

The degree of overlap between arrays is illustrated in the UpSet plot of fig. 20, with the full intersection data listed in tab. IV. An UpSet plot visualizes the membership of pulsars across multiple PTAs. Each column represents a specific combination of PTAs,

indicated by the filled circles in the lower matrix; the bar height above gives the number of pulsars timed by exactly that combination and no other. For instance, the tallest bar corresponds to the 33 pulsars observed only by the MPTA. The horizontal bars on the left show the total number of pulsars in each PTA regardless of overlap.

Reading the plot, the MPTA times 83 pulsars in total, but 33 are unique to that array. Of InPTA’s 27 pulsars, all are also observed by at least one other PTA—InPTA has no unique pulsars, and neither does the EPTA. Six pulsars are observed by all six PTAs (the column with all six circles filled). Only one pulsar is unique to the PPTA: J1824–2452A (PSR B1821–24A). This extensive overlap motivates the LITE framework’s figure-of-merit approach as a first step to data combination: rather than merging all available TOAs, one selects the highest quality dataset per pulsar.

**10’2. The LITE method: three steps to combination.** – Addressing this challenge, Larsen et al. [316] proposed the LITE method, a principled framework for rapid PTA data combination. Rather than attempting to merge all datasets in one step, LITE decomposes the process into three deliberate stages, each of which yields scientifically valuable intermediate products.

1. **Lite data sets.** At the first stage, for each pulsar observed by multiple PTAs, the single dataset with the highest figure of merit (FoM) is selected. The FoM is a scaling proxy for the expected S/N of a given GW signal (Tab. III). This step immediately yields a “best of” compilation: a global array assembled from the highest-quality data per pulsar, without the need for detailed cross-calibration.
2. **Early combined data sets (EDR).** The second stage prioritizes combination of the most sensitive pulsars, again ranked by their FoM. By combining the top-tier pulsars first, one can rapidly construct an intermediate dataset that already captures much of the total sensitivity. This staged approach mirrors the strategy of early data releases in other fields (e.g. Gaia), enabling preliminary science well before the full dataset is complete.
3. **Fully combined data sets.** Finally, the traditional endpoint is reached, where all available data are harmonized and combined. This stage remains essential for definitive analyses, but by the time it arrives, much science has already been extracted from the earlier stages.

There are several advantages to this step-by-step approach. It ensures that new PTA data can be rapidly incorporated into global analyses, reducing the time lag between data acquisition and astrophysical inference. It provides multiple checkpoints where results can be cross-validated across different stages, identifying biases or systematics early. And it allows flexibility: one can construct GWB-optimized Lite sets, CW-optimized Lite sets, or even burst-optimized sets, depending on the signal class of interest.

A key innovation of LITE is its reliance on FoMs to guide data selection. The per-pulsar FoMs for each signal class are collected in tab. III. Since the FoMs weight  $T_{\text{obs}}$ ,  $\sigma_{\text{TOA}}$ , and cadence  $c$  differently, the optimal Lite data set depends on the target signal. These metrics provide a quantitative basis for selecting among overlapping datasets.

Applying this framework to IPTA DR2, [316] showed that Lite sets recover the common red noise signal with amplitudes consistent with the fully combined dataset, albeit with somewhat broader posteriors. For example, DR2 Lite yielded a GWB amplitude of  $A \approx 4.8_{-1.8}^{+1.8} \times 10^{-15}$ , compared to  $A \approx 3.9_{-1.0}^{+1.0} \times 10^{-15}$  for the full DR2. The difference reflects Lite’s greater vulnerability to pulsar-intrinsic noise leaking into the common

channel, which we now know should be expected. Constraints on the spectral index are correspondingly weaker, but still consistent.

**10.3. *FrankenStat: likelihood-level data combination without merging TOAs.*** – A complementary approach avoids TOA-level merging entirely. FrankenStat [317] combines datasets at the likelihood level: for each pulsar observed by multiple PTAs, the individual-PTA likelihood functions are multiplied to form a “FrankenPulsar” object that can be dropped directly into standard Bayesian pipelines without modifying the analysis code. The procedure runs in minutes on a laptop, in contrast to the years typically required for full TOA harmonization.

In simulation studies, the FrankenStat and traditionally combined datasets yield nearly identical S/N distributions for a Hellings–Downs-correlated background (eq. (25)), with sensitivity curves differing at the  $\lesssim 1\%$  level when full noise models (sect. 9) are included [317]. FrankenStat does not replace fully harmonized IPTA releases, which remain essential for precision inference and careful treatment of cross-dataset systematics, but it provides a fast surrogate that enables routine cross-PTA checks and rapid iteration whenever a regional PTA updates a key pulsar or noise model.

**10.4. *Fourier-space combination and global Gibbs sampling.*** – A third strategy operates entirely in Fourier space. Valtolina & van Haasteren [318] proposed a regularized likelihood approach in which posterior distributions over Fourier coefficients are first obtained for each pulsar individually, then combined in a global GWB search. The per-pulsar stage absorbs the complexity of heterogeneous noise models and timing solutions, so the global stage can proceed without merging raw TOAs or reconciling backend-specific systematics. This approach naturally accommodates data from different observing methods—including gamma-ray pulsars. Complementing this, Laal et al. [319] developed a global Gibbs sampling scheme that jointly infers per-pulsar noise parameters and a common red process in a single hierarchical model, avoiding the need for fixed noise posteriors and enabling fully self-consistent inference across the array.

**10.5. *Outlook.*** – The trajectory from cross-PTA validation [305] to rapid combination methods captures a broader shift: the immediate priority has moved from establishing the existence of a common signal to precision characterization of the Hellings–Downs curve (sect. 2), GWB anisotropy (sect. 5), and individually resolvable CW sources (sect. 6). Fully harmonized IPTA releases remain indispensable for definitive inference, while LITE-style staged selection, FrankenStat likelihood-level combination, and Fourier-space regularization provide complementary paths to near-optimal global sensitivity on short timescales. Integrating these approaches will allow the community to preserve the robustness that established the first evidence for the GWB while unlocking the full discovery space of a truly global PTA.

## 11. – Complementary Science

**11.1. *Picohertz GW Searches.*** – At frequencies above  $\sim 1$  nHz, PTA sensitivity is set by the inverse of the observing baseline,  $1/T_{\text{obs}}$ , and the formalism of sect. 2 applies directly. A prominent gap in GW frequency coverage lies at  $10^{-16}$  Hz–1 nHz, the picohertz (pHz) regime, below the reach of standard PTA analysis but above the band probed by CMB tensor modes [320].

Strong theoretical motivation exists for signals in this band. SMBHBs at wide orbital separations radiate pHz GWs during the early, environment-driven inspiral phase dis-

cussed in sect. 4 [25]. In addition, several cosmological sources predicted to contribute in this band—cosmic strings [222, 223], bubble collisions [227], electroweak phase transitions [224], turbulent QCD phase transitions [225, 226, 321], primordial GWs from inflation [230, 322], and preheating [229]—overlap with those discussed in sect. 8, but at wavelengths far longer than the PTA baseline.

When the GW period vastly exceeds  $T_{\text{obs}}$ , the wave is effectively “frozen” and manifests as a quasi-static spatial distortion rather than a time-varying signal. Traditional cross-correlation methods are therefore inapplicable. Instead, the GW-induced redshift appears as a drift in observed timing parameters—spin period derivatives, binary orbital period derivatives—that can be measured with decades of high-precision data [323–325].

The underlying physics mirrors the nanoHertz case. A passing GW induces an apparent velocity between pulsar  $a$  and the solar system barycenter (SSB):

$$(81) \quad v_{\text{GW}} = \sum_{A=+, \times} F_a^A(\hat{\Omega}) [s_A(t, \mathbf{0}) - s_A(t_p, L_a \hat{p}_a)],$$

where  $s_A(t, \mathbf{x})$  is the strain at position  $\mathbf{x}$ ,  $L_a$  is the pulsar distance,  $\hat{p}_a$  is the unit vector toward the pulsar, and  $t_p = t - L_a(1 + \hat{\Omega} \cdot \hat{p}_a)/c$  is the retarded time at the pulsar (cf. eq. (13)). The difference in brackets is the familiar Earth–Pulsar term structure discussed in sect. 2.2. The antenna beam pattern  $F_a^A(\hat{\Omega})$  has the same form as eq. (14):

$$(82) \quad F_a^A(\hat{\Omega}) = \frac{\hat{p}_a^i \hat{p}_a^j e_{ij}^A(\hat{\Omega})}{2(1 + \hat{\Omega} \cdot \hat{p}_a)},$$

where  $e_{ij}^A$  is the polarization tensor. Crucially, at picohertz frequencies the condition  $2\pi f L_a/c < 1$  is satisfied for many PTA pulsars, so the short-wavelength approximation (sect. 2.2; [53, 57]) breaks down and the pulsar term cannot be averaged away. This is a qualitative difference from the nanoHertz regime: the Earth and pulsar terms are coherent, and the full two-point spatial structure of the GW field is accessible.

For pHz GWs, the time derivatives of the induced redshift can be truncated at leading order since  $T_{\text{obs}} \ll 1/f$ . These derivatives contribute to the observed values of time-dependent pulsar parameters. For a pulsar in a binary system, the observed orbital period derivative can be decomposed as:

$$(83) \quad \frac{\dot{P}_b^{\text{Obs}}}{P_b} = \frac{\dot{P}_b^{\text{Int}}}{P_b} - a_{\text{Kin}} - a_{\text{MW}} - a_{\text{GW}},$$

where  $\dot{P}_b^{\text{Int}}/P_b$  is the intrinsic orbital decay from GW emission,  $a_{\text{Kin}}$  is the Shklovskii kinematic term [212],  $a_{\text{MW}}$  is the Milky Way gravitational acceleration (see also sect. 11.2), and  $a_{\text{GW}} = \dot{v}_{\text{GW}}$  is the pHz GW signal. Ref. [325] developed a Bayesian framework for pHz searches that allows flexible control of these uncertainties (fig. 21). With the dramatic increase in pulsar discoveries and timing precision expected from next-generation telescopes, these methods will evolve from upper-limit exercises into genuine discovery tools for probing both SMBHB evolution at wide separations and the cosmological sources discussed in sect. 8.

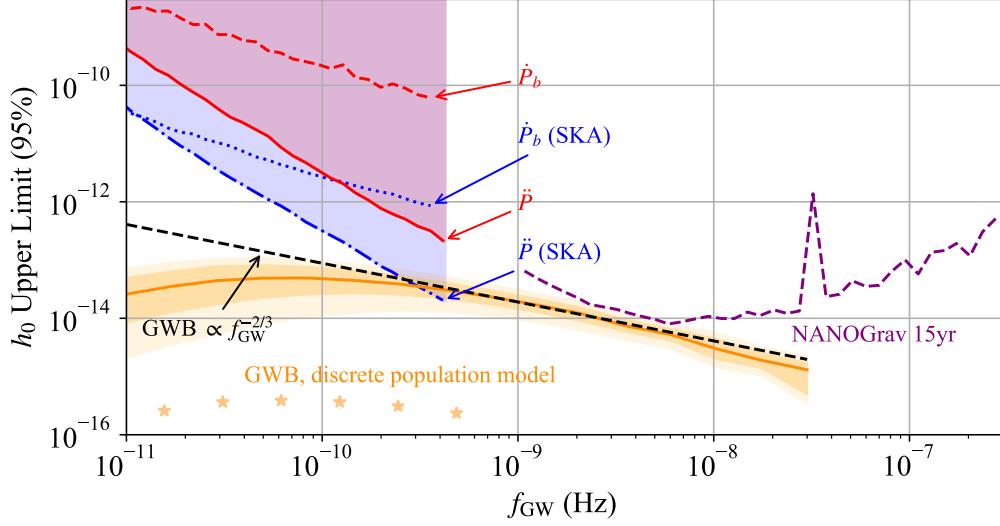


Fig. 21. – Strain amplitude upper limits and forecast sensitivities for pHz CW searches using pulsar timing parameters  $\dot{P}_b$  and  $\ddot{P}$  [325]. Fiducial sources are circular-orbit SMBHBs. SKAO forecasts (not shown) provide an additional order of magnitude improvement from increased data volume alone. Current limits are comparable to nanoHertz PTA CW upper limits (purple dashed) at certain frequencies. Stars denote expected individual CW sources from a population model; these lie  $\sim 3$  orders of magnitude below current constraints. The orange curve is the GWB spectrum from a quasar-based population model (sect. 4) matched to the NANOGrav GWB at  $f_{\text{GW}} = 1 \text{ yr}^{-1}$ , with shaded uncertainty quantiles. The black dashed line is the corresponding power-law fit.

**11.2. Mapping Galactic Acceleration.** – For pulsars in binary orbits, precise PTA data allows us to measure not only the orbital periods of the systems (denoted  $P_b$ ), but the change in these periods over time ( $\dot{P}_b$ ). The change we measure,  $\dot{P}_b^{\text{Obs}}$ , is the combined effect of several factors [326]:

$$(84) \quad \dot{P}_b^{\text{Obs}} = \dot{P}_b^{\text{Kin}} + \dot{P}_b^{\text{GW}} + \dot{P}_b^{\text{Gal}} + \dot{P}_b^{\text{n}}.$$

The kinematic or Shklovskii term  $\dot{P}_b^{\text{Kin}}$  accounts for time dilation effects [212]. It depends on the proper motion and distance of the pulsar system.  $\dot{P}_b^{\text{GW}}$  is the change in orbital period due to GW radiation, and depends on the pulsar and companion masses and orbit eccentricity, see [327].  $\dot{P}_b^{\text{Gal}}$  is the change due to galactic acceleration, and  $\dot{P}_b^{\text{n}}$  is a nuisance term which characterizes all other contributions to the time derivative.

The galactic term is of particular interest because it can be used as in [328, 329] to determine the line-of-sight relative acceleration between the pulsar and the Earth via:

$$(85) \quad \mathbf{a}_{\text{Gal}} = c \frac{\dot{P}_b^{\text{Gal}}}{P_b} \hat{\mathbf{r}},$$

where  $c$  is the speed of light, and  $\hat{\mathbf{r}}$  is the unit vector pointing from the Earth to the

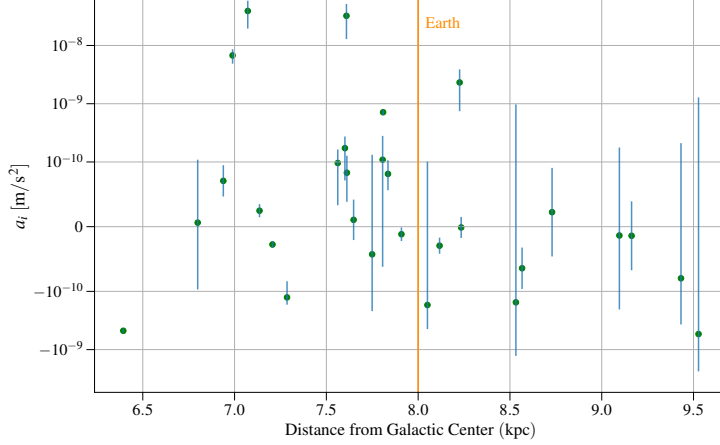


Fig. 22. – The line-of-sight relative acceleration between the Earth and each binary system from Ref. [329] as a function of distance from the center of the Milky Way. The Earth is shown for reference. Error bars do not account for acceleration noise encapsulated in  $\dot{P}_b^n$ .

pulsar. By creating a catalog of pulsars with measured orbital period derivatives, masses, and independent distance measurements it is possible to isolate the quantity  $\dot{P}_b^{\text{Gal}} + \dot{P}_b^n$ . By further eliminating known noise sources (such as accreting binary systems), we can write  $\dot{P}_b^n \approx 0$ , and statistically account for unknown noise sources later in the analysis. Thus we can isolate the galactic term  $\dot{P}_b^{\text{Gal}}$ . fig. 22 shows the galactic acceleration values calculated via eq. (85) for 29 pulsars in Ref. [329].

To evaluate these data, Ref. [329] expands the galactic potentially locally as

$$(86) \quad \mathbf{a}_{\text{Gal}} = a'_x \mathbf{x} + a'_z \mathbf{z}$$

where  $\mathbf{x}$  and  $\mathbf{z}$  are the vector differences between a given pulsar's position and the Earth in galactocentric coordinates ( $\mathbf{x}$  points away from the Galactic Center and  $\mathbf{z}$  towards the Galactic North Pole).  $a'_x$  and  $a'_z$  are the acceleration gradients in each of these directions.

Parameter estimation of  $a'_x$  and  $a'_z$  must account for noise in the data, since there is no way to guarantee  $\dot{P}_b^n = 0$  for all pulsars. Ref. [329] accordingly constructs a likelihood function with parameters  $p_n$  and  $\zeta$ , which represent the probability of noise in the data, and the amplitude of this noise, respectively. For the 29 pulsars in Ref. [329], an MCMC analysis finds a high probability for this noise, and resolves the noise amplitude, and acceleration gradients (see fig. 23).

We use Poisson equation to write the vertical acceleration gradient as:

$$(87) \quad a'_z = 4\pi G \rho_d$$

where  $G$  is the gravitational constant and  $\rho_d$  is the density of the Milky Way disk. The value of  $\rho_d$  corresponding to the best-fit  $a'_z$  from Ref. [329] is shown alongside other measurements in tab. V. Chakrabarti et al. [328] independently applied this technique to

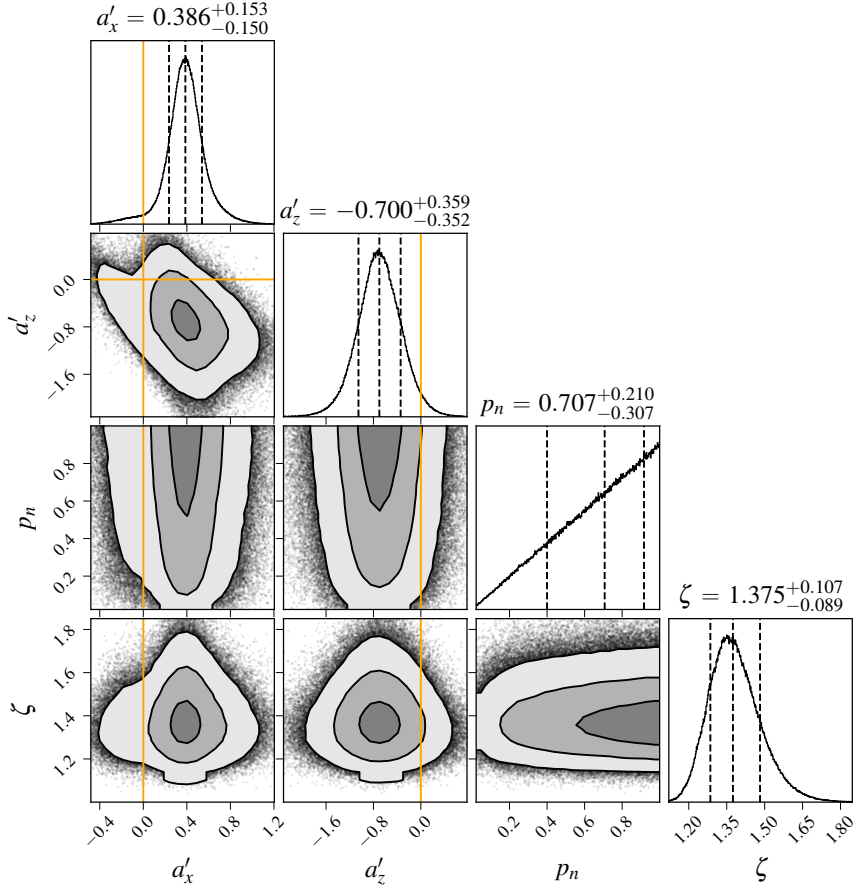


Fig. 23. – Posterior distributions for the galactic acceleration gradients  $a'_x$  and  $a'_z$  and the noise parameters  $p_n$  and  $\zeta$ . The 16th, 50th, and 84th percentiles are shown with black lines. The acceleration gradient values shown have units of  $[10^{-10} \text{ m s}^{-2} \text{ kpc}^{-1}]$ . The orange lines show the null hypothesis where  $a'_x = a'_z = 0$ .

measure galactic acceleration using binary pulsars. Both methods use eq. (85) to extract the line-of-sight acceleration from the galactic contribution to  $\dot{P}_b$ . The key difference is in the treatment of systematics: Chakrabarti et al. fit the acceleration gradients directly to their pulsar sample, while Moran et al. introduce the nuisance parameters  $p_n$  and  $\zeta$  to statistically account for pulsars whose  $\dot{P}_b$  may be contaminated by unmodeled effects. The use of precision acceleration measurements to constrain the local dark matter density was proposed by Ravi et al. [330], who showed that stellar accelerations measured via radial velocity surveys could probe  $\rho_d$  directly. The binary pulsar approach extends this idea by exploiting the exquisite timing precision of MSPs. The resulting  $\rho_d$  values from both Moran et al. and Chakrabarti et al. are of comparable precision to indirect methods (Jeans analyses, orbital arc fitting), as shown in tab. V. All five measurements are broadly consistent given their uncertainties, though the binary pulsar values tend to be lower than the Jeans-based estimates. As more independent pulsar distances become

available and timing data improve, this method will become increasingly powerful for constraining the local dark matter density.

Reference	$\rho_d$ ( $10^{-2} M_\odot/\text{pc}^3$ )
Ref. [329]	$3.6_{-2.1}^{+2.0}$
Ref. [331]	$5.6_{-3.1}^{+3.1}$
Ref. [332]	$10.2_{-1.0}^{+1.0}$
Ref. [333]	$7.6_{-1.5}^{+1.5}$
Ref. [328]	$8_{-2}^{+5}$

TABLE V. – Comparison of  $\rho_d$  values from the literature. Refs. [328, 329] use the binary pulsar method described here. Ref. [331] uses the orbital arc method, and Refs. [332, 333] use Jeans analyses.

## 12. – Conclusion and Future Outlook

The independent evidence of a common red-noise process with Hellings–Downs correlations by the NANOGrav, EPTA, InPTA, PPTA, CPTA, and MPTA collaborations marks the opening of the nanoHertz GW window. After decades of precision monitoring, the local Galaxy has been successfully transformed into a kiloparsec-scale GW detector. As we transition from evidence to characterization, six themes that mirror the structure of this review, define the roadmap for the next decade:

**The GWB.** The recovered GWB amplitude lies at the upper end of early predictions, but there is still some tension with astrophysical GWB models. As detailed in sect. 3 and sect. 4, the “stalling” crisis has been superseded by evidence that binaries merge efficiently, though the exact physical mechanism is still an active area of research. The high amplitude is a natural consequence of models that incorporate the VDF or quasar-based populations [67], and is consistent with recent JWST observations of over-massive black holes at high redshift. Indeed, new work is already using the GWB amplitude to constrain galactic feedback processes and massive black hole growth [87], infer the  $M_{\text{BH}}-M_{\text{bulge}}$  relation out to  $z \sim 1$  [334], and place energetic ceilings on astrophysical GW backgrounds [89]. These ceilings constrain the maximum GW energy density from astrophysical sources in the most model-agnostic way currently available, complementing the population-level inferences above. Beyond amplitude, the spectral shape of the GWB is itself becoming a measurable quantity: piecewise power-law reconstructions [335] and searches for a running spectral index [336] are providing the first model-independent spectral characterization, while systematic studies of individual pulsar contributions to the signal [337] and harmonic analyses of the angular correlations [62] are cross-checking the evidence for the GWB. A key diagnostic will be signs of spectral discreteness—departures from a smooth  $f^{-2/3}$  power law at high frequencies due to the finite number of SMBHBs per frequency bin [28] (sect. 5.2). Such features would simultaneously confirm the astrophysical origin of the signal, distinguishing it from a smooth cosmological background, indicate the onset of GWB anisotropy, and mark the transition to individually resolvable sources.

**GWB anisotropy.** An astrophysical GWB is guaranteed to be anisotropic, and detecting that anisotropy—or resolving the individual SMBHBs that produce it—is a central goal of the next decade (sect. 5). The intrinsic shot-noise anisotropy grows steeply with frequency ( $C_{\ell>0}/C_0 \propto f^{11/3}$ ; sect. 5.2.1), so sensitivity to anisotropy improves most rapidly at high frequencies, with long baselines and large PTAs. At high frequencies ( $f \gtrsim 26$  nHz) the  $f^{-2/3}$  power-law spectrum breaks down [28] (sect. 5.2), and depending on the confusion limit, the loudest binaries will either imprint detectable anisotropy on the background or become individually resolvable as CWs. At lower frequencies, where many sources overlap per bin, the anisotropy instead traces LSS and can be cross-correlated with galaxy catalogs to constrain the source population and its redshift evolution [157, 338] (sect. 5.4), or to infer the structure of the inner galaxy from the aggregate angular distribution of sources [339]. Complementary analytical estimates by Lin, Lidz & Ma [340] confirm that shot-noise anisotropy dominates over the LSS contribution by two to three orders of magnitude, and that its frequency dependence can diagnose SMBHB residence times. Extracting these signals faces two systematic hurdles: small-scale leakage bias in current anisotropy estimators [160] (sect. 5.5), which regularization alone does not fully resolve, and cosmic variance from a finite source population, which can produce realization-dependent deviations from Hellings–Downs correlations that mimic anisotropy [159]. Addressing both will require new estimator frameworks—per-frequency optimal statistics that account for inter-pair covariance and cosmic variance [145, 163], and joint inference over resolved and unresolved angular scales. Recent forecasts [145, 158] suggest that per-frequency searches offer substantially better prospects than broadband approaches.

**From anisotropy to resolvability.** The boundary between a stochastic background and a collection of individually resolvable sources may shift substantially as the SMBHB population becomes better understood. Both energetic ceiling arguments [89] and demographic analyses [341] suggest that the GWB amplitude favors SMBHBs more massive than inferred from local scaling relations. Recent JWST observations of over-massive black holes at high redshift support this picture. More massive binaries evolve faster— $\dot{f} \propto \mathcal{M}^{5/3} f^{11/3}$ —reducing the bin occupancy  $\Delta N \propto \mathcal{M}^{-5/3}$  (eq. (7)). A population dominated by systems with chirp mass  $\mathcal{M} \sim 10^{10} M_\odot$  has  $\Delta N$  a factor of  $\sim 50$  smaller than the canonical  $\mathcal{M} = 10^9 M_\odot$  estimate, significantly reducing  $\Delta N$  across the PTA band and lowering the frequency at which individual sources become resolvable. In this scenario, notion of GWB anisotropy from these loud individual binaries may need to be reframed: there would be no mid-to-high frequency confusion background, only discrete sources to be detected one by one. The only true stochastic anisotropy would then reside at the lowest frequencies, where many sources still overlap and their spatial clustering traces the LSS (sect. 5.4). This raises the question posed by Cornish & Romano [50]: when is a GWB truly stochastic? At high frequencies, where the number of sources per bin is small, it may be more productive to search simultaneously for CWs and the GWB using cross-correlation statistics such as the single-source fingerprint  $\Upsilon_{ab}$  (sect. 6.7) rather than attempting to characterize GWB anisotropy in a regime where the background itself is dissolving into discrete sources.

**Continuous GWs from individual binaries.** The search for individual binaries has evolved from all-sky limits (sect. 6) to rigorous hypothesis testing of electromagnetic candidates. Targeted searches for SMBHBs in known galaxy pairs are now underway [42], and quasar variability studies suggest that quasars themselves may signpost close binary systems [191]. Coordinating nanoHertz GW follow-up with multi-messenger electromag-

netic campaigns [167] will be essential for confirming the first CW detection. The path to detection requires a protocol to rule out red-noise false positives: candidates must survive phase scrambling, demonstrate robustness against correlated background models, and withstand dropout analyses across the array. The new single-source fingerprint  $\Upsilon_{ab}$  (sect. 6.7) provides a geometry-dependent discriminant between a CW and the isotropic GWB, and may become a useful tool.

**New physics.** The GWB spectrum may encode signals beyond the standard SMBHB picture. While the astrophysical background is expected to fracture into discrete sources at high frequencies (sect. 5.2), a cosmological background from inflation or phase transitions would remain smooth and isotropic across the PTA band. Searches for signs of discreteness in the GWB [28] and for GW memory events [342] are already probing this boundary. Distinguishing astrophysical and cosmological scenarios requires measuring the spectral index for deviations from  $\gamma = 13/3$ , searching for persistent isotropy where astrophysical models predict resolvability, and testing for non-Einsteinian polarization modes (sect. 8). Searches for transverse polarization modes [343] have placed the first constraints on scalar and vector contributions—monopolar or dipolar correlations rather than the quadrupolar Hellings–Downs curve—which would signal alternative gravity theories or exotic early-Universe sources.

**Custom noise models.** Accurate per-pulsar noise characterization underpins every result discussed above (sect. 9). As datasets grow in length and sensitivity, noise misspecification becomes the dominant systematic: it can bias the inferred GWB amplitude, inflate or suppress CW candidates, and corrupt anisotropy maps. Advances in chromatic noise modeling with time-domain kernels [244] and the treatment of spatially correlated noise sources such as the solar wind are essential to keep pace with improving data quality. Custom pulsar noise models will remain foundational for PTA science.

**Data combination and the future.** The future of the field lies in data synthesis and array expansion. Rapid combination frameworks—LITE [316], FrankenStat [317], and Fourier-space regularization [318] (sect. 10)—are essential to achieve near-optimal global sensitivity on timescales of months rather than years. Two next-generation facilities will transform the PTA landscape: the SKAO [141], which will deliver a factor of three to four improvement in sensitivity and enable the largest pulsar sample ever timed for GW science, and DSA-2000 [140, 344], which will contribute high-cadence timing of up to 200 millisecond pulsars and systematic identification of electromagnetic counterparts. Together, these instruments will enable the transition from the incoherent to the coherent regime (sect. 7). By integrating high-precision distances from *Gaia* parallaxes of pulsar companions and VLBI (sect. 6.12), the combined array will function as a Galactic-scale interferometer with sub-arcminute source localization. The extension of baselines to decades will simultaneously open the picohertz window (sect. 11.1), where recent theoretical work has shown that secular drifts in pulsar parameters can probe SMBHB evolution at wide separations, ultralight dark matter, and the physics of the early Universe [26, 325].

Evidence for the GWB is just the beginning. The challenge for the next decade is to extract astrophysical and cosmological information from the signal, detect the first individual binary, and extend the GW spectrum to picohertz frequencies. With next-generation facilities on the horizon and a growing body of new science already emerging from existing data, there is good reason to believe that PTAs will become a cornerstone of multi-band GW astronomy.

## Acknowledgements

The authors thank M. Lam for his careful reading of this manuscript, providing a link to the DSA-2000 community document, and for useful discussions about GWB anisotropy and scaling laws. They thank P. Petrov for providing fig. 11. They also thank IPTA colleagues for sending comments on this review, and especially Małgorzata Curyło and Boris Goncharov for sharing additional GWB models for fig. 5 and detailed comments on custom noise models, and G. Shaifullah and J. Verbiest for their comments on fig. 19. C. M. F. M. thanks Ue-Li Pen for useful discussions about the GWB polarization, Meg Urry for suggestion fig. 7, and V. Ozolins for useful conversations. She also thanks all her students, past and present, who are the co-authors of this work, for being a constant source of joy. C. M. F. M. was supported in part by the National Science Foundation under Grants No. NSF PHY-1748958, NASA LPS 80NSSC24K0440, and NSF PHY-2309135 to the Kavli Institute for Theoretical Physics (KITP) where she carried out some of this work. C.M.F.M. also thanks the Center for Computational Astrophysics of the Flatiron Institute for support. The Flatiron Institute is supported by the Simons Foundation.

## references

- [1] ESTABROOK F. B. and WAHLQUIST H. D., *General Relativity and Gravitation*, **6** (1975) 439.
- [2] HULSE R. A. and TAYLOR J. H., *ApJ*, **195** (1975) L51.
- [3] TAYLOR J. H. and WEISBERG J. M., *ApJ*, **253** (1982) 908.
- [4] SAZHIN M., *Societ Ast*, **22** (1978) .
- [5] DETWEILER S., *AJ*, **234** (1979) .
- [6] HELLINGS R. and DOWNS G., *AJ*, **265** (1983) .
- [7] BACKER D. C., KULKARNI S. R., HEILES C., DAVIS M. M. and GOSS W. M., *Nature*, **300** (1982) 615.
- [8] FOSTER R. S. and BACKER D. C., *ApJ*, **361** (1990) 300.
- [9] KASPI V. M., TAYLOR J. H. and RYBA M. F., *ApJ*, **428** (1994) 713.
- [10] MCHUGH M. P., ZALAMANSKY G., VERNOTTE F. and LANTZ E., *Phys. Rev. D*, **54** (1996) 5993.
- [11] PHINNEY E. S., *arXiv:astro-ph/0108028*, (2001) .
- [12] MANCHESTER R. N., HOBBS G., BAILES M., COLES W. A., VAN STRATEN W., KEITH M. J., SHANNON R. M., BHAT N. D. R., BROWN A., BURKE-SPOLAOR S. G. *et al.*, *PASA*, **30** (2013) .
- [13] HOBBS G. B., EDWARDS R. T. and MANCHESTER R. N., *MNRAS*, **369** (2006) 655.
- [14] KRAMER M. and CHAMPION D. J., *Classical and Quantum Gravity*, **30** (2013) .
- [15] JENET F., FINN L. S., LAZIO J., LOMMEN A., McLAUGHLIN M., STAIRS I., STINEBRING D., VERBIEST J., ARCHIBALD A., ARZOUMANIAN Z. *et al.*, *arXiv e-prints*, (2009) .
- [16] HOBBS G., ARCHIBALD A., ARZOUMANIAN Z., BACKER D., BAILES M., BHAT N. D. R., BURGAY M., BURKE-SPOLAOR S., CHAMPION D., COGNARD I. *et al.*, *Classical and Quantum Gravity*, **27** (2010) .
- [17] ARZOUMANIAN Z., BAKER P. T., BLUMER H., BÉCSY B., BRAZIER A., BROOK P. R., BURKE-SPOLAOR S., CHATTERJEE S., CHEN S., CORDES J. M. *et al.*, *ApJ*, **905** (2020) L34.
- [18] GONCHAROV B., SHANNON R. M., REARDON D. J., HOBBS G., ZIC A., BAILES M., CURYLO M., DAI S., KERR M., LOWER M. E., MANCHESTER R. N., MANDOW R., MILES M. T., RUSSELL C. J., SPIEWAK R., THYAGARAJAN N. and ZHU X.-J., *ApJ*, **917** (2021) L19.

- [19] CHEN S., CABALLERO R. N., GUO Y. J., CHALUMEAU A., LIU K., SHAIFULLAH G., LEE K. J., BABAK S., DESVIGNES G., PARTHASARATHY A., HU H., VAN DER WATEREN E., ANTONIADIS J., BAK NIELSEN A. S., BASSA C. G., BERTHEREAU A., BURGAY M., CHAMPION D. J., COGNARD I., FALXA M., FERDMAN R. D., FREIRE P. C. C., GAIR J. R., GRAIKOU E., GUILLEMOT L., JANG J., JANSSEN G. H., KARUPPUSAMY R., KEITH M. J., KRAMER M., LIU X. J., LYNE A. G., MAIN R. A., MCKEE J. W., MICKALIGER M. B., PERERA B. B. P., PERRODIN D., PETITEAU A., PORAYKO N. K., POSSENTI A., SAMAJDAR A., SANIDAS S. A., SESANA A., SPERI L., STAPPERS B. W., THEUREAU G., TIBURZI C., VECCHIO A., VERBIEST J. P. W., WANG J., WANG L. and XU H., *MNRAS*, **508** (2021) 4970.
- [20] ANTONIADIS J., ARZUMANIAN Z., BABAK S., BAILES M., BAK NIELSEN A. S., BAKER P. T., BASSA C. G., BÉCSY B., BERTHEREAU A., BONETTI M., BRAZIER A., BROOK P. R., BURGAY M., BURKE-SPOLAOR S., CABALLERO R. N., CASEY-CLYDE J. A., CHALUMEAU A., CHAMPION D. J., CHARISI M., CHATTERJEE S., CHEN S., COGNARD I., CORDES J. M., CORNISH N. J., CRAWFORD F., CROMARTIE H. T., CROWTER K., DAI S., DECESAR M. E., DEMOREST P. B., DESVIGNES G., DOLCH T., DRACHLER B., FALXA M., FERRARA E. C., FIORE W., FONSECA E., GAIR J. R., GARVER-DANIELS N., GONCHAROV B., GOOD D. C., GRAIKOU E., GUILLEMOT L., GUO Y. J., HAZBOUN J. S., HOBBS G., HU H., ISLO K., JANSSEN G. H., JENNINGS R. J., JOHNSON A. D., JONES M. L., KAISER A. R., KAPLAN D. L., KARUPPUSAMY R., KEITH M. J., KELLEY L. Z., KERR M., KEY J. S., KRAMER M., LAM M. T., LAMB W. G., LAZIO T. J. W., LEE K. J., LENTATI L., LIU K., LUO J., LYNCH R. S., LYNE A. G., MADISON D. R., MAIN R. A., MANCHESTER R. N., MCEWEN A., MCKEE J. W., MCLAUGHLIN M. A., MICKALIGER M. B., MINGARELLI C. M. F., NG C., NICE D. J., OSŁOWSKI S., PARTHASARATHY A., PENNUCCI T. T., PERERA B. B. P., PERRODIN D., PETITEAU A., POL N. S., PORAYKO N. K., POSSENTI A., RANSOM S. M., RAY P. S., REARDON D. J., RUSSELL C. J., SAMAJDAR A., SAMPSON L. M., SANIDAS S., SARKISSIAN J. M., SCHMITZ K., SCHULT L., SESANA A., SHAIFULLAH G., SHANNON R. M., SHAPIRO-ALBERT B. J., SIEMENS X., SIMON J., SMITH T. L., SPERI L., SPIEWAK R., STAIRS I. H., STAPPERS B. W., STINEBRING D. R., SWIGGUM J. K., TAYLOR S. R., THEUREAU G., TIBURZI C., VALLISNERI M., VAN DER WATEREN E., VECCHIO A., VERBIEST J. P. W., VIGELAND S. J., WAHL H., WANG J. B., WANG J., WANG L., WITT C. A., ZHANG S. and ZHU X. J., *MNRAS*, **510** (2022) 4873.
- [21] AGAZIE G., ANUMARLAPUDI A., ARCHIBALD A. M., ARZUMANIAN Z., BAKER P. T., BÉCSY B., BLECHA L., BRAZIER A., BROOK P. R., BURKE-SPOLAOR S., BURNETTE R., CASE R., CHARISI M., CHATTERJEE S., CHATZIOANNOU K., CHEESEBORO B. D., CHEN S., COHEN T., CORDES J. M., CORNISH N. J., CRAWFORD F., CROMARTIE H. T., CROWTER K., CUTLER C. J., DECESAR M. E., DEGAN D., DEMOREST P. B., DENG H., DOLCH T., DRACHLER B., ELLIS J. A., FERRARA E. C., FIORE W., FONSECA E., FREEDMAN G. E., GARVER-DANIELS N., GENTILE P. A., GERSBACH K. A., GLASER J., GOOD D. C., GÜLTEKIN K., HAZBOUN J. S., HOURIHANE S., ISLO K., JENNINGS R. J., JOHNSON A. D., JONES M. L., KAISER A. R., KAPLAN D. L., KELLEY L. Z., KERR M., KEY J. S., KLEIN T. C., LAAL N., LAM M. T., LAMB W. G.,

- LAZIO T. J. W., LEWANDOWSKA N., LITTENBERG T. B., LIU T., LOMMEN A., LORIMER D. R., LUO J., LYNCH R. S., MA C.-P., MADISON D. R., MATTSON M. A., MCEWEN A., MCKEE J. W., MCLAUGHLIN M. A., MCMANN N., MEYERS B. W., MEYERS P. M., MINGARELLI C. M. F., MITRIDATE A., NATARAJAN P., NG C., NICE D. J., OCKER S. K., OLUM K. D., PENNUCCI T. T., PERERA B. B. P., PETROV P., POL N. S., RADOVAN H. A., RANSOM S. M., RAY P. S., ROMANO J. D., SARDESAI S. C., SCHMIEDEKAMP A., SCHMIEDEKAMP C., SCHMITZ K., SCHULT L., SHAPIRO-ALBERT B. J., SIEMENS X., SIMON J., SIWEK M. S., STAIRS I. H., STINEBRING D. R., STOVALL K., SUN J. P., SUSOBHANAN A., SWIGGUM J. K., TAYLOR J., TAYLOR S. R., TURNER J. E., UNAL C., VALLISNERI M., VAN HAASTEREN R., VIGELAND S. J., WAHL H. M., WANG Q., WITT C. A., YOUNG O. and NANOGRV COLLABORATION, *ApJ*, **951** (2023) L8.
- [22] ANTONIADIS J. *et al.*, *A&A*, **678** (2023) A50.
- [23] REARDON D. J., ZIC A., SHANNON R. M. *et al.*, *ApJ*, **951** (2023) L6.
- [24] XU H., CHEN S., GUO Y. *et al.*, *Research in Astronomy and Astrophysics*, **23** (2023) 075024.
- [25] BEGELMAN M. C., BLANDFORD R. D. and REES M. J., *Nature*, **287** (1980) 307.
- [26] AFZAL A., AGAZIE G., ANUMARLAPUDI A., ARCHIBALD A. M., ARZOUMANIAN Z., BAKER P. T., BÉCSY B., BLANCO-PILLADO J. J., BLECHA L., BODDY K. K., BRAZIER A., BROOK P. R., BURKE-SPOLAOR S., BURNETTE R., CASE R., CHARISI M., CHATTERJEE S., CHATZIOANNOU K., CHEESEBORO B. D., CHEN S., COHEN T., CORDES J. M., CORNISH N. J., CRAWFORD F., CROMARTIE H. T., CROWTER K., CUTLER C. J., DECESAR M. E., DEGAN D., DEMOREST P. B., DENG H., DOLCH T., DRACHLER B., VON ECKARDSTEIN R., FERRARA E. C., FIORE W., FONSECA E., FREEDMAN G. E., GARVER-DANIELS N., GENTILE P. A., GERSBACH K. A., GLASER J., GOOD D. C., GUERTIN L., GÜLTEKIN K., HAZBOUN J. S., HOURIHANE S., ISLO K., JENNINGS R. J., JOHNSON A. D., JONES M. L., KAISER A. R., KAPLAN D. L., KELLEY L. Z., KERR M., KEY J. S., LAAL N., LAM M. T., LAMB W. G., LAZIO T. J. W., LEE V. S. H., LEWANDOWSKA N., LINO DOS SANTOS R. R., LITTENBERG T. B., LIU T., LORIMER D. R., LUO J., LYNCH R. S., MA C.-P., MADISON D. R., MCEWEN A., MCKEE J. W., MCLAUGHLIN M. A., MCMANN N., MEYERS B. W., MEYERS P. M., MINGARELLI C. M. F., MITRIDATE A., NAY J., NATARAJAN P., NG C., NICE D. J., OCKER S. K., OLUM K. D., PENNUCCI T. T., PERERA B. B. P., PETROV P., POL N. S., RADOVAN H. A., RANSOM S. M., RAY P. S., ROMANO J. D., SARDESAI S. C., SCHMIEDEKAMP A., SCHMIEDEKAMP C., SCHMITZ K., SCHRÖDER T., SCHULT L., SHAPIRO-ALBERT B. J., SIEMENS X., SIMON J., SIWEK M. S., STAIRS I. H., STINEBRING D. R., STOVALL K., STRATMANN P., SUN J. P., SUSOBHANAN A., SWIGGUM J. K., TAYLOR J., TAYLOR S. R., TRICKLE T., TURNER J. E., UNAL C., VALLISNERI M., VERMA S., VIGELAND S. J., WAHL H. M., WANG Q., WITT C. A., WRIGHT D., YOUNG O., ZUREK K. M. and NANOGRV COLLABORATION, *ApJ*, **951** (2023) L11.
- [27] SESANA A. and FIGUEROA D. G., *arXiv e-prints*, (2025) arXiv:2512.18822.

- [28] AGAZIE G. *et al.*, *ApJ*, **978** (2025) 31.
- [29] ALLEN B., DHURANDHAR S., GUPTA Y., McLAUGHLIN M., NATARAJAN P., SHANNON R. M., THRANE E. and VECCHIO A., *arXiv e-prints*, (2023) .
- [30] MILES M. T., SHANNON R. M., REARDON D. J., BAILES M., CHAMPION D. J., GEYER M., GITIKA P., GRUNTHAL K., KEITH M. J., KRAMER M., KULKARNI A. D., NATHAN R. S., PARTHASARATHY A., SINGHA J., THEUREAU G., THRANE E., ABBATE F., BUCHNER S., CAMERON A. D., CAMILO F., MORESCHI B. E., SHAIFULLAH G., SHAMOHAMMADI M., POSSENTI A. and KRISHNAN V. V., *MNRAS*, **536** (2025) 1489.
- [31] AGAZIE G., ANUMARLAPUDI A., ARCHIBALD A. M., ARZOUMANIAN Z., BAKER P. T., BÉCSY B., BLECHA L., BRAZIER A., BROOK P. R., BURKE-SPOLAOR S., CHARISI M., CHATTERJEE S., COHEN T., CORDES J. M., CORNISH N. J., CRAWFORD F., CROMARTIE H. T., CROWTER K., DECESAR M. E., DEMOREST P. B., DOLCH T., DRACHLER B., FERRARA E. C., FIORE W., FONSECA E., FREEDMAN G. E., GARVER-DANIELS N., GENTILE P. A., GLASER J., GOOD D. C., GUERTIN L., GÜLTEKIN K., HAZBOUN J. S., JENNINGS R. J., JOHNSON A. D., JONES M. L., KAISER A. R., KAPLAN D. L., KELLEY L. Z., KERR M., KEY J. S., LAAL N., LAM M. T., LAMB W. G., LAZIO T. J. W., LEWANDOWSKA N., LIU T., LORIMER D. R., LUO J., LYNCH R. S., MA C.-P., MADISON D. R., McEWEN A., MCKEE J. W., McLAUGHLIN M. A., McMANN N., MEYERS B. W., MINGARELLI C. M. F., MITRIDATE A., NG C., NICE D. J., OCKER S. K., OLUM K. D., PENNUCCI T. T., PERERA B. B. P., POL N. S., RADOVAN H. A., RANSOM S. M., RAY P. S., ROMANO J. D., SARDESAI S. C., SCHMIEDEKAMP A., SCHMIEDEKAMP C., SCHMITZ K., SHAPIRO-ALBERT B. J., SIEMENS X., SIMON J., SIWEK M. S., STAIRS I. H., STINEBRING D. R., STOVALL K., SUSOBHANAN A., SWIGGUM J. K., TAYLOR S. R., TURNER J. E., UNAL C., VALLISNERI M., VIGELAND S. J., WAHL H. M., WITT C. A., YOUNG O. and NANOGRAV COLLABORATION, *ApJ*, **951** (2023) L10.
- [32] GONCHAROV B., REARDON D. J., SHANNON R. M., ZHU X.-J., THRANE E., BAILES M., BHAT N. D. R., DAI S., HOBBS G., KERR M., MANCHESTER R. N., OSŁOWSKI S., PARTHASARATHY A., RUSSELL C. J., SPIEWAK R., THYAGARAJAN N. and WANG J. B., *MNRAS*, **502** (2021) 478.
- [33] ANTONIADIS J., ARUMUGAM P., ARUMUGAM S., BABAK S., BAGCHI M., BAK NIELSEN A. S., BASSA C. G., BATHULA A., BERTHEREAU A., BONETTI M., BORTOLAS E., BROOK P. R., BURGAY M., CABALLERO R. N., CHALUMEAU A., CHAMPION D. J., CHANLARIDIS S., CHEN S., COGNARD I., DANDAPAT S., DEB D., DESAI S., DESVIGNES G., DHANDA-BATRA N., DWIVEDI C., FALXA M., FERDMAN R. D., FRANCHINI A., GAIR J. R., GONCHAROV B., GOPAKUMAR A., GRAIKOU E., GRIESSMEIER J. M., GUILLEMOT L., GUO Y. J., GUPTA Y., HISANO S., HU H., IRACI F., IZQUIERDO-VILLALBA D., JANG J., JAWOR J., JANSSEN G. H., JESSNER A., JOSHI B. C., KAREEM F., KARUPPUSAMY R., KEANE E. F., KEITH M. J., KHARBANDA D., KIKUNAGA T., KOLHE N., KRAMER M., KRISHNAKUMAR M. A., LACKEOS K., LEE K. J., LIU K., LIU Y., LYNE A. G., MCKEE J. W., MAAN Y., MAIN R. A., MICKALIGER M. B., NIȚU I. C., NOBLESON K., PALADI A. K., PARTHASARATHY A., PERERA B. B. P., PERRODIN D., PETITEAU A., PORAYKO N. K., POSSENTI A.,

- PRABU T., QUELQUEJAY LECLERE H., RANA P., SAMAJDAR A., SANIDAS S. A., SESANA A., SHAIFULLAH G., SINGHA J., SPERI L., SPIEWAK R., SRIVASTAVA A., STAPPERS B. W., SURNIS M., SUSARLA S. C., SUSOBHANAN A., TAKAHASHI K., TARAFDAR P., THEUREAU G., TIBURZI C., VAN DER WATEREN E., VECCHIO A., VENKATRAMAN KRISHNAN V., VERBIEST J. P. W., WANG J., WANG L. and WU Z., *Astron. Astrophys.*, **678** (2023) A49.
- [34] AGAZIE G., ANUMARLAPUDI A., ARCHIBALD A. M., BAKER P. T., BÉCSY B., BLECHA L., BONILLA A., BRAZIER A., BROOK P. R., BURKE-SPOLAOR S., BURNETTE R., CASE R., CASEY-CLYDE J. A., CHARISI M., CHATTERJEE S., CHATZIOANNOU K., CHEESEBORO B. D., CHEN S., COHEN T., CORDES J. M., CORNISH N. J., CRAWFORD F., CROMARTIE H. T., CROWTER K., CUTLER C. J., D’ORAZIO D. J., DECESAR M. E., DEGAN D., DEMOREST P. B., DENG H., DOLCH T., DRACHLER B., FERRARA E. C., FIORE W., FONSECA E., FREEDMAN G. E., GARDINER E., GARVER-DANIELS N., GENTILE P. A., GERSBACH K. A., GLASER J., GOOD D. C., GÜLTEKIN K., HAZBOUN J. S., HOURIHANE S., ISLO K., JENNINGS R. J., JOHNSON A., JONES M. L., KAISER A. R., KAPLAN D. L., KELLEY L. Z., KERR M., KEY J. S., LAAL N., LAM M. T., LAMB W. G., LAZIO T. J. W., LEWANDOWSKA N., LITTENBERG T. B., LIU T., LUO J., LYNCH R. S., MA C.-P., MADISON D. R., MCEWEN A., MCKEE J. W., MCLAUGHLIN M. A., MCMANN N., MEYERS B. W., MEYERS P. M., MINGARELLI C. M. F., MITRIDATE A., NATARAJAN P., NG C., NICE D. J., OCKER S. K., OLUM K. D., PENNUCCI T. T., PERERA B. B. P., PETROV P., POL N. S., RADOVAN H. A., RANSOM S. M., RAY P. S., ROMANO J. D., RUNNOE J. C., SARDESAI S. C., SCHMIEDEKAMP A., SCHMIEDEKAMP C., SCHMITZ K., SCHULT L., SHAPIRO-ALBERT B. J., SIEMENS X., SIMON J., SIWEK M. S., STAIRS I. H., STINEBRING D. R., STOVALL K., SUN J. P., SUSOBHANAN A., SWIGGUM J. K., TAYLOR J., TAYLOR S. R., TURNER J. E., UNAL C., VALLISNERI M., VIGELAND S. J., WACHTER J. M., WAHL H. M., WANG Q., WITT C. A., WRIGHT D. and YOUNG O., *Astrophys. J. Lett.*, **951** (2023) L11.
- [35] LIEPOLD E. R. and MA C.-P., *ApJ*, **971** (2024) L29.
- [36] BAÑADOS E., VENEMANS B. P., MAZZUCHELLI C., FARINA E. P., WALTER F., WANG F., DECARLI R., STERN D., FAN X., DAVIES F. B., HENNAWI J. F., SIMCOE R. A., TURNER M. L., RIX H.-W., YANG J., KELSON D. D., RUDIE G. C. and WINTERS J. M., *Nature*, **553** (2018) 473.
- [37] FAN X., BANADOS E. and SIMCOE R. A., *Annual Review of Astronomy and Astrophysics*, **61** (2023) 373.
- [38] BOGDÁN Á., GOULDING A. D., NATARAJAN P., KOVACS O. E., TREMBLAY G. R., CHADAYAMMURI U., KRAFT R. P., FORMAN W. R., JONES C., CHURAZOV E. and ZHURAVLEVA I., *Nature Astronomy*, **8** (2024) 126.
- [39] SESANA A., *Monthly Notices of the Royal Astronomical Society*, **433** (2013) L1.
- [40] CASEY-CLYDE J. A., MINGARELLI C. M. F., GREENE J. E., PARDO K., NAÑEZ M. and GOULDING A. D., *ApJ*, **924** (2022) 93.

- [41] ARZOUMANIAN Z., BAKER P. T., BRAZIER A., BROOK P. R., BURKE-SPOLAOR S., BÉCSY B., CHARISI M., CHATTERJEE S., CORDES J. M., CORNISH N. J., CRAWFORD F., CROMARTIE H. T., CROWTER K., DECESAR M. E., DEMOREST P. B., DOLCH T., ELLIOTT R. D., ELLIS J. A., FERDMAN R. D., FERARRA E. C., FONSECA E., GARVER-DANIELS N., GENTILE P. A., GOOD D. C., HAZBOUN J. S., ISLO K., JENNINGS R. J., JONES M. L., KAISER A. R., KAPLAN D. L., KELLEY L. Z., KEY J. S., LAM M. T., LAZIO T. J. W., LEVIN L., LUO J., LYNCH R. S., MADISON D. R., McLAUGHLIN M. A., MINGARELLI C. M. F., NG C., NICE D. J., PENNUCCI T. T., POL N. S., RANSOM S. M., RAY P. S., SHAPIRO-ALBERT B. J., SIEMENS X., SIMON J., SPIEWAK R., STAIRS I. H., STINEBRING D. R., STOVALL K., SWIGGUM J. K., TAYLOR S. R., VALLISNERI M., VIGELAND S. J., WITT C. A., ZHU W. and NANOGrav COLLABORATION, *ApJ*, **900** (2020) 102.
- [42] AGARWAL N. *et al.*, *ApJ*, (2026) .
- [43] TAYLOR S. R., *Ap&SS*, **370** (2025) .
- [44] SHAIFULLAH G. M., *Classical and Quantum Gravity*, **42** (2025) .
- [45] LIU K. and CHEN S., , (2025) .
- [46] SESANA A., VECCHIO A. and COLACINO C. N., *Monthly Notices of the Royal Astronomical Society*, **390** (2008) 192.
- [47] KOCSIS B. and SESANA A., *MNRAS*, **411** (2011) 1467.
- [48] ROSADO P. A., *Physical Review D*, **84** (2011) 084004.
- [49] REGIMBAU T., GIAMPANIS S., SIEMENS X. and MANDIC V., *Physical Review D*, **85** (2012) 066001.
- [50] CORNISH N. J. and ROMANO J. D., *Phys. Rev. D*, **92** (2015) 042001.
- [51] RAVI V., WYITHE J. S. B., SHANNON R. M., HOBBS G. and MANCHESTER R. N., *MNRAS*, **447** (2015) 2772.
- [52] ANHOLM M., BALLMER S., CREIGHTON J. D. E., PRICE L. R. and SIEMENS X., *Phys. Rev. D*, **79** (2009) 084030.
- [53] MINGARELLI C. M. F. and MINGARELLI A. B., *Journal of Physics Communications*, **2** (2018) 105002.
- [54] CORBIN V. and CORNISH N. J., *Class. Quantum Grav.*, **27** (2010) 235002.
- [55] MINGARELLI C., GROVER K., SIDERY T. *et al.*, *Physical Review Letters*, **108** (2012) .
- [56] MINGARELLI C. M. F., SIDERY T., MANDEL I. and VECCHIO A., *Phys. Rev. D*, **88** (2013) 062005.
- [57] MINGARELLI C. M. F. and SIDERY T., *Phys. Rev. D*, **90** (2014) 062011.

- [58] CHAMBERLIN S. J., CREIGHTON J. D. E., DEMOREST P., ELLIS J., PRICE L. R., ROMANO J. D., SIMON J., SIEMENS X. and VIGELAND S., *Phys. Rev. D*, **91** (2015) 044048.
- [59] ALI-HAÏMOUD Y., SMITH T. L. and MINGARELLI C. M. F., *Phys. Rev. D*, **102** (2020) 122005.
- [60] ROEBBER E. and HOLDER G., *ApJ*, **835** (2017) 21.
- [61] NAY J., BODDY K. K., SMITH T. L. and MINGARELLI C. M. F., *Phys. Rev. D*, **110** (2024) 044062.
- [62] NANOGRAV COLLABORATION, AGAZIE G. *et al.*, *Astrophys. J.*, **985** (2025) 99.
- [63] TIBURZI C., HOBBS G., KERR M., COLES W. A., DAI S., MANCHESTER R. N., POSSENTI A., SHANNON R. M. and YOU X. P., *MNRAS*, **455** (2016) 4339.
- [64] THORNE K. S., *Gravitational radiation*, in *300 Years of Gravitation*, edited by HAWKING S. W. and ISRAEL W. (Cambridge University Press, Cambridge) 1987, pp. 330–458.
- [65] MINGARELLI C. M. F., *Nature Astronomy*, **3** (2019) 8.
- [66] MINGARELLI C. M. F. and CASEY-CLYDE J. A., *Science*, **378** (2022) 592.
- [67] MINGARELLI C. M. F., BLECHA L., BOGDANOVIĆ T., CHARISI M., CHEN S., ESCALA A., GONCHAROV B., GRAHAM M. J., KOMOSSA S., MCWILLIAMS S. T., SCHWARTZ D. A. and ZRAKE J., *Nature Astronomy*, **9** (2025) 183.
- [68] RAJAGOPAL M. and ROMANI R. W., *ApJ*, **446** (1995) 543.
- [69] JAFFE A. H. and BACKER D. C., *ApJ*, **583** (2003) 616.
- [70] WYITHE J. S. B. and LOEB A., *ApJ*, **590** (2003) 691.
- [71] VAN HAASTEREN R., LEVIN Y., McDONALD P. and LU T., *MNRAS*, **395** (2009) 1005.
- [72] TAYLOR S. R. and GAIR J. R., *Phys. Rev. D*, **88** (2013) 084001.
- [73] LEE K., JENET F. A. and PRICE R. H., *ApJ*, **685** (2008) 1304.
- [74] SAMPSON L., CORNISH N. J. and MCWILLIAMS S. T., *Phys. Rev. D*, **91** (2015) 084055.
- [75] DVORKIN I. and BARAUSSE E., *MNRAS*, **470** (2017) 4547.
- [76] KELLEY L. Z., BLECHA L., HERNQUIST L., SESANA A. and TAYLOR S. R., *MNRAS*, **471** (2017) 4508.
- [77] BONETTI M., SESANA A., BARAUSSE E. and HAARDT F., *MNRAS*, **477** (2018) 2599.
- [78] RYU T., PERNA R., HAIMAN Z., OSTRIKER J. P. and STONE N. C., *MNRAS*, **473** (2018) 3410.

- [79] HAZBOUN J. S., SIMON J., SIEMENS X. and ROMANO J. D., *ApJ*, **905** (2020) L6.
- [80] GONCHAROV B., THRANE E., SHANNON R. M., HARMS J., BHAT N. D. R., HOBBS G., KERR M., MANCHESTER R. N., REARDON D. J., RUSSELL C. J., ZHU X.-J. and ZIC A., *ApJ*, **932** (2022) L22.
- [81] GONCHAROV B., SARDANA S., SESANA A., TOMSON S. M., ANTONIADIS J., CHALUMEAU A., CHAMPION D., CHEN S., KEANE E. F., LIU K., SHAIFULLAH G., SPERI L. and VALTOLINA S., *Nature Communications*, **16** (2025) 9692.
- [82] SIMON J., *ApJ*, **949** (2023) L24.
- [83] SATO-POLITO G., PARDO K., FISHBACH M., HOLZ D. E. and KAMIONKOWSKI M., *ApJ*, **949** (2023) 17.
- [84] MAIOLINO R., SCHOLTZ J., WITSTOK J., CARNIANI S., D'EUGENIO F., DE GRAAFF A., ÜBLER H., TACHELLA S., CURTIS-LAKE E., ARRIBAS S. *et al.*, *Nature*, **627** (2024) 59.
- [85] CASEY-CLYDE J. A., MINGARELLI C. M. F., GREENE J. E., PARDO K., NAÑEZ M. and GOULDING A. D., *ApJ*, **924** (2022) 93.
- [86] NI Y., CHEN N., DI MATTEO T., BIRD S., DEGRAF C., CROFT R., TREMMEL M. and FENG Y., *The Astrophysical Journal Letters*, **971** (2024) L19, (in press).
- [87] TILLMAN M. T., BURKHART B., MINGARELLI C. M. F., CASEY-CLYDE J. A., HERNQUIST L., BOSE S., REGOS E. and HERNÁNDEZ-AGUAYO C., *arXiv e-prints*, (2026) arXiv:2602.15938.
- [88] LAPI A., SHANKAR F., BOSI M., ROBERTS D., FU H., VARADARAJAN K. M. and BOCO L., *J. Cosmology Astropart. Phys.*, **2026** (2026) 001.
- [89] MINGARELLI C. M. F., *arXiv e-prints*, (2026) arXiv:2601.18859.
- [90] MA C.-P., GREENE J. E., MCCONNELL N., JANISH R., BLAKESLEE J. P., THOMAS J. and MURPHY J. D., *ApJ*, **795** (2014) 158.
- [91] MCCONNELL N. J. and MA C.-P., *ApJ*, **764** (2013) 184.
- [92] YU Q. and TREMAINE S., *MNRAS*, **335** (2002) 965.
- [93] SHANKAR F., WEINBERG D. H. and MIRALDA-ESCUDE J., *ApJ*, **690** (2009) 20.
- [94] SOLTAN A., *MNRAS*, **200** (1982) 115.
- [95] MARCONI A., RISALITI G., GILLI R., HUNT L. K., MAIOLINO R. and SALVATI M., *Monthly Notices of the Royal Astronomical Society*, **351** (2004) 169–185, arXiv: astro-ph/0311619.
- [96] HUGHES S. A. and BLANDFORD R. D., *ApJ*, **585** (2003) L101.
- [97] HUGHES S. A., *Phys. Rev. D*, **61** (2000) 084004.
- [98] BERTI E., CARDOSO V. and STARINETS A. O., *Classical and Quantum Gravity*, **26** (2009) 163001.

- [99] SESANA A., HAARDT F., MADAU P. and VOLONTERI M., *ApJ*, **611** (2004) 623.
- [100] ENOKI M., INOUE K. T., NAGASHIMA M. and SUGIYAMA N., *ApJ*, **615** (2004) 19.
- [101] SESANA A., VECCHIO A. and VOLONTERI M., *Monthly Notices of the Royal Astronomical Society*, **394** (2009) 2255.  
URL <https://doi.org/10.1111/j.1365-2966.2009.14499.x>
- [102] BARAUSSE E., *MNRAS*, **423** (2012) 2533.
- [103] SESANA A., *Classical and Quantum Gravity*, **30** (2013) 224014.
- [104] MCWILLIAMS S. T., OSTRIKER J. P. and PRETORIUS F., *ApJ*, **789** (2014) 156.
- [105] KULIER A., OSTRIKER J. P., NATARAJAN P., LACKNER C. N. and CEN R., *ApJ*, **799** (2015) 178.
- [106] ROSADO P. A., SESANA A. and GAIR J., *MNRAS*, **451** (2015) 2417.
- [107] ROEBBER E., HOLDER G., HOLZ D. E. and WARREN M., *ApJ*, **819** (2016) 163.
- [108] SESANA A., *Phys. Rev. Lett.*, **116** (2016) 231102.
- [109] RASSKAZOV A. and MERRITT D., *Phys. Rev. D*, **95** (2017) 084032.
- [110] CHEN S., SESANA A. and CONSELICE C. J., *Monthly Notices of the Royal Astronomical Society*, **488** (2019) 401.
- [111] ZHU X.-J., CUI W. and THRANE E., *MNRAS*, **482** (2019) 2588.
- [112] CHEN Y., YU Q. and LU Y., *ApJ*, **897** (2020) 86.
- [113] SIWEK M., KELLEY L. Z. and HERNQUIST L., *MNRAS*, **498** (2020) 531.
- [114] IZQUIERDO-VILLALBA D., SESANA A., BONOLI S. and COLPI M., *MNRAS*, **509** (2022) 3488.
- [115] BARAUSSE E., DEY K., CRISOSTOMI M., PANAYADA A., MARSAT S. and BASAK S., *Phys. Rev. D*, **108** (2023) 103034.
- [116] CURYŁO M. and BULIK T., *MNRAS*, **528** (2024) 1053.
- [117] CHEN N., DI MATTEO T., ZHOU Y., KELLEY L. Z., BLECHA L., NI Y., BIRD S., YANG Y. and CROFT R., *ApJ*, **991** (2025) L19.
- [118] GOULDING A. D., PARDO K., GREENE J. E., MINGARELLI C. M. F., NYLAND K. and STRAUSS M. A., *The Astrophysical Journal*, **879** (2019) L21.  
URL <https://doi.org/10.3847/2041-8213/2Fab2a14>
- [119] KOSS M. J., TREISTER E., KAKKAD D., CASEY-CLYDE J. A., KAWAMURO T., WILLIAMS J., FOORD A., TRAKHTENBROT B., BAUER F. E., PRIVON G. C., RICCI C., MUSHOTZKY R., BARCOS-MUNOZ L., BLECHA L., CONNOR T., HARRISON F., LIU T., MAGNO M., MINGARELLI C. M. F., MULLER-SANCHEZ F., OH K., SHIMIZU T. T., SMITH K. L., STERN D., TELLO M. P. and URRY C. M., *ApJ*, **942** (2023) L24.

- [120] QUINLAN G. D., *New Astronomy*, **1** (1996) 35.
- [121] SESANA A. and KHAN F. M., *MNRAS*, **454** (2015) L66.
- [122] IVANOV P. B., PAPALOIZOU J. C. B. and POLNAREV A. G., *MNRAS*, **307** (1999) 79.
- [123] PETERS P. C., *Phys. Rev.*, **136** (1964) B1224.
- [124] MIDDLETON H., SESANA A., CHEN S., VECCHIO A., DEL POZZO W. and ROSADO P. A., *Monthly Notices of the Royal Astronomical Society*, **502** (2021) L99.
- [125] SANDERS D. B., SOIFER B. T., ELIAS J. H., MADORE B. F., MATTHEWS K., NEUGEBAUER G. and SCOVILLE N. Z., *The Astrophysical Journal*, **325** (1988) 74.
- [126] VOLONTERI M., HAARDT F. and MADAU P., *The Astrophysical Journal*, **582** (2003) 559.
- [127] HOPKINS P. F., HERNQUIST L., COX T. J. and KEREŠ D., *The Astrophysical Journal Supplement Series*, **175** (2008) 356.
- [128] HOPKINS P. F., RICHARDS G. T. and HERNQUIST L., *The Astrophysical Journal*, **654** (2007) 731.
- [129] SHEN X., HOPKINS P. F., FAUCHER-GIGUÈRE C.-A., ALEXANDER D. M., RICHARDS G. T., ROSS N. P. and HICKOX R. C., *Monthly Notices of the Royal Astronomical Society*, **495** (2020) 3252.
- [130] KIS-TÓTH Á., HAIMAN Z. and FREI Z., *Classical and Quantum Gravity*, **42** (2025) 075007.
- [131] MIDDLETON H., DEL POZZO W., FARR W. M., SESANA A. and VECCHIO A., *Monthly Notices of the Royal Astronomical Society*, **455** (2016) L72–L76.
- [132] HOTINLI S. C., KAMIONKOWSKI M. and JAFFE A. H., *The Open Journal of Astrophysics*, **2** (2019) 8.
- [133] SATO-POLITO G. and KAMIONKOWSKI M., *Physical Review D*, **104** (2021) 103511.
- [134] TAYLOR S. R., MINGARELLI C. M. F., GAIR J. R., SESANA A., THEUREAU G., BABAK S., BASSA C. G., BREM P., BURGAY M., CABALLERO R. N., CHAMPION D. J., COGNARD I., DESVIGNES G., GUILLEMOT L., HESSELS J. W. T., JANSSEN G. H., KARUPPUSAMY R., KRAMER M., LASSUS A., LAZARUS P., LENTATI L., LIU K., OSŁOWSKI S., PERRODIN D., PETITEAU A., POSSENTI A., PURVER M. B., ROSADO P. A., SANIDAS S. A., SMITS R., STAPPERS B., TIBURZI C., VAN HAASTEREN R., VECCHIO A., VERBIEST J. P. W. and EPTA COLLABORATION, *Phys. Rev. Lett.*, **115** (2015) 041101.
- [135] TAYLOR S. R., VAN HAASTEREN R. and SESANA A., *Phys. Rev. D*, **102** (2020) 084039.
- [136] POL N., TAYLOR S. R. and ROMANO J. D., *Astrophys. J.*, **940** (2022) 173.
- [137] AGAZIE G. *et al.*, *ApJ*, **956** (2023) L3.

- [138] CORNISH N. J. and VAN HAASTEREN R., *Physical Review D*, **90** (2014) 122003.
- [139] ALI-HAÏMOUD Y., SMITH T. L. and MINGARELLI C. M. F., *Phys. Rev. D*, **103** (2021) 042009.
- [140] HALLINAN G. *et al.*, *arXiv e-prints*, (2019) .
- [141] SHANNON R. M. *et al.*, *arXiv e-prints*, (2025) .
- [142] GRUNTHAL K., CHAMPION D. J., THRANE E., NATHAN R. S., KRAMER M. and MILES M. T., *A&A*, **706** (2026) A352.
- [143] BALLMER S. W., *Classical and Quantum Gravity*, **23** (2006) S179.
- [144] MITRA S., DHURANDHAR S., SOURADEEP T., LAZZARINI A., MANDIC V., BOSE S. and BALLMER S., *Phys. Rev. D*, **77** (2008) .
- [145] KONSTANDIN T., LEMKE A.-M., MITRIDATE A. and PERBONI E., *J. Cosmology Astropart. Phys.*, **2026** (2026) 084.
- [146] GRUNTHAL K. *et al.*, *MNRAS*, **536** (2025) 1501.
- [147] CHEN Y., ZHAO S.-Y., PENG Z.-Z., ZHU X., BHAT N. D. R., CHEN Z.-C., CURYŁO M., DI MARCO V., HOBBS G., KAPUR A., LING W., MANDOW R., MISHRA S., REARDON D. J., RUSSELL C. J., SHANNON R. M., CARDINAL TREMBLAY J., WANG J., ZHANG L. and ZIC A., *arXiv e-prints*, (2026) arXiv:2602.11529.
- [148] ANIL KUMAR N., ÇALIŞKAN M., SATO-POLITO G., KAMIONKOWSKI M. and JI L., *Phys. Rev. D*, **110** (2024) 043501.
- [149] SATO-POLITO G. and KAMIONKOWSKI M., *Physical Review D*, **109** (2024) 123507.
- [150] AGAZIE G., ANUMARLAPUDI A., ARCHIBALD A. M., ARZOUMANIAN Z., BAKER P. T., BÉCSY B., BLECHA L., BRAZIER A., BROOK P. R., BURKE-SPOLAOR S., CASE R., CASEY-CLYDE J. A., CHARISI M., CHATTERJEE S., COHEN T., CORDES J. M., CORNISH N. J., CRAWFORD F., CROMARTIE H. T., CROWTER K., DECESAR M. E., DEMOREST P. B., DIGMAN M. C., DOLCH T., DRACHLER B., FERRARA E. C., FIORE W., FONSECA E., FREEDMAN G. E., GARVER-DANIELS N., GENTILE P. A., GLASER J., GOOD D. C., GÜLTEKIN K., HAZBOUN J. S., HOURIHANE S., JENNINGS R. J., JOHNSON A. D., JONES M. L., KAISER A. R., KAPLAN D. L., KELLEY L. Z., KERR M., KEY J. S., LAAL N., LAM M. T., LAMB W. G., LAZIO T. J. W., LEWANDOWSKA N., LIU T., LORIMER D. R., LUO J., LYNCH R. S., MA C.-P., MADISON D. R., MCEWEN A., MCKEE J. W., McLAUGHLIN M. A., McMANN N., MEYERS B. W., MEYERS P. M., MINGARELLI C. M. F., MITRIDATE A., NG C., NICE D. J., OCKER S. K., OLUM K. D., PENNUCCI T. T., PERERA B. B. P., PETROV P., POL N. S., RADOVAN H. A., RANSOM S. M., RAY P. S., ROMANO J. D., SARDESAI S. C., SCHMIEDEKAMP A., SCHMIEDEKAMP C., SCHMITZ K., SHAPIRO-ALBERT B. J., SIEMENS X., SIMON J., SIWEK M. S., STAIRS I. H., STINEBRING D. R., STOVALL K., SUSOBHANAN A., SWIGGUM J. K., TAYLOR J., TAYLOR S. R., TURNER J. E., UNAL C., VALLISNERI M., VAN HAASTEREN R., VIGELAND S. J., WAHL H. M., WITT C. A., YOUNG O. and NANO GRAV COLLABORATION, *ApJ*, **951** (2023) L50.

- [151] KATO R. and SODA J., *Phys. Rev. D*, **93** (2016) 062003.  
URL <https://link.aps.org/doi/10.1103/PhysRevD.93.062003>
- [152] CONNEELY C., JAFFE A. H. and MINGARELLI C. M. F., *MNRAS*, **487** (2019) 562.
- [153] JOW D. L., TSAI A. C. and PEN U.-L., *arXiv e-prints*, (2025) .
- [154] DAI L., KAMIONKOWSKI M., KOVETZ E. D., RACCANELLI A. and SHIRAIISHI M., *Phys. Rev. D*, **93** (2016) 023507.
- [155] KOVETZ E. D., RACCANELLI A. and RAHMAN M., *Mon. Not. Roy. Astron. Soc.*, **468** (2017) 3650, arXiv: 1606.07434.
- [156] SCELFO G., BELLOMO N., RACCANELLI A., MATARRESE S. and VERDE L., *JCAP*, **09** (2018) 039, arXiv: 1809.03528.
- [157] SEMENZATO F. *et al.*, *arXiv e-prints*, (2024) .
- [158] LEMKE A.-M., MITRIDATE A. and GERSBACH K. A., *Phys. Rev. D*, **111** (2025) 063068.
- [159] KONSTANDIN T., LEMKE A.-M., MITRIDATE A. and PERBONI E., , (2024) .
- [160] SEMENZATO F., BELLOMO N., RACCANELLI A. and MINGARELLI C. M. F., *arXiv e-prints*, (2025) arXiv:2510.24857.
- [161] GARDINER E. *et al.*, *ApJ*, **965** (2024) 164.
- [162] SCHULT L., PETROV P., TAYLOR S. R., POL N., LAAL N., CHARISI M. and MA C.-P., *arXiv e-prints*, (2025) arXiv:2510.01317.  
URL <https://arxiv.org/abs/2510.01317>
- [163] GERSBACH K. A., TAYLOR S. R., BÉCSY B., LEMKE A.-M., MITRIDATE A. and POL N., *arXiv e-prints*, (2025) .
- [164] MINGARELLI ET AL. C. M. F., *Nature Astronomy*, **1** (2017) 886.
- [165] BOGDANOVIĆ T., MILLER M. C. and BLECHA L., *Living Reviews in Relativity*, **25** (2022) 3.
- [166] D’ORAZIO D. J. and CHARISI M., *arXiv e-prints*, (2023) arXiv:2310.16896.
- [167] BURKE-SPOLAOR S., BOGDANOVIĆ T., D’ORAZIO D. J., ERACLEOUS M., GEZARI S., GRAHAM M. J., GÜLTEKIN K., HAZBOUN J., MINGARELLI C. M. F., NARAYAN G., PETROV P. and VERONESI N., *arXiv e-prints*, (2025) arXiv:2512.15911.
- [168] PETROV P., TAYLOR S. R., CHARISI M. and MA C.-P., *ApJ*, **976** (2024) 129.
- [169] MACFADYEN A. I. and MILOSAVLJEVIĆ M., *ApJ*, **672** (2008) 83.
- [170] D’ORAZIO D. J. and HAIMAN Z., *MNRAS*, **470** (2017) 1198.
- [171] GRAHAM M. J. *et al.*, *Nature*, **518** (2015) 74.

- [172] CHARISI M. *et al.*, *MNRAS*, **463** (2016) 2145.
- [173] ERACLEOUS M. *et al.*, *ApJS*, **201** (2012) 23.
- [174] SHEN Y. *et al.*, *ApJ*, **719** (2010) 1693.
- [175] BURKE-SPOLAOR S., *MNRAS*, **410** (2011) 2113.
- [176] FALXA M., BABAK S., BAKER P. T., BÉCSY B., CHALUMEAU A., CHEN S., CHEN Z., CORNISH N. J., GUILLEMOT L., HAZBOUN J. S. *et al.*, *MNRAS*, **521** (2023) 5077.
- [177] ZHAO S.-Y., CHEN Z.-C., TREMBLAY J. C., GONCHAROV B., ZHU X.-J. *et al.*, *ApJ*, **992** (2025) 181.
- [178] ANTONIADIS J. *et al.*, *A&A*, **678** (2023) A50.
- [179] IGUCHI S. *et al.*, *ApJ*, **724** (2010) L166.
- [180] BÉCSY B., CORNISH N. J., PETROV P., SIEMENS X., TAYLOR S. R., VIGELAND S. J. and WITT C. A., *Classical and Quantum Gravity*, **42** (2025) 175016.
- [181] AGGARWAL K., ARZOUMANIAN Z., BAKER P. T., BRAZIER A., BRINSON M. R., BROOK P. R., BURKE-SPOLAOR S., CHATTERJEE S., CORDES J. M., CORNISH N. J., CRAWFORD F., CROWTER K., CROMARTIE H. T., DECESAR M., DEMOREST P. B., DOLCH T., ELLIS J. A., FERDMAN R. D., FERRARA E., FONSECA E., GARVER-DANIELS N., GENTILE P., HAZBOUN J. S., HOLGADO A. M., HUERTA E. A., ISLO K., JENNINGS R., JONES G., JONES M. L., KAISER A. R., KAPLAN D. L., KELLEY L. Z., KEY J. S., LAM M. T., LAZIO T. J. W., LEVIN L., LORIMER D. R., LUO J., LYNCH R. S., MADISON D. R., MCLAUGHLIN M. A., MCWILLIAMS S. T., MINGARELLI C. M. F., NG C., NICE D. J., PENNUCCI T. T., POL N. S., RANSOM S. M., RAY P. S., SIEMENS X., SIMON J., SPIEWAK R., STAIRS I. H., STINEBRING D. R., STOVALL K., SWIGGUM J., TAYLOR S. R., TURNER J. E., VALLISNERI M., VAN HAASTEREN R., VIGELAND S. J., WITT C. A., ZHU W. W. and COLLABORATION) T. N., *The Astrophysical Journal*, **880** (2019) 116.  
URL <https://dx.doi.org/10.3847/1538-4357/ab2236>
- [182] MINGARELLI C. M. F., LARSEN B., EISENBERG E., ZHENG Q. and HUTCHISON F., *arXiv e-prints*, (2026) arXiv:2603.05722.
- [183] CORNISH N. J. and SESANA A., *Classical and Quantum Gravity*, **30** (2013) 224005.
- [184] ALLEN B., *Phys. Rev. D*, **107** (2023) 043018.
- [185] BÉCSY B., CORNISH N. J. and KELLEY L. Z., *ApJ*, **941** (2022) 119.
- [186] XIN C., MINGARELLI C. M. F. and HAZBOUN J. S., *The Astrophysical Journal*, **915** (2021) 97.  
URL <https://doi.org/10.3847/1538-4357/2Fac01c5>
- [187] EZQUIAGA J. M., HOLZ D. E., HU W., LAGOS M. and WALD R. M., *Phys. Rev. D*, **103** (2021) 064047.

- [188] KHUSID N. M., MINGARELLI C. M. F., NATARAJAN P., CASEY-CLYDE J. A. and BARNACKA A., *ApJ*, **955** (2023) 25.
- [189] DAI L., VENUMADHAV T. and SIGURDSON K., *Phys. Rev. D*, **95** (2017) 044011.
- [190] MUZZIN A., MARCHESINI D., STEFANON M. *et al.*, *ApJ*, **777** (2013) 18.
- [191] CASEY-CLYDE J. A., MINGARELLI C. M. F., GREENE J. E., GOULDING A. D., CHEN S. and TRUMP J. R., *ApJ*, **987** (2025) 106.
- [192] REID M., LOINARD L. and MACCARONE T., *Astrometry and Long Baseline Science*, in proc. of *Science with a Next Generation Very Large Array*, Vol. 517 of *Astronomical Society of the Pacific Conference Series* 2018, p. 523.
- [193] BRISKEN W. F., MACQUART J.-P., GAO J. J., RICKETT B. J., COLES W. A., DELLER A. T., TINGAY S. J. and WEST C. J., *ApJ*, **708** (2009) 232.
- [194] DEWDNEY P. E., HALL P. J., SCHILIZZI R. T. and LAZIO T. J. L. W., *IEEE Proceedings*, **97** (2009) 1482.
- [195] BARNACKA A., *Physics Reports*, **778** (2018) 1.
- [196] CHARISI M. *et al.*, *arXiv e-prints*, (2025) .
- [197] SCHUTZ B. F., *Nature*, **323** (1986) 310.
- [198] HOLZ D. E. and HUGHES S. A., *ApJ*, **629** (2005) 15.
- [199] WANG B., HE D.-Z., WANG L.-F., LI H.-L. and ZHANG Y., *arXiv e-prints*, (2025) .
- [200] RIESS A. G., YUAN W., MACRI L. M., SCOLNIC D., BROUT D., CASERTANO S., JONES D. O., MURAKAMI Y., ANAND G. S., BREUVAL L., BRINK T. G., FILIPPENKO A. V., HOFFMANN S., JHA S. W., KENWORTHY W. D., MACKENTY J., STAHL B. E. and ZHENG W., *ApJ*, **934** (2022) L7.
- [201] PLANCK COLLABORATION, AGHANIM N. *et al.*, *A&A*, **641** (2020) A6.
- [202] CHARISI M., TAYLOR S. R., RUNNOE J., BOGDANOVIĆ T. and BURKE-SPOLAOR S., *ApJ*, **956** (2023) 1.
- [203] LEE K. J., WEX N., KRAMER M., STAPPERS B. W., BASSA C. G., JANSSEN G. H., KARUPPUSAMY R. and SMITS R., *MNRAS*, **414** (2011) 3251.
- [204] TOSCANO M., BRITTON M. C., MANCHESTER R. N., BAILES M., SANDHU J. S., KULKARNI S. R. and ANDERSON S. B., *ApJ*, **523** (1999) L171.
- [205] BRISKEN W. F., BENSON J. M., GOSS W. M. and THORSETT S. E., *ApJ*, **571** (2002) 906.
- [206] DING H., DELLER A. T., STAPPERS B. W., LAZIO T. J. W., KAPLAN D., CHATTERJEE S., BRISKEN W., CORDES J., FREIRE P. C. C., FONSECA E., STAIRS I., GUILLEMOT L., LYNE A., COGNARD I., REARDON D. J. and THEUREAU G., *MNRAS*, **519** (2023) 4982.

- [207] CORDES J. M. and LAZIO T. J. W., *ArXiv Astrophysics e-prints*, *astro-ph/0207156*, (2002) .
- [208] YAO J. M., MANCHESTER R. N. and WANG N., *ApJ*, **835** (2017) .
- [209] MORAN A., MINGARELLI C. M. F., BEDELL M., GOOD D. and SPERGEL D. N., *ApJ*, **954** (2023) 89.
- [210] OCKER S. K. and CORDES J. M., *arXiv e-prints*, (2026) arXiv:2602.11838.
- [211] JENNINGS R. J., KAPLAN D. L., CHATTERJEE S., CORDES J. M. and DELLER A. T., *ApJ*, **864** (2018) 26.
- [212] SHKLOVSKII I. S., *Nature*, **225** (1970) .
- [213] LAZARIDIS K., WEX N., JESSNER A. *et al.*, *MNRAS*, **400** (2009) .
- [214] BOYLE L. and PEN U.-L., *Phys. Rev. D*, **86** (2012) 124028.
- [215] BABAK S. and SESANA A., *Phys. Rev. D*, **85** (2012) 044034.
- [216] SESANA A. and VECCHIO A., *Phys. Rev. D*, **81** (2010) 104008.
- [217] SIEMENS X., ELLIS J., JENET F. and ROMANO J. D., *Classical and Quantum Gravity*, **30** (2013) 224015.
- [218] TSAI A. C., JOW D. L. and PEN U.-L., *arXiv e-prints*, (2025) .
- [219] DOMCKE V., FRANCIOLINI G. and PIERONI M., , (2025) .
- [220] GOLDSTEIN J. M., SESANA A., HOLGADO A. M. and VEITCH J., *Mon. Not. Roy. Astron. Soc.*, **485** (2019) 248.
- [221] PETROV P., HAZBOUN J. S., LAM M. T. and SIEMENS X., *Phys. Rev. D*, **106** (2022) 022003.
- [222] GHOSHAL A., GOUTTENOIRE Y., HEURTIER L. and SIMAKACHORN P., *Journal of High Energy Physics*, **2023** (2023) 196.
- [223] CHANG C.-F. and CUI Y., *Physics of the Dark Universe*, **29** (2020) 100604.
- [224] WEIR D. J., *Philosophical Transactions of the Royal Society A: Mathematical, Physical and Engineering Sciences*, **376** (2018) 20170126.
- [225] NERONOV A., POL A. R., CAPRINI C. and SEMIKOZ D., *Physical Review D*, **103** (2021) 041302.
- [226] BRANDENBURG A., CLARKE E., HE Y. and KAHNIASHVILI T., *Physical Review D*, **104** (2021) 043513.
- [227] FREESE K. and WINKLER M. W., *Physical Review D*, **107** (2023) 083522.
- [228] LASKY P. D., MINGARELLI C. M. F., SMITH T. L., GIBLIN J. T., THRANE E., REARDON D. J., CALDWELL R., BAILES M., BHAT N. D. R., BURKE-SPOLAOR S., DAI S., DEMPSEY J., HOBBS G., KERR M., LEVIN Y., MANCHESTER R. N., OSŁOWSKI S., RAVI V., ROSADO P. A., SHANNON R. M., SPIEWAK R., VAN STRATEN W., TOOMEY L., WANG J., WEN L., YOU X. and ZHU X., *Physical Review X*, **6** (2016) 011035.

- [229] BOYLE L. A. and STEINHARDT P. J., *Phys. Rev. D*, **77** (2005) 063504.
- [230] KAMIONKOWSKI M. and KOVETZ E. D., *Annual Review of Astronomy and Astrophysics*, **54** (2016) 227.
- [231] KHMELNITSKY A. and RUBAKOV V., *JCAP*, **2014** (2014) 019.
- [232] PORAYKO N. K. and POSTNOV K. A., *Phys. Rev. D*, **90** (2014) 062008.
- [233] PORAYKO N. K., ZHU X., LEVIN Y., HUI L., HOBBS G., GRUDSKAYA A., POSTNOV K., BAILES M., BHAT N. D. R., COLES W., DAI S., DEMPSEY J., KEITH M. J., KERR M., KRAMER M., LASKY P. D., MANCHESTER R. N., OSŁOWSKI S., PARTHASARATHY A., RAVI V., REARDON D. J., ROSADO P. A., RUSSELL C. J., SHANNON R. M., SPIEWAK R., VAN STRATEN W., TOOMEY L., WANG J., WEN L., YOU X. and PPTA COLLABORATION, *Phys. Rev. D*, **98** (2018) 102002.
- [234] BATTYE R. A., KEITH M. J., McDONALD J. I., SRINIVASAN S., STAPPERS B. W. and WELTEVREDE P., *Phys. Rev. D*, **108** (2023) 063001.
- [235] SMARRA C. *et al.*, *A&A*, **678** (2023) A50.
- [236] XUE X., DAI S., LUU H. N., LIU T., REN J., SHU J., ZHAO Y., ZIC A., BHAT N. D. R., CHEN Z.-C., FENG Y., HOBBS G., KAPUR A., MANCHESTER R. N., MANDOW R., MISHRA S., REARDON D. J., RUSSELL C. J., SHANNON R. M., WANG S., ZHANG L., ZHANG S. and ZHU X., *Physical Review Letters*, **136** (2026) 011001.
- [237] CHAMBERLIN S. J. and SIEMENS X., *Phys. Rev. D*, **85** (2012) 082001.
- [238] VALLISNERI M., TAYLOR S. R., SIMON J., FOLKNER W. M., PARK R. S., CUTLER C., ELLIS J. A., LAZIO T. J. W., VIGELAND S. J., CHATTERJEE K., CORDES J. M., LAM M. T. and HAZBOUN J. S., *ApJ*, **893** (2020) 112.
- [239] VERBIEST J. P. W., BAILES M., COLES W. A., HOBBS G. B., VAN STRATEN W., CHAMPION D. J., JENET F. A., MANCHESTER R. N., BHAT N. D. R., SARKISSIAN J. M., YARDLEY D., BURKE-SPOLAOR S., HOTAN A. W. and YOU X. P., *MNRAS*, **400** (2009) 951.
- [240] CORDES J. M., *Classical and Quantum Gravity*, **30** (2013) 224002.
- [241] HAZBOUN J. S., ROMANO J. D. and SMITH T. L., *Phys. Rev. D*, **100** (2019) 104028.
- [242] LENTATI L., SHANNON R. M., COLES W. A., VERBIEST J. P. W., VAN HAASTEREN R., ELLIS J. A., CABALLERO R. N., MANCHESTER R. N., ARZOUMANIAN Z., BABAK S., BASSA C. G., BHAT N. D. R., BREM P., BURGAY M., BURKE-SPOLAOR S., CHAMPION D., CHATTERJEE S., COGNARD I., CORDES J. M., DAI S., DEMOREST P., DESVIGNES G., DOLCH T., FERDMAN R. D., FONSECA E., GAIR J. R., GONZALEZ M. E., GRAIKOU E., GUILLEMOT L., HESSELS J. W. T., HOBBS G., JANSSEN G. H., JONES G., KARUPPUSAMY R., KEITH M., KERR M., KRAMER M., LAM M. T., LASKY P. D., LASSUS A., LAZARUS P., LAZIO T. J. W., LEE K. J., LEVIN L., LIU K., LYNCH

- R. S., MADISON D. R., MCKEE J., MCLAUGHLIN M., MCWILLIAMS S. T., MINGARELLI C. M. F., NICE D. J., OSŁOWSKI S., PENNUCCI T. T., PERERA B. B. P., PERRODIN D., PETITEAU A., POSSENTI A., RANSOM S. M., REARDON D., ROSADO P. A., SANIDAS S. A., SESANA A., SHAIFULLAH G., SIEMENS X., SMITS R., STAIRS I., STAPPERS B., STINEBRING D. R., STOVALL K., SWIGGUM J., TAYLOR S. R., THEUREAU G., TIBURZI C., TOOMEY L., VALLISNERI M., VAN STRATEN W., VECCHIO A., WANG J. B., WANG Y., YOU X. P., ZHU W. W. and ZHU X. J., *MNRAS*, **458** (2016) 2161.
- [243] CHALUMEAU A., BABAK S., PETITEAU A., CHEN S., SAMAJDAR A., CABALLERO R. N., THEUREAU G., GUILLEMOT L., DESVIGNES G., PARTHASARATHY A., LIU K., SHAIFULLAH G., HU H., VAN DER WATEREN E., ANTONIADIS J., BAK NIELSEN A. S., BASSA C. G., BERTHEREAU A., BURGAY M., CHAMPION D. J., COGNARD I., FALXA M., FERDMAN R. D., FREIRE P. C. C., GAIR J. R., GRAIKOU E., GUO Y. J., JANG J., JANSSEN G. H., KARUPPUSAMY R., KEITH M. J., KRAMER M., LEE K. J., LIU X. J., LYNE A. G., MAIN R. A., MCKEE J. W., MICKALIGER M. B., PERERA B. B. P., PERRODIN D., PORAYKO N. K., POSSENTI A., SANIDAS S. A., SESANA A., SPERI L., STAPPERS B. W., TIBURZI C., VECCHIO A., VERBIEST J. P. W., WANG J., WANG L. and XU H., *MNRAS*, **509** (2022) 5538.
- [244] HAZBOUN J. S., SIMON J., BAIER J., LARSEN B., OLIVER D. J., BAKER P. T., BÉCSY B., CHEN S., DIAZ HERNANDEZ A., ELLIS J. A., HOLGADO A. M., ISLO K., JOHNSON A., KAISER A. R., LAAL N., MCEWEN A., POL N. S., SHAPIRO KEY J., KIM M. Y., SAMSON M., SHAPIRO-ALBERT B. J., SUN J. P., TAYLOR S. R., WITT C. A., VOLPE J., YE C., BLUMER H., BROOK P. R., CHATTERJEE S., CORDES J. M., CRAWFORD F., CROMARTIE H. T., DECESAR M. E., DEMOREST P. B., DOLCH T., FERDMAN R. D., FERRARA E. C., FIORE W., FONSECA E., GARVER-DANIELS N., GENTILE P. A., GOOD D. C., JENNINGS R. J., JONES M. L., KAPLAN D. L., LAM M. T., LAZIO T. J. W., LORIMER D. R., LUO J., LYNCH R. S., MADISON D. R., MCLAUGHLIN M. A., MINGARELLI C. M. F., NG C., NICE D. J., PENNUCCI T. T., RANSOM S. M., RAY P. S., SIEMENS X., SPIEWAK R., STAIRS I. H., STINEBRING D. R., STOVALL K., SWIGGUM J. K., TURNER J. E., VALLISNERI M. and VIGELAND S. J., *arXiv e-prints*, (2025) arXiv:2511.22597.
- [245] HAZBOUN J. S., SIMON J., TAYLOR S. R., LAM M. T., VIGELAND S. J., ISLO K., KEY J. S., ARZOUMANIAN Z., BAKER P. T., BRAZIER A., BROOK P. R., BURKE-SPOLAOR S., CHATTERJEE S., CORDES J. M., CORNISH N. J., CRAWFORD F., CROWTER K., CROMARTIE H. T., DECESAR M., DEMOREST P. B., DOLCH T., ELLIS J. A., FERDMAN R. D., FERRARA E., FONSECA E., GARVER-DANIELS N., GENTILE P., GOOD D., HOLGADO A. M., HUERTA E. A., JENNINGS R., JONES G., JONES M. L., KAISER A. R., KAPLAN D. L., KELLEY L. Z., LAZIO T. J. W., LEVIN L., LOMMEN A. N., LORIMER D. R., LUO J., LYNCH R. S., MADISON D. R., MCLAUGHLIN M. A., MCWILLIAMS S. T., MINGARELLI C. M. F., NG C., NICE D. J., PENNUCCI T. T., POL N. S., RANSOM S. M., RAY P. S., SIEMENS X., SPIEWAK R., STAIRS I. H., STINEBRING D. R., STOVALL K., SWIGGUM J., TURNER J. E., VALLISNERI M., VAN HAASTEREN R., WITT C. A. and ZHU W. W., *ApJ*, **890** (2020) 108.

- [246] ZIC A., HOBBS G., SHANNON R. M., REARDON D., GONCHAROV B., BHAT N. D. R., CAMERON A., DAI S., DAWSON J. R., KERR M., MANCHESTER R. N., MANDOW R., MARSHMAN T., RUSSELL C. J., THYAGARAJAN N. and ZHU X. J., *MNRAS*, **516** (2022) 410.
- [247] GONCHAROV B. and SARDANA S., *MNRAS*, (2025) .
- [248] VAN HAASTEREN R., *ApJS*, **273** (2024) 23.
- [249] JONES M. L., McLAUGHLIN M. A., LAM M. T., CORDES J. M., LEVIN L., CHATTERJEE S., ARZOUMANIAN Z., CROWTER K., DEMOREST P. B., DOLCH T., ELLIS J. A., FERDMAN R. D., FONSECA E., GONZALEZ M. E., JONES G., LAZIO T. J. W., NICE D. J., PENNUCCI T. T., RANSOM S. M., STINEBRING D. R., STAIRS I. H., STOVALL K., SWIGGUM J. K. and ZHU W. W., *ApJ*, **841** (2017) 125.
- [250] HAZBOUN J. S., SIMON J., MADISON D. R., ARZOUMANIAN Z., CROMARTIE H. T., CROWTER K., DECESAR M. E., DEMOREST P. B., DOLCH T., ELLIS J. A., FERDMAN R. D., FERRARA E. C., FONSECA E., GENTILE P. A., JONES G., JONES M. L., LAM M. T., LEVIN L., LORIMER D. R., LYNCH R. S., McLAUGHLIN M. A., NG C., NICE D. J., PENNUCCI T. T., RANSOM S. M., RAY P. S., SPIEWAK R., STAIRS I. H., STOVALL K., SWIGGUM J. K., ZHU W. and THE NANOGRV COLLABORATION, *ApJ*, **929** (2022) 39.
- [251] SUSARLA S. C., CHALUMEAU A., TIBURZI C., KEANE E. F., VERBIEST J. P. W., HAZBOUN J. S., KRISHNAKUMAR M. A., IRACI F., SHAIFULLAH G. M., GOLDEN A., BAK NIELSEN A.-S., DONNER J., GRIESSMEIER J.-M., KEITH M. J., OSŁOWSKI S., PORAYKO N. K., SERYLAK M., ANDERSON J. M., BRÜGGEN M., CIARDI B., DETTMAR R.-J., HOEFT M., KÜNSEMÖLLER J., SCHWARZ D. and VOCKS C., *A&A*, **692** (2024) A18.
- [252] CORDES J. M. and SHANNON R. M., *arXiv e-prints*, (2010) arXiv:1010.3785.
- [253] ALAM M. F., ARZOUMANIAN Z., BAKER P. T., BLUMER H., BOHLER K. E., BRAZIER A., BROOK P. R., BURKE-SPOLAOR S., CABALLERO K., CAMUCCIO R. S., CHAMBERLAIN R. L., CHATTERJEE S., CORDES J. M., CORNISH N. J., CRAWFORD F., CROMARTIE H. T., DECESAR M. E., DEMOREST P. B., DOLCH T., ELLIS J. A., FERDMAN R. D., FERRARA E. C., FIORE W., FONSECA E., GARCIA Y., GARVER-DANIELS N., GENTILE P. A., GOOD D. C., GUSDORFF J. A., HALMRAST D., HAZBOUN J. S., ISLO K., JENNINGS R. J., JESSUP C., JONES M. L., KAISER A. R., KAPLAN D. L., KELLEY L. Z., KEY J. S., LAM M. T., LAZIO T. J. W., LORIMER D. R., LUO J., LYNCH R. S., MADISON D. R., MARACCINI K., McLAUGHLIN M. A., MINGARELLI C. M. F., NG C., NGUYEN B. M. X., NICE D. J., PENNUCCI T. T., POL N. S., RAMETTE J., RANSOM S. M., RAY P. S., SHAPIRO-ALBERT B. J., SIEMENS X., SIMON J., SPIEWAK R., STAIRS I. H., STINEBRING D. R., STOVALL K., SWIGGUM J. K., TAYLOR S. R., TRIPEPI M., VALLISNERI M., VIGELAND S. J., WITT C. A., ZHU W. and NANOGRV COLLABORATION, *ApJS*, **252** (2021) 5.
- [254] AGAZIE G., ALAM M. F., ANUMARLAPUDI A., ARCHIBALD A. M., ARZOUMANIAN Z., BAKER P. T., BLECHA L., BONIDIE V., BRAZIER A., BROOK P. R.,

- BURKE-SPOLAOR S., BÉCSY B., CHAPMAN C., CHARISI M., CHATTERJEE S., COHEN T., CORDES J. M., CORNISH N. J., CRAWFORD F., CROMARTIE H. T., CROWTER K., DECESAR M. E., DEMOREST P. B., DOLCH T., DRACHLER B., FERRARA E. C., FIORE W., FONSECA E., FREEDMAN G. E., GARVER-DANIELS N., GENTILE P. A., GLASER J., GOOD D. C., GÜLTEKIN K., HAZBOUN J. S., JENNINGS R. J., JESSUP C., JOHNSON A. D., JONES M. L., KAISER A. R., KAPLAN D. L., KELLEY L. Z., KERR M., KEY J. S., KUSKE A., LAAL N., LAM M. T., LAMB W. G., LAZIO T. J. W., LEWANDOWSKA N., LIN Y., LIU T., LORIMER D. R., LUO J., LYNCH R. S., MA C.-P., MADISON D. R., MARACINI K., MCEWEN A., MCKEE J. W., MCLAUGHLIN M. A., MCMANN N., MEYERS B. W., MINGARELLI C. M. F., MITRIDATE A., NG C., NICE D. J., OCKER S. K., OLUM K. D., PANCIU E., PENNUCCI T. T., PERERA B. B. P., POL N. S., RADOVAN H. A., RANSOM S. M., RAY P. S., ROMANO J. D., SALO L., SARDESAI S. C., SCHMIEDEKAMP C., SCHMIEDEKAMP A., SCHMITZ K., SHAPIRO-ALBERT B. J., SIEMENS X., SIMON J., SIWEK M. S., STAIRS I. H., STINEBRING D. R., STOVALL K., SUSOBHANAN A., SWIGGUM J. K., TAYLOR S. R., TURNER J. E., UNAL C., VALLISNERI M., VIGELAND S. J., WAHL H. M., WANG Q., WITT C. A., YOUNG O. and NANOGRAV COLLABORATION, *ApJ*, **951** (2023) L9.
- [255] LAM M. T., CORDES J. M., CHATTERJEE S. and DOLCH T., *ApJ*, **801** (2015) 130.
- [256] VALENTINA SOSA FISCELLA S., LAM M. T., ARZOUMANIAN Z., BLUMER H., BROOK P. R., CROMARTIE H. T., DECESAR M. E., DEMOREST P. B., DOLCH T., ELLIS J. A., FERDMAN R. D., FERRARA E. C., FONSECA E., GARVER-DANIELS N., GENTILE P. A., GOOD D. C., JONES M. L., LORIMER D. R., LUO J., LYNCH R. S., MCLAUGHLIN M. A., NG C., NICE D. J., PENNUCCI T. T., POL N. S., RANSOM S. M., SPIEWAK R., STAIRS I. H., STOVALL K., SWIGGUM J. K. and VIGELAND S. J., *Astrophys. J.*, **966** (2024) 95.
- [257] LARSEN B., MINGARELLI C. M. F., HAZBOUN J. S., CHALUMEAU A., GOOD D. C., SIMON J., AGAZIE G., ANUMARLAPUDI A., ARCHIBALD A. M., ARZOUMANIAN Z., BAKER P. T., BROOK P. R., CROMARTIE H. T., CROWTER K., DECESAR M. E., DEMOREST P. B., DOLCH T., FERRARA E. C., FIORE W., FONSECA E., FREEDMAN G. E., GARVER-DANIELS N., GENTILE P. A., GLASER J., JENNINGS R. J., JONES M. L., KAPLAN D. L., KERR M., LAM M. T., LORIMER D. R., LUO J., LYNCH R. S., MCEWEN A., MCLAUGHLIN M. A., MCMANN N., MEYERS B. W., NG C., NICE D. J., PENNUCCI T. T., PERERA B. B. P., POL N. S., RADOVAN H. A., RANSOM S. M., RAY P. S., SCHMIEDEKAMP A., SCHMIEDEKAMP C., SHAPIRO-ALBERT B. J., STAIRS I. H., STOVALL K., SUSOBHANAN A., SWIGGUM J. K., WAHL H. M., CHAMPION D. J., COGNARD I., GUILLEMOT L., HU H., KEITH M. J., LIU K., MCKEE J. W., PARTHASARATHY A., PERRODIN D., POSSENTI A., SHAIFULLAH G. M. and THEUREAU G., *ApJ*, **972** (2024) 49.
- [258] RANKIN J. M. and ROBERTS J. A., *Time Variability of the Dispersion of the Crab Nebula Pulsar*, in proc. of *The Crab Nebula*, edited by DAVIES R. D. and GRAHAM-SMITH F., Vol. 46 1971, p. 114.

- [259] KEITH M. J., COLES W., SHANNON R. M., HOBBS G. B., MANCHESTER R. N., BAILES M., BHAT N. D. R., BURKE-SPOLAOR S., CHAMPION D. J., CHAUDHARY A., HOTAN A. W., KHOO J., KOCZ J., OSŁOWSKI S., RAVI V., REYNOLDS J. E., SARKISSIAN J., VAN STRATEN W. and YARDLEY D. R. B., *MNRAS*, **429** (2013) 2161.
- [260] DEMOREST P. B., FERDMAN R. D., GONZALEZ M. E., NICE D., RANSOM S., STAIRS I. H., ARZOUMANIAN Z., BRAZIER A., BURKE-SPOLAOR S., CHAMBERLIN S. J., CORDES J. M., ELLIS J., FINN L. S., FREIRE P., GIAMPANIS S., JENET F., KASPI V. M., LAZIO J., LOMMEN A. N., MCCLAUGHLIN M., PALLIYAGURU N., PERRODIN D., SHANNON R. M., SIEMENS X., STINEBRING D., SWIGGUM J. and ZHU W. W., *ApJ*, **762** (2013) 94.
- [261] LENTATI L., ALEXANDER P., HOBSON M. P., FERROZ F., VAN HAASTEREN R., LEE K. J. and SHANNON R. M., *MNRAS*, **437** (2014) 3004.
- [262] VAN HAASTEREN R. and VALLISNERI M., *Phys. Rev. D*, **90** (2014) 104012.
- [263] PENNUCCI T. T., DEMOREST P. B. and RANSOM S. M., *ApJ*, **790** (2014) 93.
- [264] CURYŁO M., PENNUCCI T. T., BAILES M., BHAT N. D. R., CAMERON A. D., DAI S., HOBBS G., KAPUR A., MANCHESTER R. N., MANDOW R., MILES M. T., RUSSELL C. J., REARDON D. J., SHANNON R. M., SPIEWAK R., VAN STRATEN W., ZHU X.-J. and ZIC A., *ApJ*, **944** (2023) 128.
- [265] IRACI F., CHALUMEAU A., TIBURZI C., VERBIEST J. P. W., POSSENTI A., SHAIFULLAH G. M., SUSARLA S. C., KRISHNAKUMAR M. A., LAM M. T., CROMARTIE H. T., KERR M. and GRIESSMEIER J.-M., *A&A*, **692** (2024) A170.
- [266] GITIKA P., SHANNON R. M., BAILES M., REARDON D. J., MILES M. T., CHAMPION D. J. and GRUNTHAL K., *PASA*, **42** (2025) e146.
- [267] REARDON D. J., ZIC A., SHANNON R. M., DI MARCO V., HOBBS G. B., KAPUR A., LOWER M. E., MANDOW R., MIDDLETON H., MILES M. T., ROGERS A. F., ASKEW J., BAILES M., BHAT N. D. R., CAMERON A., KERR M., KULKARNI A., MANCHESTER R. N., NATHAN R. S., RUSSELL C. J., OSŁOWSKI S. and ZHU X.-J., *ApJ*, **951** (2023) L7.
- [268] IRACI F., CHALUMEAU A., TIBURZI C., VERBIEST J. P. W., POSSENTI A., SUSARLA S. C., KRISHNAKUMAR M. A., SHAIFULLAH G. M., ANTONIADIS J., BAGCHI M., BASSA C., CABALLERO R. N., CECCONI B., CHEN S., CHOWDHURY S., CIARDI B., COGNARD I., CORBEL S., DESAI S., DEB D., GIRARD J., GOLDEN A., GRIESSMEIER J.-M., GUILLEMOT L., HOEFT M., HU H., JANKOWSKI F., JANSSEN G., JOSHI B. C., KALA S., KEANE E., NOBLESON K., KONOVALENKO A., KRAVTSOV I., KRAMER M., LIU K., PARTHASARATHY A., RANA P., SCHWARZ D., SINGHA J., SRIVASTAVA A., TAKAHASHI K., TARAFDAR P., THEUREAU G., ULYANOV O., VOCKS C., WANG J., ZAKHARENKO V. and ZARKA P., *A&A*, **704** (2025) A109.
- [269] LARSEN B., BAIER J. *et al.*, *in preparation*, (2026), nANOGrav Collaboration.

- [270] SHANNON R. M., LENTATI L. T., KERR M., MANCHESTER R. N., HOBBS G., BAILES M., BHAT N. D. R., BURKE-SPOLAOR S., COLES W., DAI S., KEITH M. J., LEVIN Y., OSŁOWSKI S., RAVI V., REARDON D. J., RUSSELL C. J., TOOMEY L., VAN STRATEN W., WEN L., YOU X. P. and ZHU X.-J., *ApJ*, **828** (2016) L1.
- [271] LAM M. T., ELLIS J. A., GRILLO G., JONES M. L., HAZBOUN J. S., BROOK P. R., TURNER J. E., CHATTERJEE S., CORDES J. M., LAZIO T. J. W., DECESAR M. E., ARZOUMANIAN Z., BLUMER H., CROMARTIE H. T., DEMOREST P. B., DOLCH T., FERDMAN R. D., FERRARA E. C., FONSECA E., GARVER-DANIELS N., GENTILE P. A., GUPTA V., LORIMER D. R., LYNCH R. S., MADISON D. R., McLAUGHLIN M. A., NG C., NICE D. J., PENNUCCI T. T., RANSOM S. M., SPIEWAK R., STAIRS I. H., STINEBRING D. R., STOVALL K., SWIGGUM J. K., VIGELAND S. J. and ZHU W. W., *ApJ*, **861** (2018) 132.
- [272] CORDES J. M. and RICKETT B. J., *ApJ*, **507** (1998) 846.
- [273] HEMBERGER D. A. and STINEBRING D. R., *ApJ*, **674** (2008) L37.
- [274] SHANNON R. M. and CORDES J. M., *MNRAS*, **464** (2017) 2075.
- [275] GEIGER A., CORDES J. M., LAM M. T., OCKER S. K., CHATTERJEE S., ARZOUMANIAN Z., BATTAGLIA A. L., BLUMER H., BROOK P. R., COMBS O. A., CROMARTIE H. T., DECESAR M. E., DEMOREST P. B., DOLCH T., ELLIS J. A., FERDMAN R. D., FERRARA E. C., FONSECA E., GARVER-DANIELS N., GENTILE P. A., GOOD D. C., JONES M. L., LORIMER D. R., LUO J., LYNCH R. S., McLAUGHLIN M. A., NG C., NICE D. J., PENNUCCI T. T., POL N. S., RANSOM S. M., SPIEWAK R., STAIRS I. H., STOVALL K., SWIGGUM J. K. and VIGELAND S. J., *ApJ*, **986** (2025) 191.
- [276] LENTATI L., KERR M., DAI S., SHANNON R. M., HOBBS G. and OSŁOWSKI S., *MNRAS*, **468** (2017) 1474.
- [277] KULKARNI A. D., SHANNON R. M., REARDON D. J. and MILES M. T., *arXiv e-prints*, (2025) arXiv:2511.03185.
- [278] CORDES J. M., OCKER S. K., CHATTERJEE S., DOLCH T., JENNINGS R. J., LAM M. T. and TURNER J. E., , (2026) , in preparation.
- [279] YOUNG O. and LAM M., *arXiv e-prints*, (2023) arXiv:2306.06046.
- [280] DEMOREST P. B., *MNRAS*, **416** (2011) 2821.
- [281] DOLCH T., STINEBRING D. R., JONES G., ZHU H., LYNCH R. S., COHEN T., DEMOREST P. B., LAM M. T., LEVIN L., McLAUGHLIN M. A. and PALLIYAGURU N. T., *ApJ*, **913** (2021) 98.
- [282] TURNER J. E., STINEBRING D. R., McLAUGHLIN M. A., ARCHIBALD A. M., DOLCH T. and LYNCH R. S., *ApJ*, **944** (2023) 191.
- [283] STINEBRING D., *Classical and Quantum Gravity*, **30** (2013) 224006.
- [284] CORDES J. M., SHANNON R. M. and STINEBRING D. R., *ApJ*, **817** (2016) .

- [285] CHENG K. S., *ApJ*, **321** (1987) 799.
- [286] LYNE A., HOBBS G., KRAMER M., STAIRS I. and STAPPERS B., *Science*, **329** (2010) 408.
- [287] JONES P. B., *MNRAS*, **246** (1990) 364.
- [288] MELATOS A. and LINK B., *MNRAS*, **437** (2014) 21.
- [289] SHANNON R. M., CORDES J. M., METCALFE T. S., LAZIO T. J. W., COGNARD I., DESVIGNES G., JANSSEN G. H., JESSNER A., KRAMER M., LAZARIDIS K., PURVER M. B., STAPPERS B. W. and THEUREAU G., *ApJ*, **766** (2013) 5.
- [290] JENNINGS R. J., CORDES J. M. and CHATTERJEE S., *ApJ*, **904** (2020) 191.
- [291] LAM M. T., CORDES J. M., CHATTERJEE S., ARZOUManIAN Z., CROWTER K., DEMOREST P. B., DOLCH T., ELLIS J. A., FERDMAN R. D., FONSECA E., GONZALEZ M. E., JONES G., JONES M. L., LEVIN L., MADISON D. R., McLAUGHLIN M. A., NICE D. J., PENNUCCI T. T., RANSOM S. M., SHANNON R. M., SIEMENS X., STAIRS I. H., STOVALL K., SWIGGUM J. K. and ZHU W. W., *The Astrophysical Journal*, **834** (2017) 35, aDS Bibcode: 2017ApJ...834...35L. URL <https://ui.adsabs.harvard.edu/abs/2017ApJ...834...35L>
- [292] SRIVASTAVA A., DESAI S., KOLHE N., SURNIS M., JOSHI B. C., SUSOBHANAN A., CHALUMEAU A., HISANO S., NOBLESON K., ARUMUGAM S., KHARBANDA D., SINGHA J., TARAFDAR P., ARUMUGAM P., BAGCHI M., BATHULA A., DANDAPAT S., DEY L., DWIVEDI C., GIRGAONKAR R., GOPAKUMAR A., GUPTA Y., KIKUNAGA T., KRISHNAKUMAR M. A., LIU K., MAAN Y., MANOHARAN P. K., PALADI A. K., RANA P., SHAIFULLAH G. M. and TAKAHASHI K., *Phys. Rev. D*, **108** (2023) 023008.
- [293] NOBLESON K., DWIVEDI C., DESAI S., JOSHI B. C., GROVER H., DEB D., VYASRAJ V., VARA K., TAHBILDAR H., SUSOBHANAN A., SURNIS M., SRIVASTAVA A., SARDANA S., TAKAHASHI K., AMARNATH, ARUMUGAM P., BAGCHI M., DHANDA BATRA N., CHAKRABORTY M., CHOWDHURY S., JACOB S. J., JOSE J., KALA S., KATO R., KRISHNAKUMAR M. A., MEENA K., PALADI A. K., PANDIAN A., RAI K., RANA P., SINGH M., SINGHA J., SHUKLA A., TARAFDAR P., THIAGRAJ P. and ZURAIQ Z., *arXiv e-prints*, (2025) arXiv:2512.20455.
- [294] ANTONIADIS J., BABAK S., BAK NIELSEN A. S., BASSA C. G., BERTHEREAU A., BONETTI M., BORTOLAS E., BROOK P. R., BURGAY M., CABALLERO R. N., CHALUMEAU A., CHAMPION D. J., CHANLARIDIS S., CHEN S., COGNARD I., DESVIGNES G., FALXA M., FERDMAN R. D., FRANCHINI A., GAIR J. R., GONCHAROV B., GRAIKOU E., GRIESSMEIER J. M., GUILLEMOT L., GUO Y. J., HU H., IRACI F., IZQUIERDO-VILLALBA D., JANG J., JAWOR J., JANSSEN G. H., JESSNER A., KARUPPUSAMY R., KEANE E. F., KEITH M. J., KRAMER M., KRISHNAKUMAR M. A., LACKEOS K., LEE K. J., LIU K., LIU Y., LYNE A. G., MCKEE J. W., MAIN R. A., MICKALIGER M. B., NITU I. C., PARTHASARATHY A., PERERA B. B. P., PERRODIN D., PETITEAU A., PORAYKO N. K., POSSENTI A., SAMAJDAR H. Q. L. A., SANIDAS S. A., SESANA A., SHAIFULLAH G., SPERI L., SPIEWAK R., STAPPERS B. W., SUSARLA S. C., THEUREAU G., TIBURZI C., VAN DER WATEREN E., VECCHIO A., VENKATRAMAN KRISHNAN V., VERBIEST J. P. W., WANG J., WANG L. and WU Z., *Astron. Astrophys.*, **678** (2023) A48.

- [295] ZIC A., REARDON D. J., KAPUR A., HOBBS G., MANDOW R., CURYLO M., SHANNON R. M., ASKEW J., BAILES M., BHAT N. D. R., CAMERON A., CHEN Z.-C., DAI S., DI MARCO V., FENG Y., KERR M., KULKARNI A., LOWER M. E., LUO R., MANCHESTER R. N., MILES M. T., NATHAN R. S., OSŁOWSKI S., ROGERS A. F., RUSSELL C. J., SPIEWAK R., THYAGARAJAN N., TOOMEY L., WANG S., ZHANG L., ZHANG S. and ZHU X.-J., *Publ. Astron. Soc. Aust.*, **40** (2023) e049.
- [296] HOBBS G., GUO L., CABALLERO R. N., COLES W., LEE K. J., MANCHESTER R. N., REARDON D. J., MATSAKIS D., TONG M. L., ARZOUMANIAN Z. *et al.*, *MNRAS*, **491** (2020) 5951.
- [297] CABALLERO R. N., GUO Y. J., LEE K. J., LAZARUS P., CHAMPION D. J., DESVIGNES G., KRAMER M., PLANT K., ARZOUMANIAN Z., BAILES M. *et al.*, *MNRAS*, **481** (2018) 5501.
- [298] ELLIS J., SIEMENS X. and CHAMBERLIN S., *arXiv e-prints*, (2012) .
- [299] VAN HAASTEREN R., MINGARELLI C. M. F., VECCHIO A. and LASSUS A., *arXiv e-prints*, (2013) .
- [300] TAYLOR S. R., GAIR J. R. and LENTATI L., *Phys. Rev. D*, **87** (2013) .
- [301] HAZBOUN J. S., MINGARELLI C. M. F. and LEE K., *arXiv e-prints*, (2018) .
- [302] BAKER P. T., BROOK P. R., FIORE W. C., GARVER-DANIELS N., KAISER A. R., LAM M. T., SHAPIRO-ALBERT B. J. and WITT C. A., *arXiv e-prints*, (2019) .
- [303] VERBIEST ET AL. J. P. W., *Monthly Notices of the Royal Astronomical Society*, **458** (2016) 1267.
- [304] PERERA B. B. P., DECESAR M., DEMOREST P. B. *et al.*, *MNRAS*, **490** (2019) .
- [305] THE INTERNATIONAL PULSAR TIMING ARRAY COLLABORATION, AGAZIE G., ANTONIADIS J., ANUMARLAPUDI A., ARCHIBALD A. M., ARUMUGAM P., ARUMUGAM S., ARZOUMANIAN Z., ASKEW J., BABAK S., BAGCHI M., BAILES M., BAK NIELSEN A. S., BAKER P. T., BASSA C. G., BATHULA A., BÉCSY B., BERTHEREAU A., BHAT N. D. R., BLECHA L., BONETTI M., BORTOLAS E., BRAZIER A., BROOK P. R., BURGAY M., BURKE-SPOLAOR S., BURNETTE R., CABALLERO R. N., CAMERON A., CASE R., CHALUMEAU A., CHAMPION D. J., CHANLARIDIS S., CHARISI M., CHATTERJEE S., CHATZIOANNOU K., CHEESEBORO B. D., CHEN S., CHEN Z. C., COGNARD I., COHEN T., COLES W. A., CORDES J. M., CORNISH N. J., CRAWFORD F., CROMARTIE H. T., CROWTER K., CURYLO M., CUTLER C. J., DAI S., DANDAPAT S., DEB D., DECESAR M. E., DEGAN D., DEMOREST P. B., DENG H., DESAI S., DESVIGNES G., DEY L., DHANDA-BATRA N., DI MARCO V., DOLCH T., DRACHLER B., DWIVEDI C., ELLIS J. A., FALXA M., FENG Y., FERDMAN R. D., FERRARA E. C., FIORE W., FONSECA E., FRANCHINI A., FREEDMAN G. E., GAIR J. R., GARVER-DANIELS N., GENTILE P. A., GERSBACH K. A., GLASER J., GOOD D. C., GONCHAROV B., GOPAKUMAR A., GRAIKOU E., GRIESSMEIER J. M., GUILLEMOT L., GÜLTEKIN K., GUO Y. J., GUPTA Y., GRUNTHAL K., HAZBOUN J. S., HISANO

- S., HOBBS G. B., HOURIHANE S., HU H., IRACI F., ISLO K., IZQUIERDO-VILLALBA D., JANG J., JAWOR J., JANSSEN G. H., JENNINGS R. J., JESSNER A., JOHNSON A. D., JONES M. L., JOSHI B. C., KAISER A. R., KAPLAN D. L., KAPUR A., KAREEM F., KARUPPUSAMY R., KEANE E. F., KEITH M. J., KELLEY L. Z., KERR M., KEY J. S., KHARBANDA D., KIKUNAGA T., KLEIN T. C., KOLHE N., KRAMER M., KRISHNAKUMAR M. A., KULKARNI A., LAAL N., LACKEOS K., LAM M. T., LAMB W. G., LARSEN B. B., LAZIO T. J. W., LEE K. J., LEVIN Y., LEWANDOWSKA N., LITTENBERG T. B., LIU K., LIU T., LIU Y., LOMMEN A., LORIMER D. R., LOWER M. E., LUO J., LUO R., LYNCH R. S., LYNE A. G., MA C. P., MAAN Y., MADISON D. R., MAIN R. A., MANCHESTER R. N., MANDOW R., MATTSON M. A., MCEWEN A., MCKEE J. W., MCLAUGHLIN M. A., MCMANN N., MEYERS B. W., MEYERS P. M., MICKALIGER M. B., MILES M., MINGARELLI C. M. F., MITRIDATE A., NATARAJAN P., NATHAN R. S., NG C., NICE D. J., NIȚU I. C., NOBLESON K., OCKER S. K., OLUM K. D., OSŁOWSKI S., PALADI A. K., PARTHASARATHY A., PENNUCCI T. T., PERERA B. B. P., PERRODIN D., PETITEAU A., PETROV P., POL N. S., PORAYKO N. K., POSSENTI A., PRABU T., QUELQUEJAY LECLERE H., RADOVAN H. A., RANA P., RANSOM S. M., RAY P. S., REARDON D. J., ROGERS A. F., ROMANO J. D., RUSSELL C. J., SAMAJDAR A., SANIDAS S. A., SARDESAI S. C., SCHMIEDEKAMP A., SCHMIEDEKAMP C., SCHMITZ K., SCHULT L., SESANA A., SHAIFULLAH G., SHANNON R. M., SHAPIRO-ALBERT B. J., SIEMENS X., SIMON J., SINGHA J., SIWEK M. S., SPERI L., SPIEWAK R., SRIVASTAVA A., STAIRS I. H., STAPPERS B. W., STINEBRING D. R., STOVALL K., SUN J. P., SURNIS M., SUSARLA S. C., SUSOBHANAN A., SWIGGUM J. K., TAKAHASHI K., TARAFDAR P., TAYLOR J., TAYLOR S. R., THEUREAU G., THRANE E., THYAGARAJAN N., TIBURZI C., TOOMEY L., TURNER J. E., UNAL C., VALLISNERI M., VAN DER WATEREN E., VAN HAASTEREN R., VECCHIO A., VENKATRAMAN KRISHNAN V., VERBIEST J. P. W., VIGELAND S. J., WAHL H. M., WANG S., WANG Q., WITT C. A., WANG J., WANG L., WAYT K. E., WU Z., YOUNG O., ZHANG L., ZHANG S., ZHU X. J. and ZIC A., *Astrophys. J.*, **966** (2024) 105.
- [306] ELLIS J. A., SIEMENS X. and CREIGHTON J. D. E., *The Astrophysical Journal*, **756** (2012) 175.  
URL <https://dx.doi.org/10.1088/0004-637X/756/2/175>
- [307] VAN HAASTEREN R. and LEVIN Y., *MNRAS*, **401** (2010) 2372.
- [308] MADISON D. R., CORDES J. M. and CHATTERJEE S., *ApJ*, **788** (2014) 141.
- [309] DESVIGNES G., CABALLERO R. N., LENTATI L., VERBIEST J. P. W., CHAMPION D. J., STAPPERS B. W., JANSSEN G. H., LAZARUS P., OSŁOWSKI S., BABAK S., BASSA C. G., BREM P., BURGAY M., COGNARD I., GAIR J. R., GRAIKOU E., GUILLEMOT L., HESSELS J. W. T., JESSNER A., JORDAN C., KARUPPUSAMY R., KRAMER M., LASSUS A., LAZARIDIS K., LEE K. J., LIU K., LYNE A. G., MCKEE J., MINGARELLI C. M. F., PERRODIN D., PETITEAU A., POSSENTI A., PURVER M. B., ROSADO P. A., SANIDAS S., SESANA A., SHAIFULLAH G., SMITS R., TAYLOR S. R., THEUREAU G., TIBURZI C., VAN HAASTEREN R. and VECCHIO A., *MNRAS*, **458** (2016) 3341.
- [310] LENTATI L., KERR M., DAI S., HOBSON M. P., SHANNON R. M., HOBBS G. *et al.*, *MNRAS*, **466** (2017) 3706.

- [311] NOBLESON K., AGARWAL N., GIRGAONKAR R. *et al.*, *MNRAS*, **512** (2022) 1234.
- [312] SHARMA S. S., ROY J., BHATTACHARYYA B. *et al.*, *ApJ*, **936** (2022) .
- [313] AGAZIE G., KAPLAN D. L., SUSOBHANAN A. *et al.*, *arXiv e-prints*, (2025) .
- [314] SUSOBHANAN A., *Phys. Rev. D*, **112** (2025) .
- [315] SUSOBHANAN A., PALADI A. K., DESMECHT R. *et al.*, *arXiv e-prints*, (2025) .
- [316] LARSEN B., MINGARELLI C. M. F., BAKER P. T., HAZBOUN J. S., CHEN S., SCHULT L., TAYLOR S. R., SIMON J., ANTONIADIS J., BAIER J., CABALLERO R. N., CHALUMEAU A., CHEN Z., COGNARD I., DEB D., DI MARCO V., DOLCH T., EYA I. O., FERRARA E. C., GERSBACH K. A., GOOD D. C., HU H., KAPUR A., KALA S., KRAMER M., LAM M. T., LAMB W. G., LAZIO T. J. W., LIU K., LIU Y., MCLAUGHLIN M., NICE D. J., PERERA B. B. P., PETITEAU A., RANSOM S. M., REARDON D. J., RUSSELL C. J., SHAIFULLAH G. M., SPERI L., SRIVASTAVA A., THEUREAU G., WANG J. and ZHANG L., *MNRAS*, **542** (2025) 3028.
- [317] WRIGHT D., WAYT K., HAZBOUN J. S., SIEMENS X., VAN HAASTEREN R., SCHULT L. and TAYLOR S. R., *arXiv e-prints*, (2025) arXiv:2512.14807.
- [318] VALTOLINA S. and VAN HAASTEREN R., *arXiv e-prints*, (2024) arXiv:2412.11894.
- [319] LAAL N., TAYLOR S. R., VAN HAASTEREN R. *et al.*, *arXiv e-prints*, (2024) arXiv:2410.11944.
- [320] COLLABORATION P., *Astronomy & Astrophysics*, **641** (2020) A10.  
URL <https://arxiv.org/abs/1807.06211>
- [321] MOORE C. J. and VECCHIO A., *Nature Astronomy*, **5** (2021) 1268.
- [322] LIDDLE A. R. and LYTH D. H., *Cosmological Inflation and Large-Scale Structure* (Cambridge University Press) 2000.
- [323] DEROCO W. and DROR J. A., *Physical Review D*, **107** (2023) 123508.  
URL <https://arxiv.org/abs/2304.13042>
- [324] DEROCO W. and DROR J. A., *Physical Review Letters*, **132** (2024) 101403.  
URL <https://arxiv.org/abs/2212.09751>
- [325] ZHENG Q., MINGARELLI C. M. F., DEROCO W., NAY J., BODDY K. K. and DROR J. A., *Phys. Rev. D*, **113** (2026) 023037.
- [326] BELL J. F. and BAILES M., *ApJ*, **456** (1996) .
- [327] SHAPIRO I. I., *Phys. Rev. Lett.*, **13** (1964) 789.
- [328] CHAKRABARTI S., CHANG P., LAM M. T., VIGELAND S. J. and QUILLEN A. C., *ApJL*, **907** (2021) L26.
- [329] MORAN A., MINGARELLI C. M. F., VAN TILBURG K. and GOOD D., *Phys. Rev. D*, **109** (2024) 123015.

- [330] RAVI A., LANGELLIER N., PHILLIPS D. F., BUSCHMANN M., SAFDI B. R. and WALSWORTH R. L., *Phys. Rev. Lett.*, **123** (2019) 091101.
- [331] KIPPER R., TENJES P., TEMPEL E. and DE PROPRIIS R., *MNRAS*, **506** (2021) 5559.
- [332] HOLMBERG J. and FLYNN C., *MNRAS*, **313** (2000) 209.
- [333] CREZE M., CHEREUL E., BIENAYME O. and PICHON C., *A&A*, **329** (1998) 920.
- [334] MATT C., GÜLTEKIN K., KELLEY L. Z., BLECHA L., SIMON J., AGAZIE G., ANUMARLAPUDI A., ARCHIBALD A. M., ARZOUMANIAN Z., BAIER J. G., BAKER P. T., BÉCSY B., BRAZIER A., BROOK P. R., BURKE-SPOLAOR S., BURNETTE R., CASE R., CASEY-CLYDE J. A., CHARISI M., CHATTERJEE S., COHEN T., CORDES J. M., CORNISH N. J., CRAWFORD F., CROMARTIE H. T., CROWTER K., DECESAR M. E., DEMOREST P. B., DENG H., DEY L., DOLCH T., FERRARA E. C., FIORE W., FONSECA E., FREEDMAN G. E., GARDINER E. C., GARVER-DANIELS N., GENTILE P. A., GERSBACH K. A., GLASER J., GOOD D. C., HARRIS C. J., HAZBOUN J. S., JENNINGS R. J., JOHNSON A. D., JONES M. L., KAPLAN D. L., KERR M., KEY J. S., LAAL N., LAM M. T., LAMB W. G., LARSEN B., LAZIO T. J. W., LEWANDOWSKA N., LIU T., LORIMER D. R., LUO J., LYNCH R. S., MA C.-P., MADISON D. R., MCEWEN A., MCKEE J. W., MCLAUGHLIN M. A., MCMANN N., MEYERS B. W., MEYERS P. M., MINGARELLI C. M. F., MITRIDATE A., NG C., NICE D. J., OCKER S. K., OLUM K. D., PENNUCCI T. T., PERERA B. B. P., PETROV P., POL N. S., RADOVAN H. A., RANSOM S. M., RAY P. S., ROMANO J. D., RUNNOE J. C., SAFFER A., SARDESAI S. C., SCHMIEDEKAMP A., SCHMIEDEKAMP C., SCHMITZ K., SHAPIRO-ALBERT B. J., SIEMENS X., FISCELLA S. V. S., STAIRS I. H., STINEBRING D. R., STOVALL K., SUSOBHANAN A., SWIGGUM J. K., TAYLOR J., TAYLOR S. R., THOMPSON M. S., TURNER J. E., VALLISNERI M., VAN HAASTEREN R., VIGELAND S. J., WAHL H. M., WILSON K. P., WITT C. A., WRIGHT D. and YOUNG O., *ApJ*, **997** (2026) 188.
- [335] AGAZIE G., ANUMARLAPUDI A., ARCHIBALD A. M., ARZOUMANIAN Z., BAIER J. G., BAKER P. T., BÉCSY B., BHOONAH A., BLECHA L., BRAZIER A., BROOK P. R., BURKE-SPOLAOR S., BURNETTE R., CASE R., CASEY-CLYDE J. A., CHARISI M., CHATTERJEE S., COHEN T., CORDES J. M., CORNISH N. J., CRAWFORD F., CROMARTIE T., CROWTER K., DECESAR M. E., DEMOREST P. B., DENG H., DEY L., DOLCH T., FERRARA E. C., FIORE W., FONSECA E., FREEDMAN G. E., GARDINER E. C., GARVER-DANIELS N., GENTILE P. A., GERSBACH K. A., GLASER J., GÓMEZ-CORTES B. D., GOOD D. C., GÜLTEKIN K., HARRIS C. J., HAZBOUN J. S., JENNINGS R. J., JOHNSON A. D., JONES M. L., KAPLAN D. L., KELLEY L. Z., KERR M., KEY J. S., LAAL N., LAM M. T., LAMB W. G., LARSEN B., LAZIO T. J. W., LEWANDOWSKA N., LEYS M., LIU T., LORIMER D. R., LUO J., LYNCH R. S., MA C.-P., MADISON D. R., MATT C., MCEWEN A., MCKEE J. W., MCLAUGHLIN M. A., MCMANN N., MEYERS B. W., MEYERS P. M., MINGARELLI C. M. F., MITRIDATE A., NG C., NICE D. J., OCKER S. K., OLUM K. D., PENNUCCI T. T., PERERA B. B. P., PETROV P., POL N. S., RADOVAN H. A., RANSOM S. M., RAY P. S., ROMANO J. D., RUNNOE J. C., SAFFER A., SARDESAI S. C., SCHMIEDEKAMP

A., SCHMIEDEKAMP C., SCHMITZ K., SHAPIRO-ALBERT B. J., SIEMENS X., SIMON J., SOSA FISCELLA S. V., STAIRS I. H., STINEBRING D. R., STOVALL K., SUSOBHANAN A., SWIGGUM J. K., TAYLOR J., TAYLOR S. R., THOMPSON M. S., TURNER J. E., VALLISNERI M., VAN HAASTEREN R., VIGELAND S. J., WAHL H. M., WANG S., WILSON K. P., WITT C. A., WRIGHT D. and YOUNG O., *arXiv e-prints*, (2026) arXiv:2601.09481.

- [336] AGAZIE G., ANUMARLAPUDI A., ARCHIBALD A. M., ARZOUMANIAN Z., BAIER J. G., BAKER P. T., BÉCSY B., BLECHA L., BRAZIER A., BROOK P. R., BURKE-SPOLAOR S., CASEY-CLYDE J. A., CHARISI M., CHATTERJEE S., COHEN T., CORDES J. M., CORNISH N. J., CRAWFORD F., CROMARTIE H. T., CROWTER K., DECESAR M. E., DEMOREST P. B., DENG H., DEY L., DOLCH T., ESMYOL D., FERRARA E. C., FIORE W., FONSECA E., FREEDMAN G. E., GARDINER E. C., GARVER-DANIELS N., GENTILE P. A., GERSBACH K. A., GLASER J., GOOD D. C., GÜLTEKIN K., HAZBOUN J. S., JENNINGS R. J., JOHNSON A. D., JONES M. L., KAPLAN D. L., KELLEY L. Z., KERR M., KEY J. S., LAAL N., LAM M. T., LAMB W. G., LARSEN B., LAZIO T. J. W., LEWANDOWSKA N., LINO DOS SANTOS R. R., LIU T., LORIMER D. R., LUO J., LYNCH R. S., MA C.-P., MADISON D. R., MCEWEN A., MCKEE J. W., MCLAUGHLIN M. A., MCMANN N., MEYERS B. W., MEYERS P. M., MINGARELLI C. M. F., MITRIDATE A., NG C., NICE D. J., OCKER S. K., OLUM K. D., PENNUCCI T. T., PERERA B. B. P., POL N. S., RADOVAN H. A., RANSOM S. M., RAY P. S., ROMANO J. D., RUNNOE J. C., SAFFER A., SARDESAI S. C., SCHMIEDEKAMP A., SCHMIEDEKAMP C., SCHMITZ K., SCHRÖDER T., SHAPIRO-ALBERT B. J., SIEMENS X., SIMON J., SIWEK M. S., SOSA FISCELLA S. V., STAIRS I. H., STINEBRING D. R., STOVALL K., SUSOBHANAN A., SWIGGUM J. K., TAYLOR S. R., TURNER J. E., UNAL C., VALLISNERI M., VAN HAASTEREN R., VIGELAND S. J., VON ECKARDSTEIN R., WAHL H. M., WITT C. A., WRIGHT D. and YOUNG O., *ApJ*, **978** (2025) L29.

- [337] AGAZIE G., ANUMARLAPUDI A., ARCHIBALD A. M., ARZOUMANIAN Z., BAIER J. G., BAKER P. T., BÉCSY B., BLECHA L., BRAZIER A., BROOK P. R., BURKE-SPOLAOR S., CASEY-CLYDE J. A., CHARISI M., CHATTERJEE S., COHEN T., CORDES J. M., CORNISH N. J., CRAWFORD F., CROMARTIE H. T., CROWTER K., DECESAR M. E., DEMOREST P. B., DENG H., DEY L., DOLCH T., FERRARA E. C., FIORE W., FONSECA E., FREEDMAN G. E., GARDINER E. C., GARVER-DANIELS N., GENTILE P. A., GERSBACH K. A., GLASER J., GOOD D. C., GUERTIN L., GÜLTEKIN K., HAZBOUN J. S., JENNINGS R. J., JOHNSON A. D., JONES M. L., KAISER A. R., KAPLAN D. L., KELLEY L. Z., KERR M., KEY J. S., LAAL N., LAM M. T., LAMB W. G., LARSEN B., LAZIO T. J. W., LEWANDOWSKA N., LIU T., LORIMER D. R., LUO J., LYNCH R. S., MA C.-P., MADISON D. R., MCEWEN A., MCKEE J. W., MCLAUGHLIN M. A., MCMANN N., MEYERS B. W., MEYERS P. M., MIDDLETON H., MINGARELLI C. M. F., MITRIDATE A., MOORE C. J., NG C., NICE D. J., OCKER S. K., OLUM K. D., PENNUCCI T. T., PERERA B. B. P., POL N. S., RADOVAN H. A., RANSOM S. M., RAY P. S., ROMANO J. D., RUNNOE J. C., SAFFER A., SARDESAI S. C., SCHMIEDEKAMP A., SCHMIEDEKAMP C., SCHMITZ K., SHAPIRO-ALBERT B. J., SIEMENS X., SIMON J., SIWEK M. S., SOSA FISCELLA S. V., STAIRS I. H., STINEBRING D. R., STOVALL K., SUSOBHANAN A., SWIGGUM J. K., TAYLOR

- S. R., TURNER J. E., UNAL C., VALLISNERI M., VECCHIO A., VIGELAND S. J., WAHL H. M., WITT C. A., WRIGHT D. and YOUNG O., *ApJ*, **978** (2025) 168.
- [338] SAH M. R. and MUKHERJEE S., *arXiv e-prints*, (2024) arXiv:2407.11669.
- [339] CHEN Y., DANIEL M., D’ORAZIO D. J., FAN X., MITRIDATE A., SAGUNSKI L., XUE X., NANOGRAV COLLABORATION, AGAZIE G., ANUMARLAPUDI A., ARCHIBALD A. M., ARZOUMANIAN Z., BAIER J. G., BAKER P. T., BÉCSY B., BLECHA L., BRAZIER A., BROOK P. R., BURKE-SPOLAOR S., BURNETTE R., CASEY-CLYDE J. A., CHARISI M., CHATTERJEE S., COHEN T., CORDES J. M., CORNISH N. J., CRAWFORD F., CROMARTIE H. T., CROWTER K., DECESAR M. E., DEMOREST P. B., DENG H., DEY L., DOLCH T., FERRARA E. C., FIORE W., FONSECA E., FREEDMAN G. E., GARDINER E. C., GARVER-DANIELS N., GENTILE P. A., GERSBACH K. A., GLASER J., GOOD D. C., GÜLTEKIN K., HAZBOUN J. S., JENNINGS R. J., JOHNSON A. D., JONES M. L., KAPLAN D. L., KELLEY L. Z., KERR M., KEY J. S., LAAL N., LAM M. T., LAMB W. G., LARSEN B., LAZIO T. J. W., LEWANDOWSKA N., LIU T., LORIMER D. R., LUO J., LYNCH R. S., MA C.-P., MADISON D. R., MCEWEN A., MCKEE J. W., MCLAUGHLIN M. A., MCMANN N., MEYERS B. W., MEYERS P. M., MINGARELLI C. M. F., NG C., NICE D. J., OCKER S. K., OLUM K. D., PENNUCCI T. T., PERERA B. B. P., PETROV P., POL N. S., RADOVAN H. A., RANSOM S. M., RAY P. S., ROMANO J. D., RUNNOE J. C., SAFFER A., SARDESAI S. C., SCHMIEDEKAMP A., SCHMIEDEKAMP C., SCHMITZ K., SHAPIRO-ALBERT B. J., SIEMENS X., SIMON J., SIWEK M. S., SOSA FISCELLA S. V., STAIRS I. H., STINEBRING D. R., STOVALL K., SUSOBHANAN A., SWIGGUM J. K., TAYLOR J., TAYLOR S. R., TURNER J. E., ÜNAL C., VALLISNERI M., VAN HAASTEREN R., VIGELAND S. J., WAHL H. M., WITT C. A., WRIGHT D. and YOUNG O., *Nature Astronomy*, (2026) .
- [340] LIN M.-X., LIDZ A. and MA C.-P., *arXiv e-prints*, (2026) arXiv:2602.16808.
- [341] SATO-POLITO G., ZALDARRIAGA M. and QUATAERT E., *Phys. Rev. D*, **110** (2024) 063020.
- [342] AGAZIE G., ANUMARLAPUDI A., ARCHIBALD A. M., ARZOUMANIAN Z., BAIER J. G., BAKER P. T., BÉCSY B., BLECHA L., BRAZIER A., BROOK P. R., BURKE-SPOLAOR S., BURNETTE R., CASEY-CLYDE J. A., CHARISI M., CHATTERJEE S., COHEN T., CORDES J. M., CORNISH N. J., CRAWFORD F., CROMARTIE H. T., CROWTER K., DECESAR M. E., DEMOREST P. B., DENG H., DEY L., DOLCH T., FERRARA E. C., FIORE W., FONSECA E., FREEDMAN G. E., GARDINER E. C., GARVER-DANIELS N., GENTILE P. A., GERSBACH K. A., GLASER J., GOOD D. C., GÜLTEKIN K., HAZBOUN J. S., JENNINGS R. J., JOHNSON A. D., JONES M. L., KAPLAN D. L., KELLEY L. Z., KERR M., KEY J. S., LAAL N., LAM M. T., LAMB W. G., LARSEN B., LAZIO T. J. W., LEWANDOWSKA N., LIU T., LORIMER D. R., LUO J., LYNCH R. S., MA C.-P., MADISON D. R., MCEWEN A., MCKEE J. W., MCLAUGHLIN M. A., MCMANN N., MEYERS B. W., MEYERS P. M., MINGARELLI C. M. F., MITRIDATE A., NATARAJAN P., NG C., NICE D. J., OCKER S. K., OLUM K. D., PENNUCCI T. T., PERERA B. B. P., PETROV P., POL N. S., RADOVAN H. A., RANSOM S. M., RAY P. S., RUNNOE J. C., SAFFER A., SARDESAI S. C., SCHMIEDEKAMP

- A., SCHMIEDEKAMP C., SCHMITZ K., SHAPIRO-ALBERT B. J., SIEMENS X., SIMON J., SIWEK M. S., SOSA FISCELLA S. V., STAIRS I. H., STINEBRING D. R., STOVALL K., SUN J. P., SUSOBHANAN A., SWIGGUM J. K., TAYLOR J., TAYLOR S. R., TURNER J. E., UNAL C., VALLISNERI M., VAN HAASTEREN R., VIGELAND S. J., WAHL H. M., WITT C. A., WRIGHT D. and YOUNG O., *ApJ*, **987** (2025) 5.
- [343] AGAZIE G., ANUMARLAPUDI A., ARCHIBALD A. M., ARZOUMANIAN Z., BAIER J., BAKER P. T., BÉCSY B., BLECHA L., BRAZIER A., BROOK P. R., BURKE-SPOLAOR S., BURNETTE R., CASE R., CASEY-CLYDE J. A., CHARISI M., CHATTERJEE S., COHEN T., CORDES J. M., CORNISH N. J., CRAWFORD F., CROMARTIE H. T., CROWTER K., DECESAR M. E., DEGAN D., DEMOREST P. B., DOLCH T., DRACHLER B., FERRARA E. C., FIORE W., FONSECA E., FREEDMAN G. E., GARVER-DANIELS N., GENTILE P. A., GLASER J., GOOD D. C., GÜLTEKIN K., HAZBOUN J. S., JENNINGS R. J., JOHNSON A. D., JONES M. L., KAISER A. R., KAPLAN D. L., KELLEY L. Z., KERR M., KEY J. S., LAAL N., LAM M. T., LAMB W. G., LAZIO T. J. W., LEWANDOWSKA N., LIU T., LORIMER D. R., LUO J., LYNCH R. S., MA C.-P., MADISON D. R., MCEWEN A., MCKEE J. W., MCLAUGHLIN M. A., MCMANN N., MEYERS B. W., MINGARELLI C. M. F., MITRIDATE A., NATARAJAN P., NG C., NICE D. J., OCKER S. K., OLUM K. D., PENNUCCI T. T., PERERA B. B. P., POL N. S., RADOVAN H. A., RANSOM S. M., RAY P. S., ROMANO J. D., SAFFER A., SARDESAI S. C., SCHMIEDEKAMP A., SCHMIEDEKAMP C., SCHMITZ K., SHAPIRO-ALBERT B. J., SIEMENS X., SIMON J., SIWEK M. S., STAIRS I. H., STINEBRING D. R., STOVALL K., SUN J. P., SUSOBHANAN A., SWIGGUM J. K., TAYLOR J. A., TAYLOR S. R., TURNER J. E., UNAL C., VALLISNERI M., VIGELAND S. J., WAHL H. M., WITT C. A., YOUNG O. and NANOGRAV COLLABORATION, *ApJ*, **964** (2024) L14.
- [344] MCLAUGHLIN M., WALTER F., HALLINAN G. and RAVI V., *DSA-2000 Community Science Document*, <https://www.deepsynoptic.org/commeet> (Mar. 2025).